Application of Ultrasound to the Morphology Control of Crystals and Deposition of Nanoparticles

by

Recep Kaş

A Thesis Submitted to the
Graduate School of Engineering
in Partial Fulfillment of the Requirements for
the Degree of

Master of Science
in
Material Science and Engineering

Koc University

December 2011

Koc University

Graduate School of Sciences and Engineering

This is to certify that I have examined this copy of a master's thesis by

Recep Kaş

and have found that it is complete and satisfactory in all respects,
and that any and all revisions required by the final
examining committee have been made.

Committee Members:

_____

Özgür Birer, Ph. D. (Advisor)

_____

Uğur Ünal, Ph. D.

_____

Oğuzhan Gürlü, Ph. D.

Date: _____

ABSTRACT

In the first part of the present study, the effect of reaction conditions to the crystal morphology of the Brochantite ($Cu_4(OH)_6SO_4$) crystal is investigated. Different morphologies ranging from flowers, to bricks, belts and needles are obtained in different temperatures and pHs under ultrasonic field. Sodium peroxydisulfate ($Na_2S_2O_8$) is used both as sulfate (SO_4^{2-}) and hydroxyl anion (OH^-) source by ultrasonic and thermal decomposition. Different characterization techniques are used to find the reaction pathway and propose possible crystal growth mechanisms. The morphologies of the products are found to be determined by the relative formation rates of the sulfate and hydroxide anions.

In the second part of this study, silica and organically modified silica particles are deposited onto titanium under ultrasonic field. The significance of the solvent to the deposition process is demonstrated. Acetone is found to be the best solvent to obtain a fully coated surface and to deposit larger particles. The effect of the ultrasonic field to the deposition process is shown by changing the thickness of the coating with different amplitudes of the ultrasonic waves. Time dependent study of the deposition process is done to predict the structure of the produced films. The films are found to be composed of layers of silica particles with different particle sizes. Organosilanes are used to decrease the aggregation of silica particles and modify of the surface properties of the coatings. The corrosion tests of the coated samples revealed that coated samples show better corrosion resistance compared to bare titanium.

ÖZET

Sunulan çalışmaların ilk kısmında reaksiyon şartlarının brokantit'in ($Cu_4(OH)_6SO_4$) kristal morfolojisine etkisi incelenmiştir. Ultrason dalgaları altında değişik sıcaklık ve pH değerlerinde reaksiyon yapılarak çiçek, dikdörtgen tuğla, kuşak ve iğne şekillerinde değişik kristal morfolojileri elde edilmiştir. Sodyum persülfat ($Na_2S_2O_8$) hem hidroksil (OH^-) hem de sülfat (SO_4^{2-}) anyonlarını radikal reaksiyonları aracılığıyla üretmek için kullanılmıştır. Farklı morfolojilerin oluşumunu ve reaksiyon ve kristal büyüme mekanizmalarını anlamak amacıyla değişik karakterizasyon teknikleri kullanılmıştır. Bütün bu bilgilerin ışığında farklı morfolojilerin oluşumunu hidroksil ve sülfat anyonlarının oluşma hızlarına bağlı oldukları belirlenmiştir.

Araştırmanın ikinci kısmında ise, titanyum yüzeyi yüksek güçte ultrason dalgalarını kullanarak silika ve organik katkılı silika parçacıkları ile kaplanmıştır. Kullanılan çözücünün kaplama yapısına ve kalınlığına önemli etkide bulunduğu gösterilmiştir. Ortak çözücü olarak aseton kullanıldığında titanyum yüzeyinin hiçbir kısmı açıkta kalmayacak şekilde değişik parçacık boyutlarıyla kaplanmalar yapılabilmektedir. Kaplamanın kalınlığı ultrason enerjisine bağlı olarak değiştirilerek, ultrason enerjisinin kaplamadaki rolü vurgulanmıştır. Kaplama özellikleri zamana bağlı olarak çalışılarak kalın kaplamaların iç katmanlarındaki yapı gösterilmiştir. Kaplanan silika parçacıklarının boyutu sisteme çok az miktarda organosilan ekleyerek arttırılabilmektedir. Elektrokimyasal çalışmalar, kaplamaların korozyona karşı kaplanmamış titanyumdan daha iyi özellikler gösterdiğini ispatlamıştır.

ACKNOWLEDGEMENT

I am deeply grateful to my supervisor Asst. Prof. Dr. Özgür Birer for his support and guidance during my studies and accepting me as a member to his group. His encouragement and motivation always stimulated my excitement. I would like to thank Asst. Prof. Dr. Uğur Ünal, whom we share our lab, for being such a polite person when we need assistance. He is one of the few people who we do not hesitate to ask for help. I really appreciate Assoc. Prof. Dr. Oğuzhan Gürlü from İstanbul Technical University for being in my thesis committee.

I would like give a special thank to Dr. Annamaria Miko for her valuable hints and motivation during at all stage of my research. With her kind and helpful approach to students, she is already among the favorites of the students. I would like to thank my lab mate Cansu Yıldırım for her friendship and help during the experimental part. Also I would like than my lab mates Fatma Sinem Ertaş and Çağnur Celaloğlu who joined to our lab this semester. I would like to thank Ahmet Alptekin Topçu, Hüseyin Enis Karahan and Caner Nazlı, who have unique personalities, for their fruitful discussions which provided me a different perspective and helped me to solve technical problems. I would like to thank advanced ceramics research laboratory group members Ceren Yılmaz, Refik Ergün, Eylül Sarac, whom we share our wet lab, for their kindly approaches to the problems. I would like to thank Ali Baş, Muharrem Güler (The glass master) for their friendship during the lunches and coffee breaks. I would like to thank Bekir Yenilmez (Bekirpedia) and Erhan Aysan for being my home mates and sharing these two enjoyable years with me. I would like to thank Enes Kılıç, whom I spend my free time, for his everlasting fellowship. I would like to thank Selçuk Acar, Pınar Tatar,

Ali Bateni, and all the people whom I could not mention one by one. Also, we thank Koç University Surface Science and Technology Center (KUYTAM) for the use of the XPS and electron microscope. The second part of this study was supported by the Scientific and Technological Research Council of Turkey (TÜBİTAK, Project No. 109T893) and we would like to express our gratitude to the Council for its financial support.

Finally I would like thank to my parents, brothers and sister for their endless support and encouragement. Last but not least I would like to give my special thanks to Assoc. Prof. Dr. Funda Yağcı Acar who has contribution in every footstep of my career.

TABLE OF CONTENTS

LIST OF TABLES

CHAPTER 1

CHAPTER 2

LIST OF FIGURES

CHAPTER 1

CHAPTER 2

NOMENCLATURE

UV	Ultra Violet
SEM	Scanning Electron Microscope
XRD	X-ray Diffraction
TGA	Thermogravimetric Analysis
ICP-OES	Inductively Coupled Plasma Optical Emission Spectroscopy
CuO	Copper Oxide
SO_4^{2-}	Sulfate Anion
OH^-	Hydroxide Anion
TiO_2	Titania (Titanium dioxide)
SiO_2	Silica (Silicon dioxide)
TEOS	Tetraethyl Orthosilicate
-OR	Alkoxide
ROH	Alcohol
NiTi	Alloy of Nickel and Titanium
SiOH	Silanol
SiC	Silicon Carbide
ES	Experimental Spectrum
SS	Simulated Spectrum
FE-SEM	Field Emission Scanning Electron Microscope
OCP	Open Circuit Potential
CV	Cyclic Voltammetry

GENERAL INTRODUCTION

Sound is transmitted by longitudinal waves in any elastic substance via series of compression and expansion cycles. During the compression and expansion cycles, distance between the molecules will change. When the liquids are irradiated with ultrasonic waves, at some point the negative pressure applied during the expansion cycle becomes large enough to break the bonds that hold the liquid molecules together. A small bubble called cavitation is formed in the solution. Once the bubble is formed it oscillates with the oscillating ultrasonic field. During the oscillation the bubble grows by taking energy from the environment. After a certain point, the bubble can not take sufficient energy from the environment and it wildly collapses. During the collapse the gas inside bubble is compressed, therefore locally very high temperatures and pressures are formed. Cavitation phenomena is firstly introduced in 1895 by John Thornycroft and Sidney Barnaby [1]. They investigated the reason of the damage which occurred quite earlier than expected in the propellers of the ships. The mechanical motion of the propeller separates the water molecules from each other and creates appropriate conditions for the cavitation nucleation. The collapse of the cavitation near the propeller surface is found to be the reason of the earlier damage of the propellers. The studies on the cavitation phenomena is started to be understood after the significant developments in the electric circuitry and transducers in 1940s. These developments lead to applications of ultrasound to materials chemistry and a new area that is called "Sonochemistry" was born. With the development of cheap and commercial devices, the number of the papers published in sonochemical processes increased dramatically in the last 30 years.

The first part of research summarized in this M.Sc. thesis is focused on the synthesis of new nanostructures in a unique reaction environment under ultrasonic field. The second part of the thesis consists of deposition of particles onto a hard substrate by using the power of ultrasound. Introduction sections will introduce the major concepts of sonochemistry, sol-gel chemistry and corrosion science in addition to review of the related literature.

Chapter 1

Sonochemical Shape Control of Copper Hydroxysulfates

INTRODUCTION

1.1 General Aspects of Sonochemistry

Sonochemistry is a research area that utilizes the ultrasonic waves (20 kHz-1 MHz) to create a unique environment for the chemical reactions. The wavelength of the ultrasonic waves used in sonochemistry is far from the molecular dimensions (10 cm-0.1 cm). Therefore, the chemical activity of the ultrasound does not originate from the interaction between the sound waves and molecules as in the case of photochemistry. Instead, the chemical activity is mostly based on the collapse of the cavitation. Suslick et al.[2] performed series of ligand exchange reactions on different metal carbonyls in order to estimate the temperatures inside the cavitation during the collapse. By using the reaction rates and the Arrhenius equation, the temperatures inside and on the surface of the cavitation are found to be 5200±650 K and ~1900 K respectively. These temperatures are also verified with complementary techniques [3]. The temperature increase is local and the surrounding liquid cools down the hot spot with a very high cooling rate at the order of 10^{10} °C/s. Therefore, the ultrasonic activity in liquid solutions produces a unique environment for the chemical reactions [4].

One of the most important features of the sonochemistry is the formation of the radicals during the collapse of the cavitation. Makino et al. [5] is the first reporter of a

direct proof for the formation of OH· and H· radicals by the splitting of water under ultrasonic field. They used spin trapping and electron spin resonance (ESR) to prove their findings.

In order to form cavitation in the solution, a critical intensity of ultrasound is required. The intensity of the ultrasound is proportional to the square amplitude of the ultrasonic wave. The increase of the amplitude increases the cavitation formation. However, extreme intensities may deteriorate the ultrasonic transducer very quickly. Therefore, higher amplitudes should be applied only to solvents with high viscosities. The viscosity increase in the solution increases the threshold intensity for cavitation formation. This is due to the requirement of higher negative pressure to break apart the solvent molecules during the expansion cycle. Also, the temperature of the reaction must be carefully chosen depending on the solvent. The effect of the temperature is a bit abrupt. The cavitation nucleation, growth and collapse rate increases with the increasing temperature since the solvent interactions are weakened. However, the collapse of the cavitation is reported to be less violent because more vapor is filled inside the bubble [6]. The dissolved gases in the system also facilitate the formation of the cavitation. They act as nucleation site for the cavitation nucleation. Dissolved gases are removed from the reaction mixture in time, therefore bubbling gas through the reaction solution increase the cavitation formation [7].

1.2 Ultrasonic system types

Ultrasonic baths and horns are used to irradiate the liquid solutions with ultrasound. Ultrasound waves are produced by applying high AC voltage to a piezoelectric material. The intensities of the ultrasonic baths used in many laboratories

are quite low. Therefore, the ultrasonic horns are used as reliable and intense sources of ultrasound in most of the sonochemical reactions. A typical setup for the horn system is given in Figure 1.1 [8].

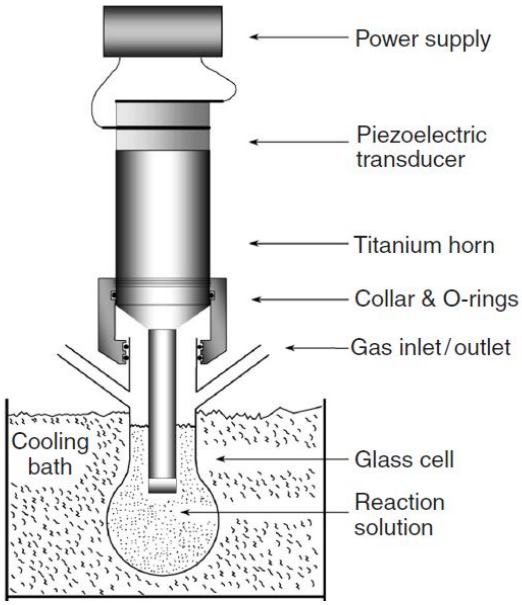

Figure 1. 1 Experimental setup for sonochemical reactions

The ultrasonic horns are mostly made from titanium and its alloys. A cooling bath is needed to control the temperature of the reaction since the gradual formation of cavitations increases the temperature of the solution.

1.3 Applications to Materials Chemistry

Inorganic nanomaterials with desired sizes and morphologies have attracted both technological and fundamental interest for morphology dependent properties and possible wide range applications [9-11]. Wet chemistry is one of the promising methods for the synthesis of nanoparticles with different shapes. This approach employs hard or soft templates or utilizes the anisotropic crystal structure of solid materials without using templates [12-14]. However, these reactions can be typically slow and may even

require a couple of days or a couple of weeks before the product is obtained. Sonochemical method, on the other hand, is a quick alternative which has been utilized for the synthesis of nanoparticles of metal oxides [15, 16], chalcogenides [17, 18] and noble metals [19]. Recently, shape control of nanomaterials produced under ultrasonic field has been demonstrated with ZnO [20, 21] and gold nanoparticles.

Copper hydroxysulfates are corrosion products of copper surfaces exposed to natural conditions [22]. Synthetic crystals, namely Antlerite $Cu_3(OH)_4SO_4$ and Brochantite $Cu_4(OH)_6SO_4$ are typically synthesized by the stoichiometric mixtures of sulfates and hydroxides [23, 24] at moderate temperatures. Hydrothermal conditions (120–200 °C) have also been utilized for these stoichiometric mixtures from several days to several weeks for growing large crystals [25-27]. Alternative routes such as homogenous precipitation from solution by urea hydrolysis [28] and precipitation from a mixture of sulfate and carbonate solutions [29] as well as the traditional methods typically yield only the needle-shaped morphology.

Copper ions and complexes have been used for centuries as antibacterial and antifungal agents in different applications such as medicine, agriculture, water treatment, etc [30-32]. Bordeaux mixture (mixture of copper sulfate, lime and water) has been used as fungicide over the world in agriculture since 1880s [32]. Standard Bordeaux mixture contains brochantite, antlerite, posnjakite [33] and lately brochantite itself was proposed as fungicide [34]. Recent studies show that the antibacterial activities depend on the size as well as the shape of the particles in cuprous oxide and silver [35-37].

Terephthalic acid has been used in photochemistry and ultrasound dosimetric experiments as OH· radical trap [38-40]. Terephthalic acid itself is non-fluorescent. The

OH· radical reacts with the terephthalic acid to form 2-hydroxyterephthalate which fluoresces in visible region. Although, there are several possible OH· radical addition products, the only fluorescent species is the major stable product which is 2-hydroxyterephthalate (Figure 1.2) [39, 41].

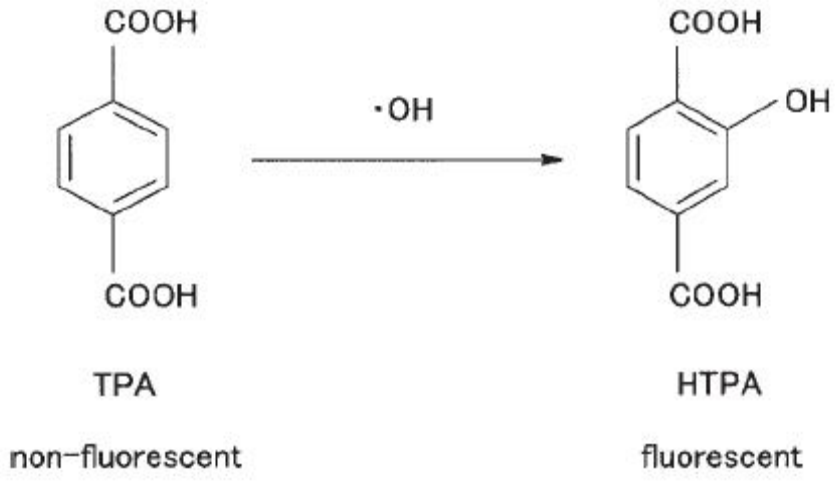

Figure 1. 2 Formation of fluorescent 2-hydroxyterephthalate from terephthalic acid

In this study, synthesis of micron size Brochantite crystals in different morphologies is synthesized by using an ultrasound assisted facile method. Ultrasonic field is used to decompose peroxydisulfate anion in the presence of copper acetate in various pH and temperatures. With this technique and precursors, Brochantite crystals can be obtained even at acidic pH compared to the methods used in the literature which start with stoichiometric amounts of copper sulfate and hydroxide anions and yield only a single crystal morphology. Terephthalic acid is used as fluorescence probe to the compare relative OH· yields qualitatively. The yields are used to propose possible reaction pathway and crystal growth mechanism.

EXPERIMENTAL METHOD

The reactions took place in a custom glass sonication cell fitted with a water jacket for temperature control. In a typical run, 0.749 g (3.752 mmol) copper salt and 0.446 g (1.874 mmol) sodium peroxydisulfate were dissolved in 50 mL deionized water (18.2 MΩ cm^{-1}). The solution was placed in the sonication vessel and purged for 30 min with nitrogen gas to remove dissolved oxygen. The solution is purged also during the sonication. The natural pH of this solution was around 5.5. Ammonia was used to adjust the initial pH of solutions to 6.5, 7.5 and 8.5. The temperature of the solution was adjusted to 5, 25, 60 and 80 °C with a circulating chiller. The solution was sonicated for 60 min. Then, the products from the reaction were separated by centrifuging, and washed several times with deionized water and dried in oven at 80 °C. In separate set of experiments, time evolution of products was observed by running the reactions for shorter and longer periods. The thermally activated control reactions were carried out at 80 °C in temperature-controlled vessels.

The OH· radical yields were compared by the fluorescence spectroscopy using terephthalic acid as the marker. In a typical procedure, aqueous solution containing 2 mM terephthalic acid (Alfa Aesar, 98%+), 1 mM sodium peroxydisulfate and 4 mM sodium acetate (Merck, 99% anhydrous) was prepared. The pH of the solution was adjusted with ammonia and/or acetic acid. The experimental procedure was the same as above except copper ions were not present in solution. Reaction times were limited to 30 min. The reactions were run at pH 5.5, 6.5 and 7.5 at 25 °C, and at pH 7.5 at 80 °C under ultrasound irradiation. For comparison, thermal decomposition of peroxydisulfate

was tested at pH 5.5 and at 80 °C. Cavitation induced OH· radical production in pH 5.5 water was also tested at 25 and 80 °C.

Instrumentation

An ultrasonic probe (Bandelin HD 3200 model , 20 kHz, 200 W at 30% efficiency) with 13 mm $TiAl_6V_4$ alloy tip was used. The average intensity was on the order of 50 W/cm^2. Copper acetate monohydrate and sodium peroxydisulfate were from Merck and were used as received (>99%). The scanning electron microscopy (SEM) studies were carried out in a Zeiss Evo 40 SEM furnished with a LaB_6 electron source. The crystals were cast on aluminum stubs from alcohol suspensions and were not coated for analysis. The powder X-ray diffraction (XRD) measurements were performed using a HUBER-G670 diffractometer utilizing a Germanium monochromator and Cu Kα radiation (λ = 1.5406 Å). The thermo gravimetric analyses (TGA) were performed using a SII Seiko SSC/5200 thermal analysis instrument with TG/DTA 220 module under argon flow. The samples were heated up to 1050 °C at a rate of 5 °C/min in Al_2O_3 holders. The optical emission measurements for concentration determination were carried out with a Spectro Genesis inductively coupled plasma optical emission (ICP-OES) spectrometer using solutions of products dissolved in hot nitric acid. Standard stock solution of Cu^{2+} was prepared by dissolving the appropriate amount of $Cu(NO_3)_2{\cdot}3H_2O$ in 3% nitric acid solution. Standard solution of sulfur was prepared from sulfuric acid solution. In each case, a 5-point calibration curve was used to cover the concentration range of interest. A Horiba Fluoromax-3 spectrometer was used for fluorescence experiments. 2-Hydroxyterephthalic acid was excited at 315 nm and the emission between 350 and 550 nm were collected. The reported spectra are corrected for the excitation intensity and dilution factors.

RESULTS and DISCUSSION

In Table 1.1 ultrasonic reactions performed in different conditions are given. The reactions below pH 5.5 do not yield any product since the hydroxyl ion (OH^-) reacts with a proton instead of a copper ion. The reactions above pH 7.5 yield mixed crystals of brochantite and copper oxide (CuO) which is proved by XRD (not shown in here). At high concentration of OH^- and low concentration of sulfate ion (SO_4^{2-}) copper hydroxide ($Cu(OH)_2$) forms and turns in to CuO with the chemical dehydration reaction. This conversion is reported in the literature and it is used to produce CuO from $Cu(OH)_2$ in very low temperatures[10, 13].

Table 1. 1 Summary of the reaction conditions and morphologies for sonochemically synthesized Brochantite

Sample #	Initial pH	Reaction Temperature (^{o}C)	Final pH	% Yield	Crystal Morphology
US1	5.59	5	4.56	3.5	Brick
US2	5.55	25	4.98	8.2	Brick
US3	5.55	60	4.09	16.5	Flower
US4	5.54	80	3.91	11.8	Lumps
US5	6.51	5	6.23	59.0	Lumps
US6	6.50	25	5.59	66.0	Lumps
US7	6.50	60	5.11	68.4	Needle
US8	6.50	80	4.99	77.8	Needle
US9	7.50	5	7.25	87.3	Belt-Needle
US10	7.52	25	6.45	82.5	Belt
US11	7.50	60	5.19	73.1	Needle
US12	7.51	80	4.96	51.9	Needle
US13	8.50	5	6.67	68.8	Lumps
US14	8.51	25	6.03	55.3	Lumps
US15	8.50	60	5.54	46.9	Lumps
US16	8.50	80	5.21	60.3	Lumps

The yield calculation is based on the initial copper amount and stoichiometric composition of brochantite by assuming it is the only solid product, except the reactions at pH 8.5. The yields of the reactions at pH 8.5 are calculated from CuO. The pH of the solutions at the end of the reaction is always lower than the initial pH. Increasing

temperature increases the difference between the initial and final pH. Different crystal morphologies from irregular lumps to flowers, brick, belt and needle forms are observed.

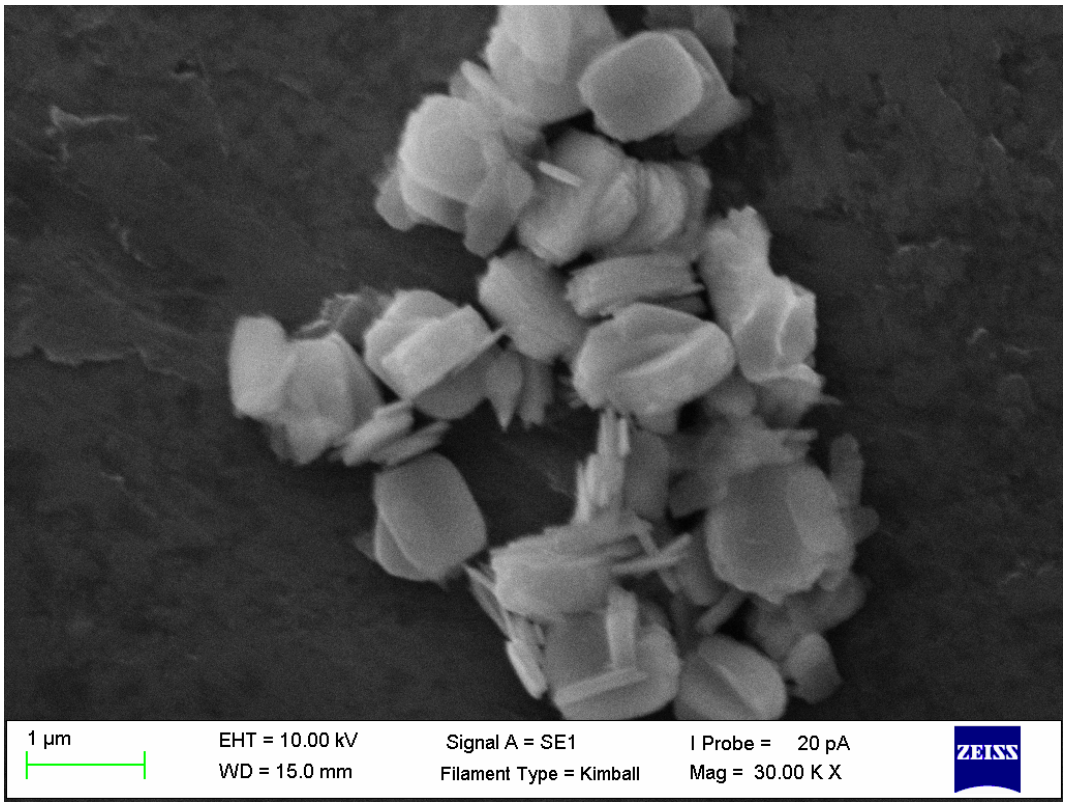

Figure 1. 3 SEM image of Brochantite crystals synthesized at pH 5.5 and 25 °C for 1 hour (Sample US2)

Low temperatures and low pH yield rectangular shape bricks (samples US1,US2). SEM image of the US2 is given in Figure 1.3. The bricks with dimensions of 1.0 x 0.7 µm are oval at the corners. Also small platelets with smaller dimensions can be seen. The pH of the reaction decreases below pH 5 after 1 hour. Therefore, increasing the reaction time leads to dissolution of the crystal rather than growth of the crystal. However, with the dissolution of the crystal, the corners of the bricks sharpened and monodisperse perfect crystals are obtained (Figure 1.4). Thermal reaction at low temperatures can not be performed since persulfate can not be activated. Thermal

reaction at 80°C and pH 5.5 does not yield any defined morphology. Therefore, rectangular shapes of brochantite crystals can be obtained only by sonochemical methods. The unique environment of the ultrasonic field and the formation of the cavitation is the key factor to obtain these nanostructures.

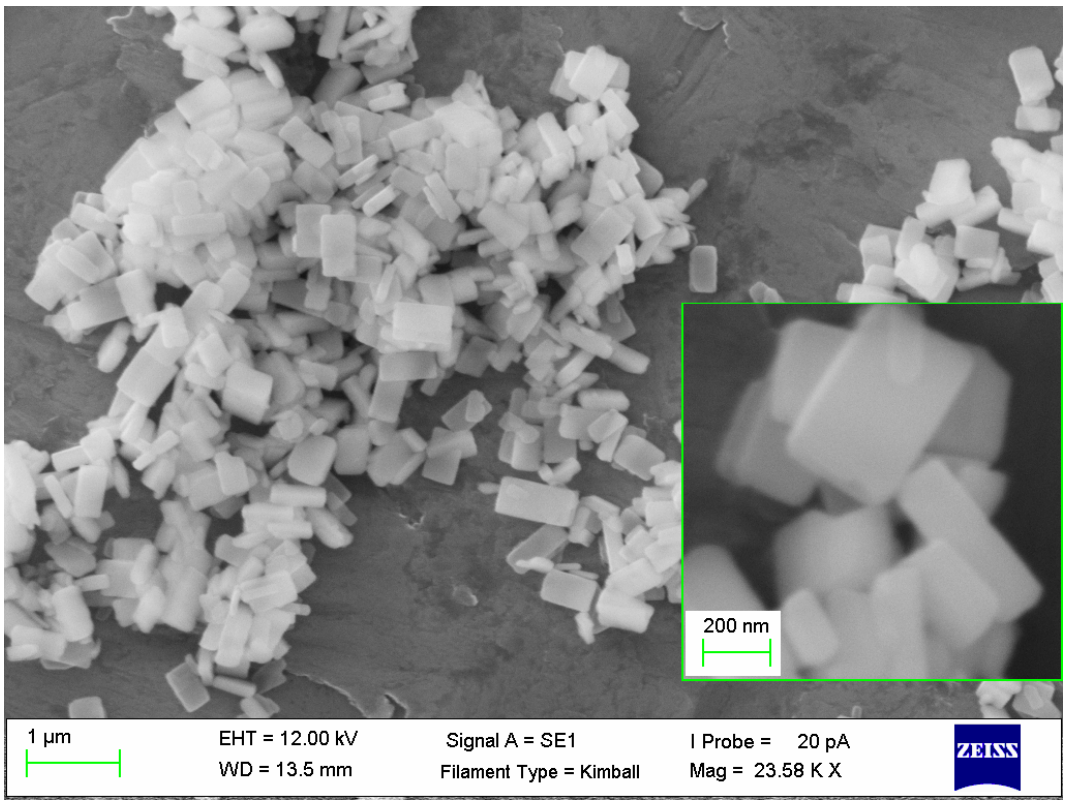

Figure 1. 4 SEM image of Brochantite crystals synthesized at pH 5.5 and 25 °C for 2 hours

When temperature is increased to 60 °C at pH 5.5 the formation of flower shaped structures are observed which are composed of two dimensional subunits. SEM images of the early reaction products are given in Figure 1.5A and 1.5B in addition to the SEM image of the sample. At the early stage of the reaction, 2-D structures with sub-micron dimensionalities are formed in the reaction solution. Due to interactions between these structures, they assemble in a flower shaped manner to form imperfect

crystals. The dimensions and the shape of the subunits are quite similar to building blocks of the flower shaped structure. Therefore, it is concluded that these new structures are formed by those subunits observed at the early stage of the reaction. The organization of the nanomaterials into larger structures is known in the literature as "oriented attachment"[42]. The primary nanostructures can join together to form new ones if the crystallographic requirements are provided. The organization of the subunits is accomplished by the desorption of the solvent and reactant molecules and the formation of the chemical bonds between these subunits. The most common reason for this is the surface energy. The elimination of the interface between the solvent molecules and the subunits decreases the total surface energy. Oriented attachment is a recently introduced phenomena and different structures such as nanosheets, nanoellipsoids , nanoribbons are already reported in the literature [10, 43].

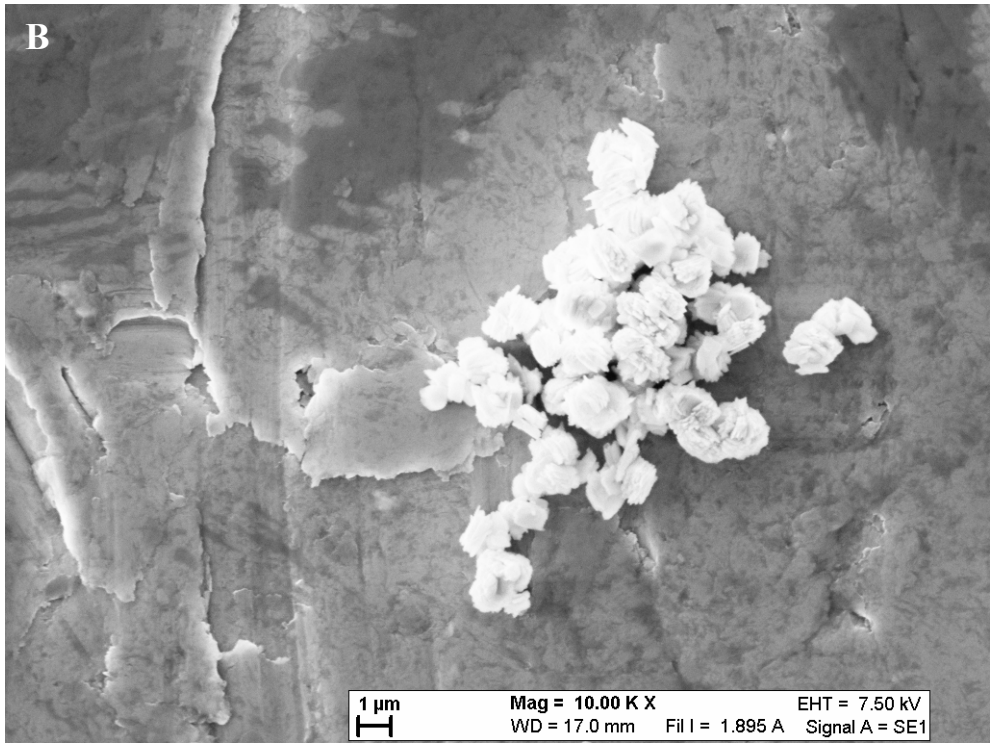
B
1 µm
Mag = 10.00 K X
WD = 17.0 mm
Fil I = 1.895 A
EHT = 7.50 kV
Signal A = SE1

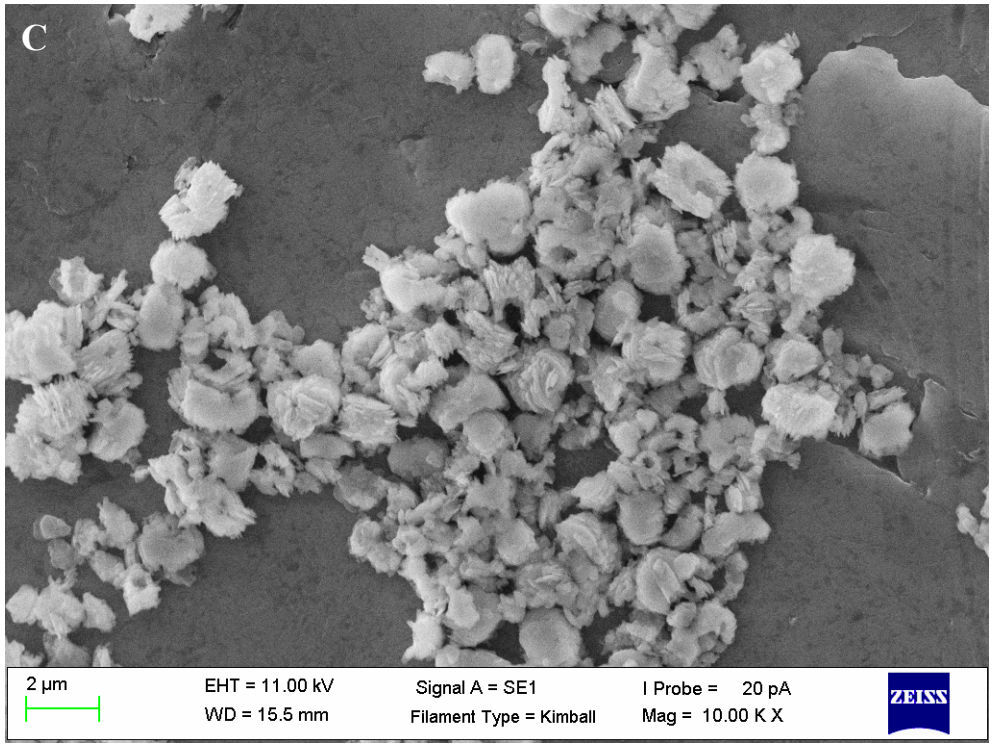
C
2 µm
EHT = 11.00 kV
WD = 15.5 mm
Signal A = SE1
Filament Type = Kimball
I Probe = 20 pA
Mag = 10.00 K X
ZEISS

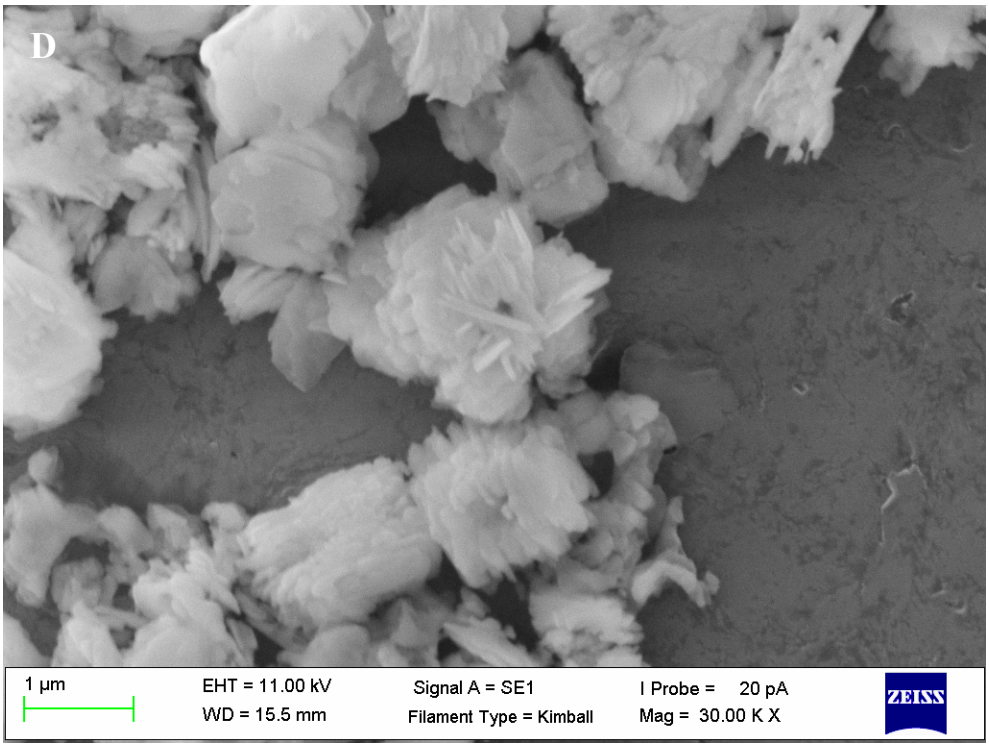

Figure 1. 5 Evolution of flower shaped Brochantite crystals at pH 5.5and 60 °C A) 20 min B) 40 min C) 1 hour D) high magnification image of flower shaped crystals

Increasing the pH and the temperature reveals new structures. After the pH is raised to 6.5, the products at 5 and 25 °C are still irregular lumps of nanoparticles. However, at 60 °C, we begin to observe micrometer sized needle-like structures (not shown in here). The particles dimensions are around 1.6 x 0.3 µm. These particles are intermediates between the belt and needle shapes discussed below. As the temperature increases, the crystals get longer and narrower, and uniformity in size and aspect ratio increases. At 80 °C the crystal size changes to about 2.1 x 0.2 µm. At this pH, the yields are over 50% with the tendency to increase with increasing temperature up to 75%.

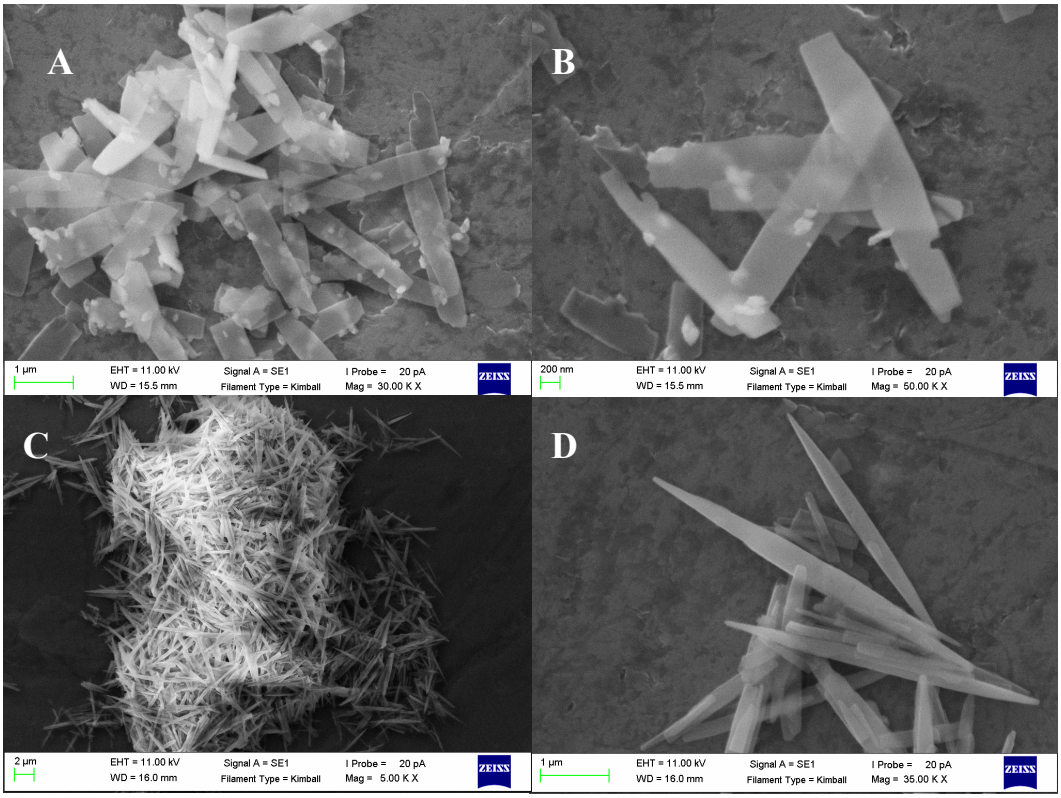

Figure 1. 6 SEM image of the belt and needle shaped crystals A) Low B) High magnification images of the belt morphology C) Low D) high magnification images of the needle crystals

At pH 7.5, low temperatures favor the formation of individual belt like structures whereas formation of needle shaped nanostructures are observed at higher temperatures (Figure1.6A and 1.6B). At 5 °C, 4.6 x 0.6 µm belt like structures are observed. As the temperature increases to 25 °C, the belt sizes get smaller with dimensions 2.6 x 0.5 µm. Further increase in the temperature increases the size and changes the shape from belt to needle (Figure1.6C and 1.6D).The tapered ends measure as small as 100 nm across, while the thickest part is about 400 nm wide. In the SEM image of the early reaction stages of reaction US10 and US12 (not shown in here) shapeless small particles are observed. This shows that the synthesis of these monodisperse polycrystalline materials involves the nucleation of primary particles followed by the aggregation. Once the particles nucleate and reach to critical size, the growth proceeds with the dissolution and

addition of these small particles to larger particles. The polycrystalline nanostructures are composed of randomly oriented primary particles. Thermal activation leads to formation of needle type crystals at higher pH values as in the case of the studies reported in the literature [28, 29]. It must be noted that the thermal activation of peroxydisulfate below 50 °C is considerably slow [44, 45]. Therefore, some of the crystal morphologies reported in this work can only be obtained with the assistance of the ultrasound irradiation.

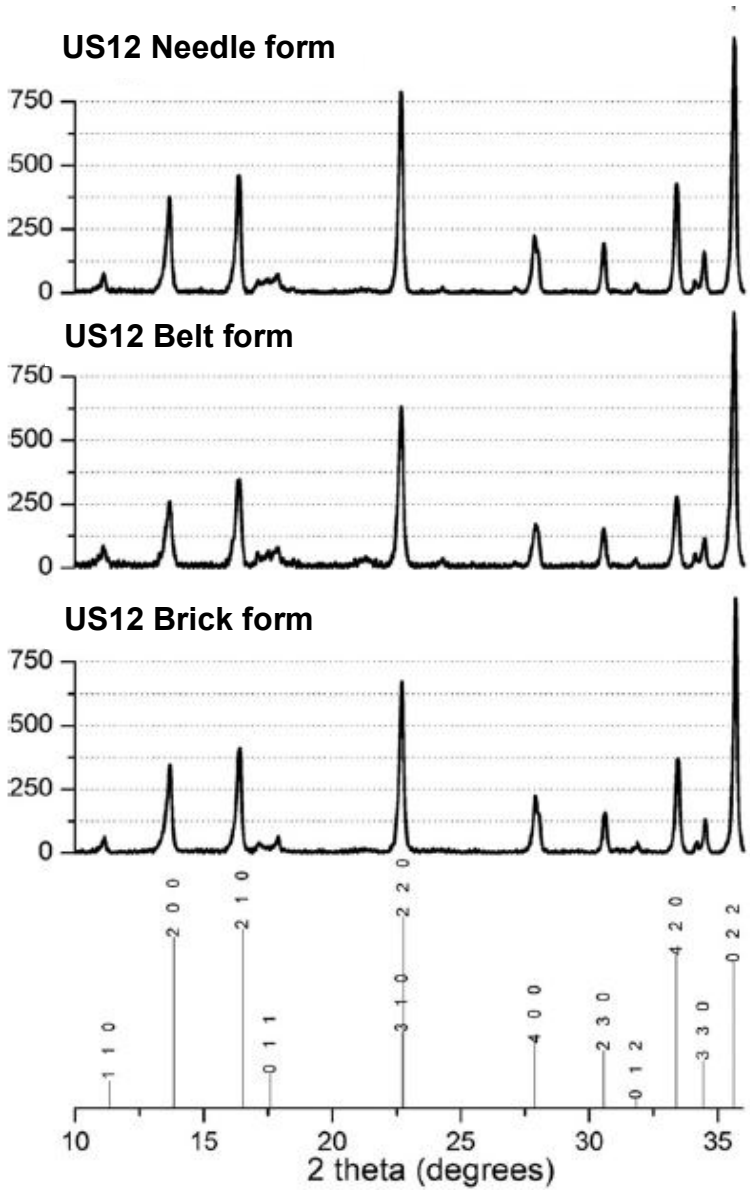

Figure 1. 7 XRD patterns of the products with brick, belt and needle forms in the same scale.

In Figure 1.7, XRD patterns of the selected samples with different morphologies (US2, US10 and US12) are given in addition to theoretical peaks. In XRD diagrams of the samples, there are small differences between the peak positions and intensities. When the peaks are normalized with respect to most intense peak at 35.63° the needle form has higher peak intensities at 13.69° [200], 16.39° [210], 22.70° [220] and 33.43° [420].

The intensity difference is a result of the excessive growth in certain crystallographic directions. This shows that subunits that form the polycrystalline structure are quite different from each other. In addition to the structural differences between subunits, with the effect of the reaction environment, these subunits aggregate to form different morphologies.

The crystal structure of brochantite is reported in the literature [25, 26]. The crystal structure with the orientation of crystallographic planes is given in Figure 1.8. Double chains of copper octahedrons are connected to each other via corner sharing in b direction whereas they are connected to each other via edge sharing in c direction. These connected octahedrons form corrugated planes roughly parallel to bc plane. Copper ions are at the center of the octahedrons and surrounded by the oxygen atoms at the corners. The black spheres stand for sulfur atoms and the corrugated planes are connected to each other with sulfate groups.

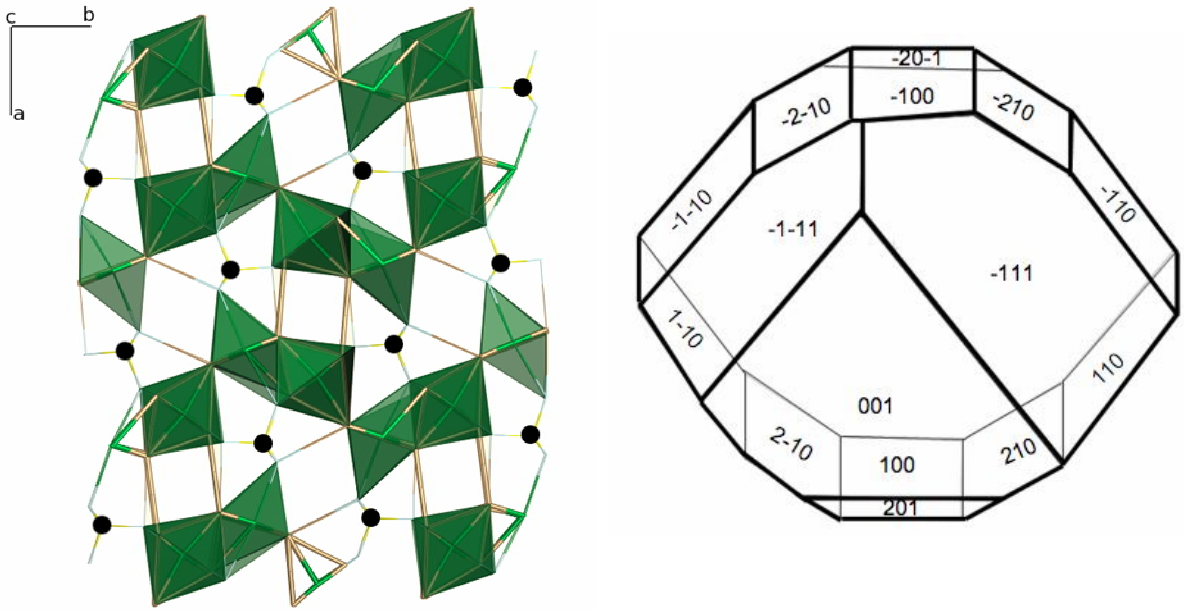

Figure 1. 8 The crystal structure and facets with Miller indices for Brochantite crystal. Oxygen atoms are at the corners of the polyhedra, sulfur atoms are shown as black spheres. Copper ions are located in the centers of each polyhedra.

Growth of the corner shared double octahedrons in b direction needs OH^- anions, whereas both SO_4^{2-} and OH^- anions are needed to connect the corrugated planes. When we compare the XRD diagrams, needle form has higher peak intensities at [200] and [210] peaks. By looking at the crystallographic orientation and the crystal structure in figure 1.8, one can see that these planes corresponds to [100] and [210] planes. Therefore, differences in these intensities originate from differences in growth rates in these directions. We can speculate here that the needle form has the highest sulfate amount per mole of copper among these morphologies.

$$Cu_4(OH)_6SO_4 \longrightarrow 3CuO+CuSO_4+3H_2O \qquad \text{Reaction 1.1}$$

$$3CuO+CuSO_4 \longrightarrow 4CuO+SO_3 \qquad \text{Reaction 1.2}$$

TG and ICP-OES analyses are used to determine the relative amounts of sulfate and hydroxide in these structures. In figure 1.9 TG curves of the brick, belt and needle (US2, US10 and US12) forms are given. The first mass loss in the TG curve corresponds to physically bounded water. The second step which starts around 280 °C stands for the chemical dehydration process (Reaction 1.1). In this step belt and brick forms loses 2.5 mol of water whereas the needle form loses 3.1 mol of water. This step ends up around 450 °C and further increase of the temperature results in the decomposition of the sulfate groups as it is shown in Reaction 1.2. The decomposition of the sulfate group finishes around 730 °C and the needle form loses the highest amount of sulfate group. The O/S ratio based on these results are given in table 1.2 with the Cu/S ratio calculated by ICP-OES.

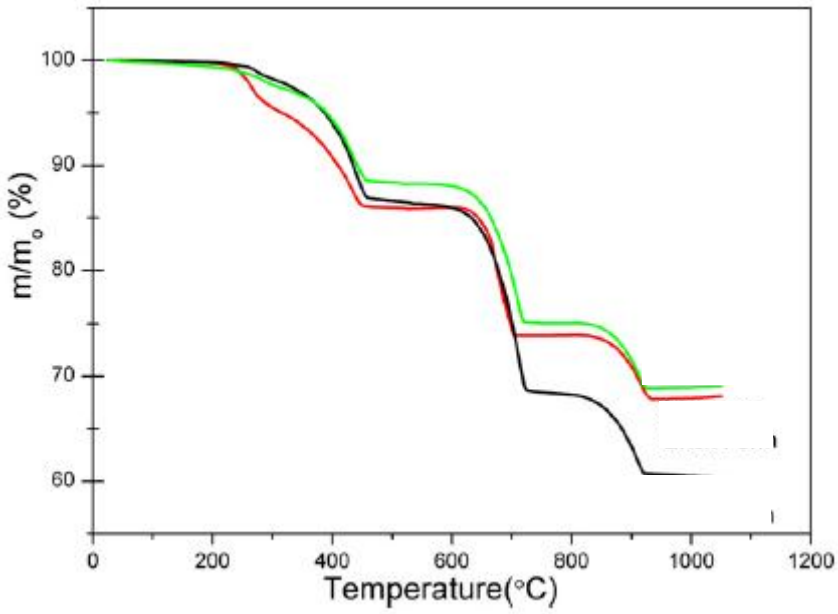

Figure 1. 9 Thermogravimetric analysis of brick (red), belt (green) and needle (black) forms of Brochantite

By looking at the Table 1.2 the effects of pH and temperature to the compositions of the crystals can be argued. Needle and belt forms are produced at the same pH but different temperatures. Needle form has smaller OH/Cu ratio than belt form. Low temperatures favor relatively higher hydroxyl content in the final product. On the other hand, Brick and belt forms are synthesized at same temperatures but at different pH. The OH/Cu ratio of the brick form is the highest among the three morphologies. These findings can be summarized as follows; the crystals grown at the high pH and high temperature conditions have the smallest relative amount of hydroxides, and conversely have the highest relative amount of sulfates compared to the crystals grown under different conditions. The XRD results also show that the needle form has highest peak intensity at peak [220]. Therefore, the needle form is mostly composed of chains of copper octahedrons connected via sulfate group. In the belt and brick forms the connection of these chains by edge sharing is favored to form a plane.

Table 1. 2 Compositions of the brick, belt and needle forms of Brochantite determined by TGA and ICP-OES analyses

Sample Morphology (Number,$pH_{initial}$, temperature in ^{o}C)	O/S molar ratio from TG Analysis	Cu/S molar ratio from ICP-OES Analysis	Estimated OH/Cu molar ratio $\left(\frac{O}{S}\right)\left(\frac{S}{Cu}\right)-4\left(\frac{S}{Cu}\right)$
Brochantite $Cu_4(OH)_6SO_4$	10.0	4.0	1.5
Brick (US2; 5.5 ; 25)	10.51± 0.03	5.19 ± 0.02	1.25 ± 0.01
Belt (US10; 7.5 ; 25)	9.33 ± 0.03	5.80 ± 0.02	0.92 ± 0.01
Needle (US12; 7.5 ; 80)	8.38 ± 0.03	5.04 ± 0.02	0.87 ± 0.01

The emission spectra of 2-hydroxyterephthalate is presented in Figure 1.9 as a semi-quantitative measure of the OH· radical where it yields under the same pH and temperature conditions discussed above. It should be noted, however, in order to avoid undesired reactions, the peroxydisulfate and consequently the terephthalic acid concentrations were kept much smaller compared to the actual runs.

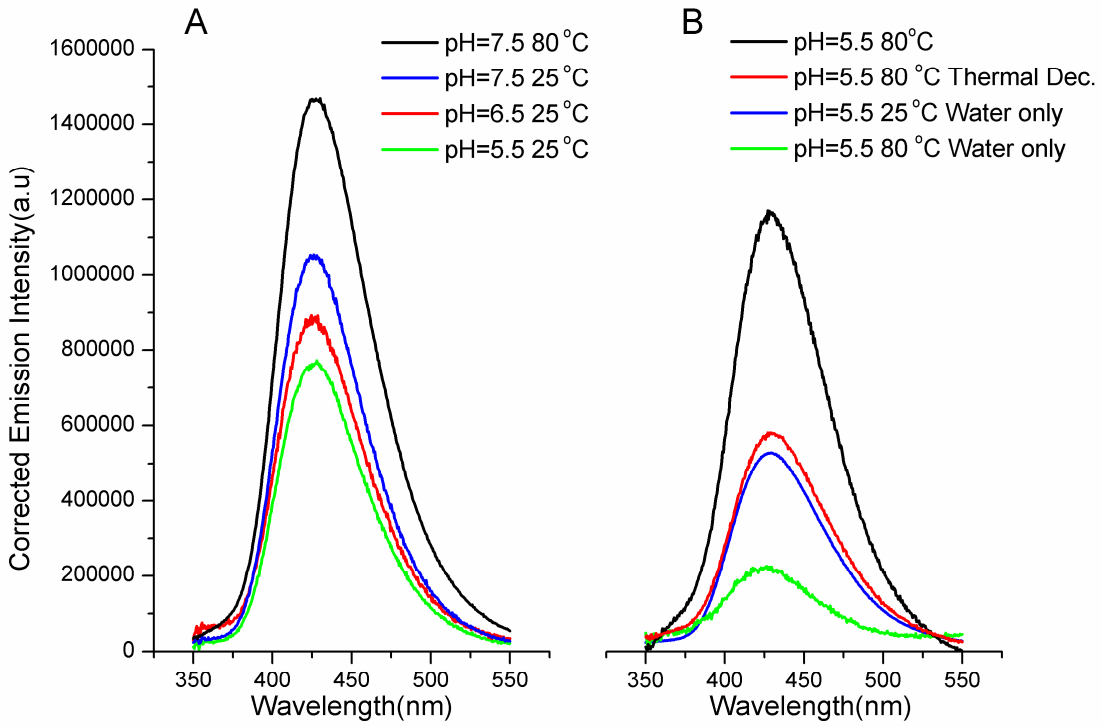

Figure 1. 10 The emission spectra of 2-hydroxyterephthalate under various experimental conditions. A) Ultrasonic decomposition at the presence of peroxydisulfate anion at pH 7.5 and 80 °C (black), pH 7.5 and 25 °C (blue), pH 6.5 and 25 °C (red), pH 5.5 and 25 °C (green). B) Ultrasonic decomposition at the presence of peroxydisulfate anion at pH 5.5 and 80 °C (black), thermal decomposition at the presence of peroxydisulfate anion at pH 5.5 and 80 °C (red), ultrasonic decomposition at the absence of peroxydisulfate anion at pH 5.5 and 25 °C(blue), pH 5.5 and 80 °C(green)

In Figure 1.10A, the effect of pH on OH· radical production yield at constant temperature of 25 °C is shown. In a series of experiments, an increase in the yields of the OH· with increasing pH is clearly observed. For comparison, the emission spectrum from 2-hydroxyterephthalate produced at pH 7.5 and 80 °C is also shown. While the yield of the OH· radical increases moderately with increasing pH, the effect of temperature is more significant. In Figure 1.10B, the effect of temperature and the presence of ultrasonic field are demonstrated at constant pH of 5.5. it is shown that although sonication of water alone is enough to generate OH· radicals, the yields are smaller than the solutions containing peroxydisulfate anions. Furthermore, the

fluorescence intensity decreases for water samples sonicated at higher temperatures. This is an expected result and it is discussed in the next section. In the same figure, we also compare the emission spectra of the solutions where peroxydisulfate anion was decomposed thermally and ultrasonically both at 80 °C and a pH of 5.5. As expected, ultrasound accelerates the OH· radical production rate, as evidenced by the almost 100% increase in the emission intensity of 2-hydroxyterephthalate. One can also conclude that with increasing temperature, the contribution of water cleavage to the overall OH· radical production decreases.

The morphologies of the crystals are controlled by both structural and kinetic effects (growth and dissolution). If the crystal structure is highly anisotropic, the differences in monomer addition rate to the different facets of the crystal could lead to different morphologies. In a similar way the difference of the availability of the monomers for the growth in different facets of the crystal could create many crystals with different morphologies. The facets [100], [210] and their variants are aligned with the crystallographic a-axis. These facets require both SO_4^{2-} and OH^- anions to grow. On the other hand, growth in the b-direction requires only OH^- anions. Contrary to the expectations, peroxydisulfate anion does not only act as the source of sulfate anions, but it generates the hydroxide anions through radical reactions, as well. In addition to reported reactions of the peroxydisulfate anion in the literature, the homolytic cleavage of the water and brochantite formation reactions are given in Reaction 1.3 to 1.10. The reported rate constants for sonochemical decomposition of peroxydisulfate ranges from 8.5 s^{-1} at 25 °C to 150 s^{-1} at 75 °C. Below, for the decomposition of peroxydisulfate, we used the value at 75 °C for the ultrasound assisted rate constant [45]. Other rate constants are the reported rate constants for thermal reactions [46-48]. The thermal and

ultrasonic decomposition of persulfate yields sulfate radical ($SO_4^{-}\cdot$) below pH 7 (Reaction1.3).

$$S_2O_8^{-2} \xrightarrow{k_1} 2SO_4^{\bullet-} \quad k_1 = 150\ M^{-1}s^{-1} \qquad \text{(Reaction1.3)}$$

$$2SO_4^{\bullet-} \xrightarrow{k_2} S_2O_8^{2-} \quad k_2 = 4\times10^{8}\ \text{M}^{-1}\ \text{s}^{-1} \qquad \text{(Reaction 1.4)}$$

$$SO_4^{\bullet-} + S_2O_8^{2-} \xrightarrow{k_3} SO_4^{2-} + S_2O_8^{\bullet-} \quad k_3 = 6.1\times10^{5}\ \text{M}^{-1}\ \text{s}^{-1} \qquad \text{(Reaction 1.5)}$$

$$SO_4^{\bullet-} + \text{OH}^- \xrightarrow{k_4} SO_4^{2-} + HO^{\bullet} \quad k_4 = 6.5\times10^{7}\ \text{M}^{-1}\text{s}^{-1} \qquad \text{(Reaction 1.6)}$$

$$SO_4^{\bullet-} + H_2\text{O} \xrightarrow{k_5} SO_4^{2-} + HO^{\bullet} + H^{+} \quad k_5 = 2\times10^{-3}\ \text{M}^{-1}\text{s}^{-1} \qquad \text{(Reaction 1.7)}$$

$$HO^{\bullet} + S_2O_8^{2-} \xrightarrow{k_6} OH^- + S_2O_8^{\bullet-} \quad k_6 = 1.2\times10^{7}\ \text{M}^{-1}\ \text{s}^{-1} \qquad \text{(Reaction 1.8)}$$

$$H_2O \xrightarrow{k_7} HO^{\bullet} + H^{\bullet} \quad k_7 = 3.3\times10^{-7}\ \text{M}^{-1}\text{s}^{-1} \qquad \text{(Reaction 1.9)}$$

$$4Cu^{2+} + SO_4^{2-} + 6OH^- \rightarrow Cu_4(OH)_6SO_4 \qquad \text{(Reaction1.10)}$$

The sonolytic cleavage of water to OH· and H· (Reaction 1.9) has been studied extensively to optimize the best ultrasonic irradiation conditions. Even though the 80% of the produced OH· and H· radicals has been estimated to recombine [49] , the rate or yield of this reaction is reported by the hydroxylation of terephtalate [39, 40] , degradation of organic compounds[50, 51], Fricke dosimetry [52] and H_2O_2 yield [53]. It was reported that OH· radical and H_2O_2 production rate constants at 20.2 kHz in the presence of saturated O_2 are 0.0699 and 0.204 μM min^{-}1, respectively[54].

Once the $SO_4^{-}\cdot$ radical is formed, it can participate to the Reactions 1.5, 1.6 and 1.7. Reaction 1.6 occurs mostly in basic medium and the OH· radical concentration is reported to be higher than $SO_4^{-}\cdot$ radical above pH 9. The Reaction 1.7 is a quite slow reaction and the rate is independent of pH [46]. The OH· radical formed in Reactions 1.7 and 1.9 reacts with persulfate ion to form OH^- anion by reaction 1.8. The reaction

1.5 produces SO_4^{2-} anion by the reaction between $SO_4^{-}\cdot$ and persulfate anion. The crystal morphology is determined by the formation rate of the OH^- anion and SO_4^{2-}. Therefore, the rate of these reactions in different pHs and temperatures influence the morphology of the crystal.

When we look at the effect of pH the Reaction 1.6, it is more sensitive to change of pH. Since OH^- is one of the monomers that compose the crystal, the competition between the precipitation reactions (Reaction 1.10) and Reaction 1.6 may affect the morphology of the crystal. The increase of the rate of the Reaction 1.6 as a function of pH is reported in the literature[46]. Thus, increase in pH may increase the production rates of $OH\cdot$ radical and SO_4^{2-} anions. This behavior is observed in both terephtalate reactions and TG analyses. Increase in pH increases the $OH\cdot$ radical yield (Figure 1.9A) and the relative sulfate content of the samples produced at high pH are higher. At low pH, the rate of the reaction of the $SO_4^{2}\cdot$ radical and OH^- may decrease and the OH^- may lead in to the precipitation reaction to form OH^- rich crystals. When the rate of the Reaction 1.3 and 1.5 is not fast enough at high pH, the OH^- anion reacts with copper to form copper oxide by chemical dehydration.

When we look at the effect of the temperature, the first thing stands out is the higher differences between initial and final pH at high temperatures. This difference may be due to the increase in the rate of reaction between the $SO_4^{2}\cdot$ radical and water (Reaction 1.7). The higher emission at high pH and high temperatures of 2-hydroxyterephtalate and the higher sulfate content of the needle form supports this result. At low temperatures the persulfate is decomposed only by ultrasonic effect. Also, at high temperatures, the collapse of the cavitation is less violent and it decreases the $OH\cdot$ radical yield [7]. 2-hydroxyterephtalate emission in water without addition of

persulfate decreases with the increasing temperature (Figure 1.9B). However the production of the $OH\cdot$ radical by the Reaction 1.6 is increased since the decomposition rate of the sulfate radical is increased.

To sum up, the relative rates of the reactions that yield OH^- and SO_4^{2-} anions may influence the morphology of the final product. At high temperatures and high pH the total organic content is higher but the relative amount of the OH^- compared to SO_4^{2-} amounts is lower. This fact can be seen both from the XRD and TGA results. A possible reaction mechanism for this is the competition between the precipitation reaction and the reactions that contain $SO_4^{2}\cdot$ radical.

CONCLUSIONS

In this part of the thesis, we utilize ultrasound to synthesize crystals with different morphologies without using any surfactants. New morphologies such as brick, belt and flower are not reported previously in the literature by any other method. The morphologies of the products are controlled by changing the reaction kinetics. A possible crystal growth and reaction mechanism is given by using X-ray diffraction, thermogravimetric analysis and fluorescence probe. Peroxydisulfate is used as a source for both sulfate anion and hydroxide anion. The different morphologies of the crystals are explained by both crystal growth models and the kinetic of the reactions. The reaction mechanism is quite different from the reactions used to synthesize copper hydroxysulfates in the literature. With this reaction mechanism, these morphologies of the brochantite can be obtained only by using ultrasound. The products from this study can potentially be used to investigate the antibacterial and antifungal properties of different morphologies of Brochantite. We would like to thank Hüseyin Enis Karahan

for his idea of analyzing the effect of morphology to the antibacterial and antifungal properties of brochantite.

Chapter 2

Sonochemical Deposition of Silica Particles on Titanium

INTRODUCTION

2.1 Properties of Titanium

Titanium received its name from the Titans that are the powerful sons of the Earth in Greek mythology. It has an atomic number of 22 and an atomic weight of 47.9 g/mol. Titanium has high strength to weight ratio. i.e. has similar strengths as steel but it has weight nearly half of steel. Some of the physical properties of titanium are given in Table 2.1 [55]. Titanium is found in the nature in the form of oxides such as Ilmenite ($FeTiO_3$), Rutile (TiO_2).

Table 2. 1 Summary of physical properties of titanium

Property	Value
Density (g/cm^3)	4.54
Thermal Expansion Coefficient, at 20 °C (K^{-1})	$8.4x10^{-6}$
Thermal Conductivity (W/(m.K))	19.2
Melting Temperature (C°)	1668
Modulus of Elasticity (GPa)	105
Yield Strength (MPa)	692
Ultimate Strength (MPa)	785

Titanium and its alloys are used extensively in aerospace applications, automotive industry, and medical and dental applications [55-59]. As biomaterials, they are used in the replacement of the damaged or diseased parts of the body such as bones and teeth. One of the most important properties of a biomaterial is the interaction with the surrounding tissue. The tissue and biomaterial must coexist without any undesirable effect on each other. Titanium is a biocompatible metal which performs effectively as a host in the body. In addition to this, low modulus and high corrosion resistance compared to the most of the metals make titanium a very suitable implant material [55, 56].

Introduction to Corrosion

Corrosion is the deterioration or change in physical or chemical properties of a material due to chemical or electrochemical processes. The corrosion process in the environment occurs by the direct reaction of the metals with its surrounding materials. Coupled oxidation and reduction reactions occurring at the surface of the metal change the chemical composition which alters the physical properties of the metal. The oxidation and reduction reactions can be separated into half reactions in electrochemistry to study and understand the corrosion process. Cathodic and anodic reactions that are usually observed are given below.

Anodic process: $M \rightarrow M^{+n} + ne^-$ Metal Oxidation

$2H_2O \rightarrow O_2 + 4H^+ + 4e^-$ Oxygen Evolution

Cathodic process: $2H^+ + 2e^- \rightarrow H_2$ Hydrogen Evolution

$O_2 + 2H_2O + 4e^- \rightarrow 4OH^-$ Oxygen Reduction

$M^{+n} + ne^- \rightarrow M$ Metal Reduction

In order to have any corrosion process, one of the anodic and cathodic reactions given above must be present.

The corrosion processes of the metals are mostly examined with Open Circuit Potential (OCP) and Cyclic Voltammetry (CV) measurements. Open circuit potential of the metal is mostly studied to monitor the changes at the surface of the metal in the long run or to reach a quasi-equilibrium state before the cyclic voltammetry measurements. OCP is the potential difference between the metal and of a reference electrode when there is no current passing through the system. From the changes in the potential to the negative or positive directions, corrosion behavior of the metals in the desired medium can be predicted. The negative change in OCP measurements is observed due to release of metal ions in to the solution. Release of positive metal ions leave a more negative metal behind when they go in to the solution. The change in negative direction is observed due to formation of protective oxide layer at the surface of the metal. In CV measurements, the potential of the electrode is changed linearly versus time with a desired scan rate (mV/s). The current change is recorded and plotted versus potential. The anodic polarization leads to dissolution of metal ions in to the solution (Metal oxidation reaction). The dissolved ion may react with water to form oxides and hydroxides and adhere to metal to protect it from further corrosion. On the surface of the inert counter electrode, hydrogen gas evolution or oxygen reduction reactions occur depending on the pH and concentrations of the reactants. The CV curves are used to predict the corrosion behavior of the metals or evaluate the quality of the coatings on metals [60].

2.2 Corrosion of Metals

Corrosion is one of the major problems when an implant is introduced into the body. Human body fluid has ~0.9% salt content at pH 7.4 and temperature of 37±1 °C which is very corrosive environment for the metals. The metal has active and passive sites at the surface. When it is in the corrosive environment the surface oxide goes through partial dissolution and repassivation cycles. If the partial dissolution rate is larger than the repassivation rate, metal ions are released into the solution [61]. Dissolution of the metals is accelerated at the presence of proteins and amino acids. Even though the mechanism for the acceleration is not clear, the releases of the ions are accelerated by the increased rate of dissolution. The dissolved ion in the body does not always combine with the biomolecules. It may react with the water immediately to form oxides, hydroxides or inorganic salts which lead to decrease the toxicity [62]. Even though titanium has high corrosion resistance in human body fluid, in the presence of chloride ions and proteins titanium is unstable which causes the release of titanium ions [58, 62-64]. In addition to this the oxide formation is more difficult since the oxygen content in the body fluid is one fourth of the air. Therefore, the corrosion behaviour of titanium has been studied extensively with electrochemical methods including long and short term open circuit potential measurements, voltammetry and electrochemical impedance spectroscopy in the literature[65-67]

None of the metals are totally corrosion resistant even they have protective oxide layer at the surface that kinetically decreases the corrosion rate. The best known corrosion types are pitting corrosion, crevice corrosion and galvanic corrosion.

2.2.1 Pitting corrosion

Pitting corrosion is a type of localized corrosion that causes formation of small holes or cavities on the surface of the metal. The pitting corrosion occurs at the naturally weak points of the metal surface with the local breakdown of the oxide film especially at the presence of chloride ions. Even though other parts of the metal surface is unaffected by this corrosion process, pitting corrosion can initiate stress-corrosion cracking. [68]

Exact mechanism for the pitting potential is not known however there are three mechanisms proposed for the process. The first one is the penetration mechanism in which the chloride ion diffuses through the oxide film and dissolves the titanium. In the second mechanism the chloride ions adsorb on to the metal surface and form complexes with the film. These complexes may dissolve into the solution which causes local breakdown of the film. With this mechanism, the film gets thinner locally in time and pitting corrosion is initiated. In the last mechanism which is known as rupture mechanism, the chloride ions penetrate through the oxide layer from the cracks and reaches to the metal [69].

2.2.2 Crevice corrosion

Crevice corrosion occurs due to geometrical conditions in the metal. The oxygen near to the metal surface is depleted quickly. When some parts of the metal are shielded from the environment, the consumed oxygen can not be refreshed as easy as the parts of the metal open to the environment. Since oxygen participates into the oxidation/reduction reactions at the surface, the potential of metal is more negative

when it is exposed to oxygen. Therefore the shielded parts of the metal become more prone for corrosion (Figure 2.1)[60].

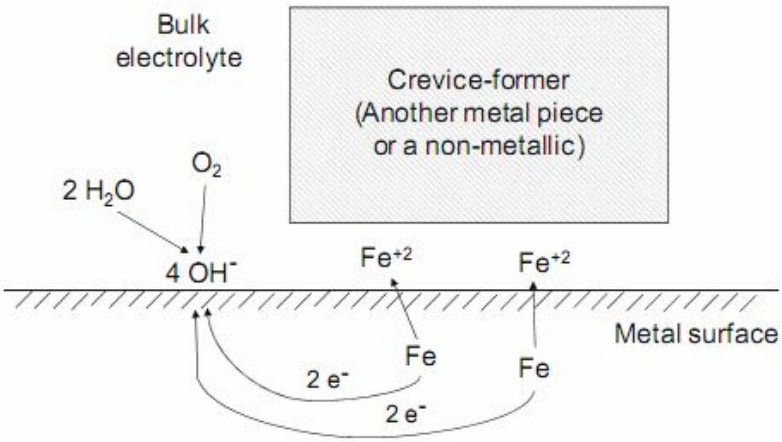

Figure 2. 1 Crevice corrosion of iron [60]

2.2.3 Galvanic corrosion

Galvanic corrosion occurs due to the potential difference between the two different metals in contact. The current flows from the more active metal to the more noble metal. The reason for the galvanic corrosion is not only the potential difference between the metals but also the contact areas of the metals with the liquid. Since in practical applications the contact of two different metals is inevitable, the galvanic corrosion occurs occasionally and it should be considered carefully[70].

2.3 Surface modifications of Titanium

Biocompatibility and corrosion resistance is very essential for implant materials to perform appropriately in the long run. However, the current hot topic in the literature is to bring to the biomaterials another important biological function that is called tissue regeneration or ossointegration [59, 71-75]. When an implant is introduced into the

body, new bone cells grow on the implant surface. After proliferation and differentiation process, the ossointegration completes and the implant is accepted by the body. On the other hand, because of the weak interaction and micromotions of the implant, fibrous tissue can be generated instead of bony interface. This may retard or prevent the ossointegration [76]. It is recently found that the tissue regeneration strictly depends on surface properties such as chemical composition, roughness and topography [77-80].

The composition, roughness and topography of the surface can be modified by coating films onto the metals with chemically inert materials. Since the interaction with surrounding environment is determined by the surface properties of the film, the density, thickness, chemical composition of the film plays an important role in the corrosion resistance, bioactivity and biocompability of the implant. Therefore, various techniques are used to produce films or change the surface properties of the implants in the literature. These methods can be divided into mechanical, chemical and physical methods depending on the film formation mechanisms.

2.3.1 Mechanical Methods

Grinding, polishing, blasting are the common methods to obtain specific surface topographies, roughness and they are used to clean the surface contamination. These methods also can help to increase the adhesion of the film to the metal surface. Even though grinding and polishing are practically similar methods, grinding is mostly used to obtain relatively rough surfaces and for faster polishing. Polishing is performed mostly with high grade abrasive papers and combined with lubrication to end up with very smooth surfaces [81]. Blasting is done by sending high velocity particles to the surface. Shot blasting is one of most frequently used methods for surface cleaning and

roughening in the literature. The cell adhesion and differentiation are reported to be stimulated at the presence of shot blasted particles [82]. In addition to this, the heterogeneity of the surface can lead to excellent corrosion resistant properties [83].

The chemical methods for the modification of the surface are based on the reaction between the solution and the surface of the titanium by using acids, bases, hydrogen peroxide, and inorganic precursors.

2.3.2 Acid treatment

Acid treatments are used to clean the contaminations from the surface. Hydrochloric acid is one of the best decontamination agent used in the literature. These pre-treatments lead to formation of thin oxide layers below 10 nm [84]. On the other hand, recent reports show that the acid treated metal surfaces show much better bioactivity since it changes the surface roughness and topology dramatically [80]. Introducing hydrogen peroxide into the system results with the formation of amorphous titania gel at the surface and these surfaces induce the formation of hydroxyapatite at the surface [85, 86]. Mixture of H_2SO_4 and H_2O_2, known as piranha solution, is used to create chemical interaction between the deposited films and titanium and modify the surface topography of the metals [87]. Piranha treatment of titanium yields an amorphous and porous titania layer on titanium. The oxygen to titanium ratio is found to be around 2 and 2.65 for piranha treated titanium and polished titanium respectively [88]. The difference is attributed to the contamination of carbon compounds. Therefore, piranha activation not only yields a pure titania film on the surface but also cleans up the surface. The piranha treated surface is reported to be much more reactive compared to the untreated surface [89]. Martin et al. used aminopropyltriethoxysilane (APTES) to

functionalize the surface of titanium and they observed that the number of Si-O-Ti bonds dramatically increased with the piranha treatment [90].

2.3.3 Sol-Gel Coatings

Sol-gel chemistry has been proven successful for the synthesis of ceramic oxides, sol-gel silicate powders, organic-inorganic hybrid materials, and sol-gel thin films [91-94]. The method can also be used for coating materials. It has several advantages such as low cost, low temperature production, large variability in products and environmentally friendly synthesis conditions. These advantages make the sol-gel coatings a viable choice compared to the physical vapor deposition, chemical vapor deposition, electrochemical deposition, and plasma spraying techniques [95].

First preparation of silica particles from tetraalkyl orthosilicates ranging 500 nm to 2 μm is introduced by Stöber et al. in 1968 [96]. Basically in this reaction, tetraalkyl orthosilicates undergo hydrolysis and condensation reactions in the presence of water, forming siloxane network in neutral pH. This reaction can be accelerated in the basic or acidic conditions. Single hydrolysis, water and alcoholic condensation reactions can be written as follows respectively [97].

$$\equiv \text{Si-OR} + H_2O \rightarrow \equiv \text{Si-OH} + \text{ROH} \qquad \text{Reaction 2.1}$$

$$\equiv \text{Si-OH} + \equiv \text{Si-OH} \rightarrow \equiv \text{Si-O-Si} \equiv + H_2O \qquad \text{Reaction 2.2}$$

$$\equiv \text{Si-OR} + \equiv \text{Si-OH} \rightarrow \equiv \text{Si-O-Si} \equiv + \text{ROH} \qquad \text{Reaction 2.3}$$

After the hydrolysis and condensation reactions; dimers, trimers, oligomers and rings are formed (Figure 2.2). When sufficiently large number of Si-O-Si bonds is formed

they are called colloidal particles or sol. The colloidal particles can be extracted from the solutions as powders. Further reaction leads to formation of three dimensional networks of colloidal particles by the crosslinking between particles. This macroscopic structure is called "gel". The crosslinking depends on the stability of the colloidal particles or polymeric structures. The stability of these colloids is provided by the static charges at the surface depending on the pH. Since in low and high pH the surface is positively or negatively charged the crosslinking between the colloids are slow compared to the neutral pH [98].

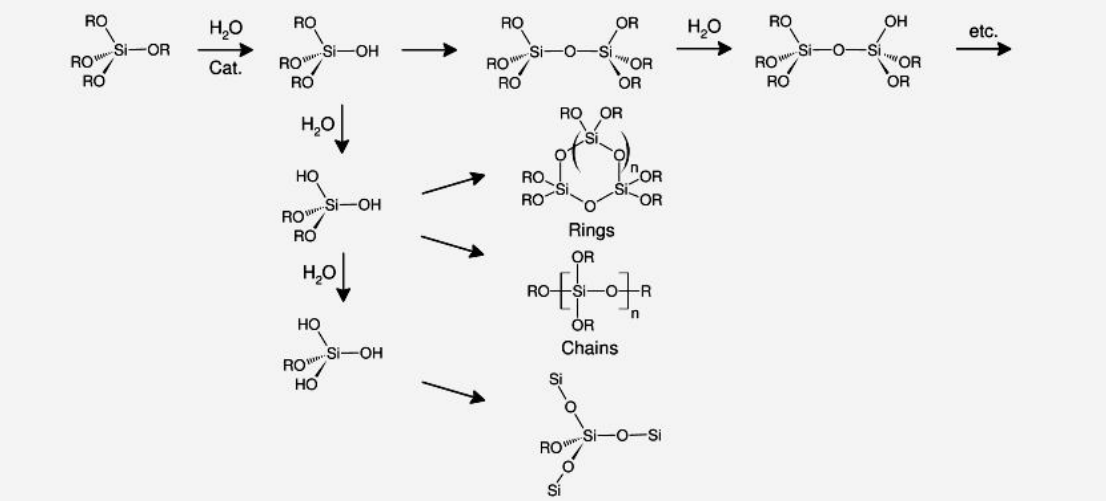

Figure 2. 2 Systematic illustritation of formation of dimers trimers, rings and chains from Tetraethyl orthosilicate [98].

The kinetic of this reaction or the functionality of the silica particles can be changed by using organosilanes. Organosilanes such as aminopropyltrimethoxysilane ($H_2N(CH_2)_3Si(OCH_3)_3$), dimethyldichlorosilane ($Si(CH_3)_2Cl_2$) methytriethoxysilane ($CH_3Si(OCH_3)_3$) etc. contain one or more groups connected to silicon atom that can not be hydrolyzed.

Inorganic coatings, organic-inorganic coatings, inorganic mixed coatings are used to coat metals to improve corrosion resistance and bioactivity [97]. Inorganic coatings are the first type of coatings that are made in the literature such as TiO_2, ZrO_2, SiO_2 [99, 100]. The titania coating was reported as an effective coating for inducing the hydroxyapatite, calcium phosphate formation which can increase the binding of the implant to the bones and corrosion resistance [85, 101, 102]. Li et al. coated NiTi by using sol-gel dip coating technique with titania. The film thickness is around 200 nm and it enhances the corrosion resistance significantly. Titania precursors for the coatings are obtained from titanium alkoxides by the hydrolysis and condensation reaction. However, great care must be taken in handling titanium alkoxides, since they hydrolyze very fast at the presence of water [97]. Silica coatings are reported as an effective coating to induce the nucleation and growth of hydroxyapatite [103]. The silanol groups are responsible for the growth of hydroxyapatite at the surface of the films since they attract the CaO and P_2O_5. Vasconcelos et al. [104] reported silica coatings with thicknesses ranging from 50 to 120 nm which improves corrosion resistance. The corrosion current density decrease when the annealing temperature is increased. Cracks are formed when thick sol-gel films are produced and annealed at high temperatures. These cracks lead to local breakdown of the film by pitting corrosion. If the thermal expansion coefficient is quite different from the coating, cracks are formed even in very thin coatings[105]. On the other hand, the inorganic coatings have very good adhesion with the metal via van der walls interaction. Covalent bonds can be formed by annealing the sample[106].

The composite coatings are formed by using an organosilane or a polymer in addition to metal alkoxide precursor. The major advantage of the composite coatings is

production of thick, crack free films upon annealing. The thickness of the film is reduced with the increasing annealing temperature. This is a result of further water and alcoholic condensation reactions. The crosslinking also creates stress in addition to the capillary pressure due to solvent vaporization. The groups than can not be hydrolyzed in organosilanes prevent the formation of new M-O-M bonds (M:Si, Ti, Zr etc..) which will decrease the stress on the film. The stress evolution upon annealing on silica and silica-organic (MTES) composite films is given Figure 2.3[107].

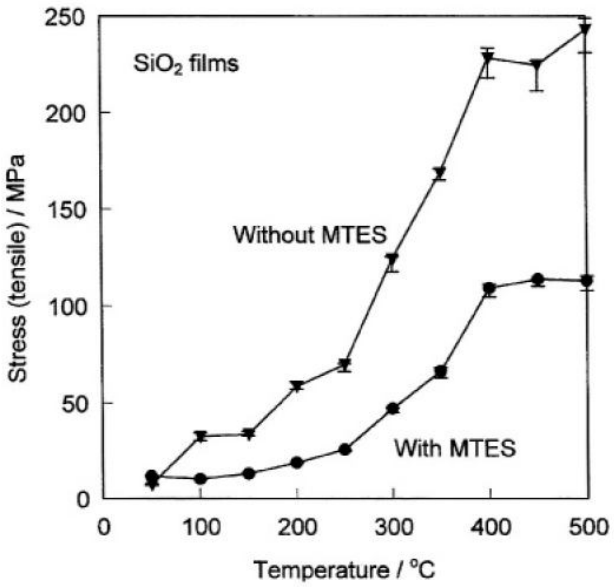

Figure 2. 3 Stress evolution on silica films upon annealing measured by optical deflection [107]

2.4 Sol-gel Coating Techniques

Dip coating is one of the oldest techniques used to coat materials mainly for research purposes. The microstructure can be controlled by controlling the liquid precursor sol properties. In this technique, basically, the sample is dipped into the solution and withdrawn with a constant speed. After gravitational draining and solvent evaporation the film is deposited onto the sample. Nazeri et al. coated stainless steel with titanium and cerium oxide mixed coating by using dipping technique[108]. In

order to prevent crevice or pitting corrosion, the samples are heat treated. Heat treated samples show better corrosion resistance compared to bare steel. Metroke et al. coated aluminum alloy substrate with a composite coating using an organosilane and TEOS as precursor[109]. Dip coated samples which are annealed at 600 °C shift the corrosion potential to the more positive direction and the sample microstructure is controlled by controlling the precursor solution properties.

Spin coating is another widely used method to coat flat surfaces. In this technique, basically, the precursor sol placed onto the center of the substrate and the substrate is rotated at very high speeds. The centrifugal force spreads the liquid to the other parts of the substrate homogenously and thin film is formed on substrate. The properties of the precursor sol such as viscosity, surface tension, vapor pressure of the liquid and the spinning conditions such as rotation speed, acceleration will affect the final thickness and properties of the thin film [97]. Fallet et al. prepared silica, titania and mixed silica-titania coatings on steel substrate by using spin coating method[110]. By using cyclic voltammetry technique, they found that the silica and titania coatings form a better barrier to the release of titanium ions compared to the composite coatings. Chen et al. used spin coating method to prepare different inorganic nanostructured coatings on aluminum [111]. Alumina, SiC, zirconia coatings show excellent corrosion resistance in 1 N sodium hydroxide and 1N potassium chloride and corrodes in 1N hydrochloric acid after 1 hour.

Dip and spin coating techniques are relatively simpler techniques but they can not be used to coat substrates with complex shapes. Therefore they are mainly used for research purposes. Electrochemical deposition is a very promising technique to produce sol-gel coatings. The microstructure and the properties of the final film can be

controlled by controlling the pH, precursor solution properties, deposition voltage and current density. By using electrochemical deposition crack free, thick films can be produced on complex shaped substrates [112].

2.5 Sonochemical Approach

Tarasevich reported a sol-gel reaction in the absence of common solvent by irradiating the water and TEOS mixture with high power ultrasound in 1984 [113]. Ultrasonic waves can induce the formation of small bubbles, i.e. cavitations in the liquid, which collapse and create local high temperatures and high pressures [114]. Under these conditions, the hydrolysis and condensation reactions can occur rapidly to form a homogeneous sol. The gel that is formed from this sol is called as "sono-gel". The sono-gel is dense due to the increase in hydrolysis rate and crosslinking [115]. There are many studies to analyze the structural properties of these sonogels in different inorganic materials such as SiO_2, TiO_2 and ZrO_2 [115-119]. However, these studies are concentrated onto the gels and no sonochemical approach is reported to prepare sols or powders in the literature.

The cavitational collapse at the neighbourhood of a solid boundary is quite different from the collapse in the pure liquid. The collapse occurs non-spherical near the solid surface and drives high-speed jets of liquids into the surface (Figure 2.4).

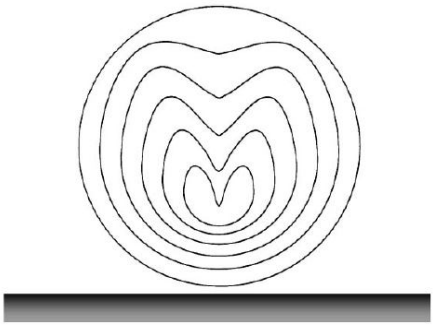

Figure 2. 4 Unsymmetrical collapse of the cavitation near a solid surface

Highly reactive surfaces and newly exposed areas are created when the accelerated jet crashes onto the surface. However the non-spherical collapse of the bubbles occurs if the length of the surface is several times larger than the resonant size of the bubble which is few microns. Therefore, this effect can not be obtained when colloids are present in the solution [120]. When the colloids or powders present in the solution, the shockwaves and turbulent flow lead to high velocity inter-particle collision. The particles collide in such velocities so when they collide, melting occurs at the interface and the particles fuse together (Figure 2.5) [4].

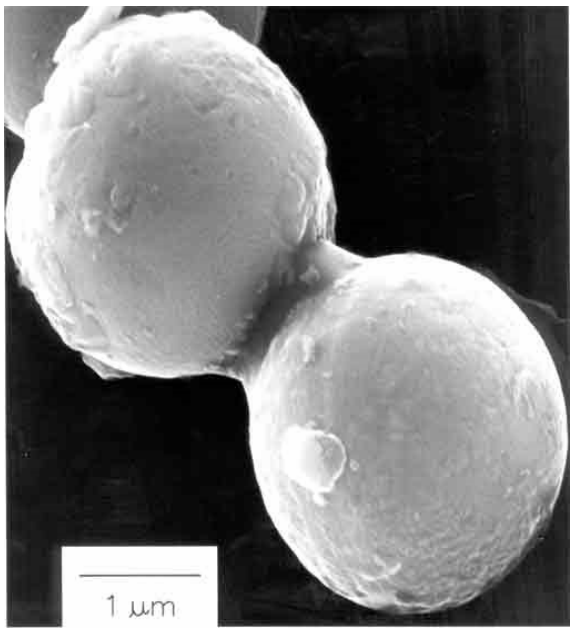

Figure 2. 5 Fusion of Zinc colloids under ultrasonic field [4]

When the solutions are irradiated with ultrasound, acoustic pressure is exerted on the molecules in addition to the hydrostatic pressure. The mean position of the molecules changes when the liquid is irradiated with ultrasound. The acoustic pressure applied to the molecules change with applied intensity of the ultrasound. In order to find the change in acoustic pressure during the compression and expansion cycles following relation can be used.

$$I = \frac{P_A^2}{2\rho c} \qquad \text{Equation 2.1}$$

Where I is the intensity of the sound wave, P_A is the amplitude of the acoustic pressure, ρ is the density of the solution, c is the velocity of the sound in the medium. The maximum velocity as a function of pressure amplitude and the displacement amplitude are given by the Equation 2.2 and 2.3.

$$v_0 = \frac{P_A}{\rho c} \qquad \text{Equation 2.2}$$

$$x_0 = \frac{v_0}{2\pi f} \qquad \text{Equation 2.3}$$

The acceleration amplitude can be written in terms of displacement amplitude by the following equation.

$$a_0 = 4\pi^2 f^2 x_0 \qquad \text{Equation 2.4}$$

By using the Equations 2.1, 2.2, 2.3 and 2.4, maximum velocity, displacement and acceleration of the particles can be found if the intensity of the ultrasound given into the solution is also known [121]. To give an insight about the velocity and acceleration that

the particles can reach under ultrasonic field, the Equations 2.1 to 2.4 are used to calculate the pressure amplitude, maximum velocity, displacement amplitude and acceleration of the particles. If ultrasonic field with intensity of 50 W cm^{-2} and a frequency of 20 kHz is applied to water solution, the acoustic pressure changes twenty thousand times per second from 12.25 atm to -12.25 atm which is calculated by using Equation 2.1. By using the equation 2.2, 2.3 and 2.4 the maximum velocity, displacement amplitude and acceleration are found as 0.82 m/s, 6.5 μm and 10^5 m s^{-2} respectively. The acceleration of the particles under ultrasonic field is approximately10^4 times higher than the acceleration due to gravity. The particles are accelerated and decelerated in micron size distances by the effect of the ultrasonic field.

The synthesis and deposition of different particles can be combined under ultrasonic field in a one pot reaction. The first depositions by utilizing ultrasound have not performed on substrates as expected. The ultrasonic deposition process is first used to coat or deposit particles onto the submicron particles [122-126]. Pol et al. deposited silver and gold nanoparticles on the silica spheres by using ultrasound. The silica particles and silver particles are synthesized separately and dispersed in the same solution for the deposition process. However, the deposition and synthesis of gold nanoparticles are performed in the same solution. Uniform silver and gold coatings are obtained in relatively short amount of time [122, 126]. Dang et al. coated magnetite particles with silica by using ultrasonic irradiation. The ultrasonic irradiation provides better dispersion of magnetite particles and accelerates the hydrolysis and condensation reactions. Hydrolysis and condensation reactions of the silica occur simultaneously with the deposition process. Coating highly dispersed magnetite particles lead to formation of

single core-shell silica coated nanoparticles. The method is specified to be an easy, effective and quick way to produce silica coated magnetite particles.

The deposition of particles onto larger substrates i.e. plates, foils, papers emerged immediately afterwards [127-130]. Kotlyar et al. deposited silver nanoparticles on polymeric chips by using sonochemical method [127]. The silver particles penetrated from the surface 20 nm into the polymer chip. The chip is homogeneously coated with silver nanoparticles in a very short amount of time by a one pot reaction. The adherence of the silver nanoparticles to the chip is reported be very high since they are partly buried inside the chip. Perkas et al. deposited silver nanoparticles onto the glass by using sonochemical methods [129]. The silver nanoparticles deposited on the surface homogeneously and the thickness can be changed as a function of time and as a silver concentration in the solution. The synthesis and deposition of silver nanoparticles are performed simultaneously. The deposited nanoparticles are buried into the glass around 60 nm which increases the adhesion even though there is no chemical bonding.

These examples show the success of ultrasonic deposition process on/in to the soft samples. There is only one study published recently applying sonochemical deposition on hard substrates. Soloviev et al. applied the sonochemical deposition process on steel by using silver nanoparticles [131]. However, the adherence of the nanoparticles is not as good as it is in the soft samples. They can be wiped out easily by a tissue paper. The paper emphasizes the importance of the distance between the sample and the ultrasonic horn for a full coverage at the surface.

To the best of our knowledge, there is no study published in the literature that utilizes ultrasound to coat titanium or any other metal with sol-gel coatings. In this study, silica and organically modified silane coatings on titanium by sonochemical

method for the first time are reported. The effects of reaction kinetics, reaction time, precursor sol, solvent and amplitude of the sound wave to the deposition of sol-gel particles are studied with reflectance measurements, X-ray photoelectron spectroscopy (XPS) and Scanning electron microscope (SEM). The corrosion properties of coated samples are analyzed with open circuit potential (OCP) and cyclic voltammetry (CV) measurements.

2.6 Simulation of Reflectance Spectrum

Reflectivities of the thin films are used to determine the thickness of the thin films especially for multilayer optical films. Therefore, the measurement of the film thickness using the reflected light is a well established technique. In this technique, basically the light is sent to the coated substrate and the reflectance spectrum is recorded. Then the recorded reflectance spectrum is compared with simulated spectrum with the known thickness to estimate the coating thickness.

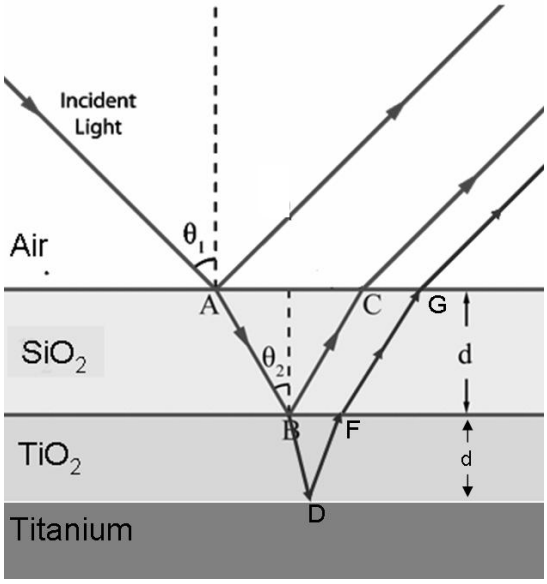

Figure 2. 6 Interference in multilayers

When the light is sent to the substrate, some of it will be reflected from the surface. Some of the light travel inside the coating and reflected back from different levels of the coating (Figure 1.6). The different portions of light will travel different distances so when they are reflected back they will form an interference pattern depending on the thickness and refractive index of the coating[132].

Mathematical Treatment

The reflectance coefficient for a thin film is given by Equation 2.5 [133].

$$r = \frac{Y_0 m_{11} + Y_0 Y_s m_{12} - m_{21} - Y_s m_{22}}{Y_0 m_{11} + Y_0 Y_s m_{12} + m_{21} + Y_s m_{22}} \qquad \text{(Equation 2.5)}$$

Where

$$Y_0 = \sqrt{\frac{\epsilon_0}{\mu_0}} n_0^{'}$$

and

$$Y_s = \sqrt{\frac{\epsilon_0}{\mu_0}} n_s^{'}$$

with $n^{|}_0$ and $n^{|}_s$ being the effective refractive indexes and can be calculated as

$$n_0^{'} = n_0 \cos\theta_0$$
$$n_s^{'} = n_s \cos\theta_s$$

Where θ_0 and θ_s is angle of incident of medium and substrate respectively. n_0 and n_s are the refractive index of the incident medium and refractive index of the substrate. The incident angle of the each medium is calculated by Snell's law. The m_{11}, m_{12}, m_{21}, m_{22}

are the elements of the characteristic matrix, M. If there are p number of layers, the characteristic matrix is shown by Equation 2.

$$M = M_1 M_2 ..... M_p = \begin{bmatrix} m_{11} & m_{12} \\ m_{21} & m_{22} \end{bmatrix} \quad \text{(Equation 2.6)}$$

Individual characteristic matrix for a layer is given by the following matrix.

$$M_x = \begin{bmatrix} \cos\delta_x & (i\sin\delta_x)/Y \\ iY_x \sin\delta_x & \cos\delta_x \end{bmatrix} \quad \text{(Equation 2.7)}$$

The term δ_x stands for phase shift. The phase shift of the wave in xth layer with thickness (d_x) is given by Equation 2.8.

$$\delta_x = k_0 \frac{2n_x d_x \cos\theta_x}{2} \quad \text{(Equation 2.8)}$$

Further simplification of the Equation 2.5 lead to Equation 2.9;

$$r = \frac{n_0' m_{11} + n_0' n_s' m_{12} - m_{21} - n_s' m_{22}}{n_0' m_{11} + n_0' n_s' m_{12} + m_{21} + n_s' m_{22}} \quad \text{(Equation 2.9)}$$

This matrix is a complex matrix, thus the reflectance coefficient is an imaginary quantity. The reflectance can be obtained by multiplying reflectance coefficient with complex conjugate.

The refractive indexes are calculated for each wavelength collected during the reflectance measurement by Sellmeier equation given below [134].

$$n^2(\lambda) = 1 + \frac{B_1\lambda^2}{\lambda^2 - C_1} + \frac{B_2\lambda^2}{\lambda^2 - C_2} + \frac{B_3\lambda^2}{\lambda^2 - C_3} \qquad \text{(Equation 2.10)}$$

Where B_1, B_2, B_3, C_1, C_2 andC_3 are the Sellmeier constants for the material, λ is the wavelength and n is the refractive index.

EXPERIMENTAL PROCEDURE

2.7 Materials and Specimen Preparation

All chemicals were analytical grade and used without further modification. Sulfuric acid (H_2SO_4, 96%-97%), hydrogen peroxide (H_2O_2 ,30%), nitric acid (HNO_3, %65), absolute ethanol (C_2H_6OH), Ammonium hydroxide (NH_4OH, 25%), were purchased from Merck. Tetraethyl Orthosilicate (TEOS,98%), Dodecyl triexthoyxysilane (DTES, 95%) were purchased from Alfa Easer. Acetone ($(CH_3)_2CO$, %99) is purchased from Honeywell. Grade 2 titanium is purchased from Bağ-San A.Ş and cut in to pieces by using water jet.

In a typical procedure, 25mm x 25mm titanium piece is wet polished with 240A, 400A, 600A, 800A silicon carbide papers in increasing grit number. Polished titanium is cleaned in ultrasonic bath for 15 minutes with ethanol and 15 minutes with water. Cleaned titanium piece is dried with a tissue paper and put into piranha solution composed of 70%/30% sulfuric acid and hydrogen peroxide (30%) by volume. The piranha solution is open to atmosphere and extra cooling or heating is not applied to the solution. After 30 minutes of treatment, titanium piece is taken by teflon tweezer and rinsed with excessive water.

2.8 Coating of Titanium via Ultrasonication

For the deposition processes in water, piranha treated titanium piece is placed into the vessel with jacket to control the temperature during the experiment. Then water, ammonia and TEOS are added to reaction vessel respectively. In all experiments, the total volume is fixed approximately to 44 ml. The distance between the ultrasonic horn and the titanium piece is 1 cm for all experiments. The catalyst type and amount, water/TEOS ratio and reaction times are varied and the corresponding amounts are given in Table 2.2.

For the deposition processes in ethanol and acetone the solvent is added into the beaker with ammonia and TEOS. Then the reaction is allowed to run for one hour under magnetic stirring. After 1 hour the reaction solution is put into reaction vessel and the deposition process is started. For the composite coating preparation, TEOS and DTES are added to the solvent and ammonia mixture simultaneously. The total volume is fixed to 44 ml and the distance between ultrasonic horn and titanium piece is adjusted to 1 cm. The reaction time, amplitude of the sound wave, catalyst amount is varied and corresponding amounts are given in tables 2.4 and 2.5.

After all deposition processes, titanium piece is taken out from the solution and put into a beaker filled with water. In order to clean the loosely bounded particles and the reactants adsorbed on titanium, it is sonicated and washed with fresh distilled water for few minutes. Then titanium piece is dried with nitrogen gas and characterized with reflectance spectroscopy, X-ray photoelectron spectroscopy (XPS), electron microscope and electrochemical methods.

2.9 Instrumentation

An ultrasonic probe (Bandelin HD 3200 model, 20 kHz, 200 W) with 13 mm $TiAl_6V_4$ alloy tip is used for the deposition process XPS spectra are recorded with Thermo Scientific K-Alpha spectrometer. Al-K α radiation is used as x-ray source and flood gun is turned on to avoid charging during the measurement. The pressure of the vacuum chamber changes between 10^{-7} to 10^{-8} Torr during the measurement. All of the spectra are corrected by using C1s binding energy 285 eV as reference. In electron microscope studies Zeiss Ultra Plus Field emission scanning electron microscope (FE-SEM) is used. Reflectance spectra are recorded with Ocean Optics HR4000 spectrometer between 500nm-900nm with respect to a silver mirror at a normal incidence. LS-1 tungsten halogen lamp is used as the source of radiation. Light is sent to the substrate and detector by using optical fibers with core diameters of 200 μm and 50 μm respectively. The experimental reflectance spectra are used to estimate the thicknesses of the films by comparing with the simulated reflectance spectra. The reflectance spectra are normalized in order to get rid of the intensity loss due to roughness of the sample. The simulation program and its details are given in Appendix. The simulation is composed of one function and a script that uses that function. Inside the function, the experimental spectrum is imported and the difference between the experimental and simulated spectra is calculated. The script minimizes the differences between the simulated and experimental spectra. The program is fed with possible minimum and maximum thicknesses of silica and titania layers in addition to the angle of incidence and refractive index of the incident medium. Program simulates the reflectance spectrum for each thickness of titania and silica layers and compare it with the experimental spectrum. Electrochemical characterization is done by using Princeton

Applied Research -EG&G Model 273 Potentiostat in a home made special cell. The characterization is done in 0.5 M NaCl (pH 6.5) solution purged with argon for at least 30 minutes. Open circuit potential (OCP) measurements are conducted for 30 minutes. The cyclic voltammetry measurements are done between open circuit potential value and 2.4 V with a scan rate of 10 mV/s. In all measurements, Ag/AgCl in saturated KCl is used as reference electrode and platinum is used as counter electrode.

RESULTS and DISCUSSION

2.10 Deposition in Water: Sono-gel Approach

Even though this procedure is called as sono-gel approach, the reaction parameters are adjusted to avoid gel formation because the travelling of ultrasonic wave in gels can not create cavitation. Therefore, the deposition process is stopped when the sol turns into gel. There are tremendous numbers of studies in sol-gel science including colloids, powders and gels. However, the studies on sono-gel approach are limited to gels. Thus, the discussions will be based on the literature of gels prepared by sono-gel approach.

Series of reactions for base catalyzed, acid catalyzed and not catalyzed reactions are given Table 2.2. (SG stands for Sono-gel)

Table 2. 2 Reaction parameters for ultrasonic deposition in water

No	Temperature (°C)	Amplitude	Duration (Min)	Water/TEOS (Mole ratio)	Catalyst	Catalyst Amount(ml) or pH
SG1	25	70%	60	95	Ammonia	3.3
SG 2	25	70%	120	95	Ammonia	3.3
SG 3	25	70%	30	40	Ammonia	3.3
SG 4	25	70%	60	40	Ammonia	3.3
SG 5	25	70%	120	40	Ammonia	3.3
SG 6	60	70%	120	20	Ammonia	3.3
SG 7	60	70%	120	20	-	-
SG 8	60	70%	120	20	-	-
SG 9	60	70%	120	20	HCl	pH 1.5
SG10	60	70%	120	10	HCl	pH 1.5
SG11	60	70%	120	20	HCl	pH 1.5
SG12	25	70%	15	40	Ammonia	3.3
SG13	25	70%	120	40	Ammonia	3.3

The characterizations of these samples are done by using XPS and reflectance spectra. Unfortunately none of these samples are fully covered at the end of the process. Below in Figure 2.7, photos of bare, piranha treated, and coated titanium pieces (SG3,SG4) with the reflectance spectra are given.

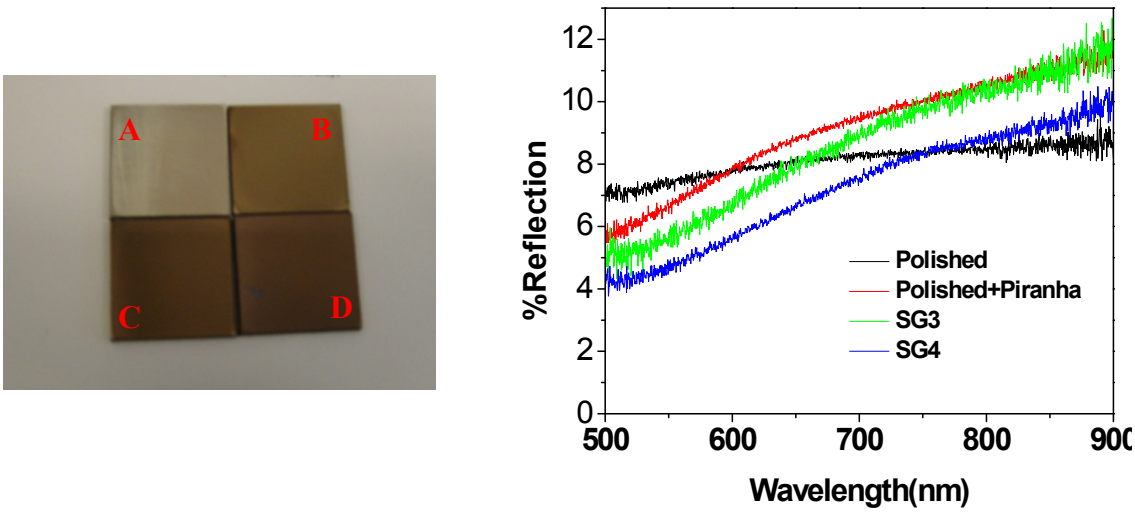

Figure 2. 7 Photo and reflectance spectra of the samples SG3 (C) and SG4 (D) in addition to polished (A) and piranha treated (B) samples.

The reflectance spectra simulations give 8 nm titania, 60 nm silica coatings for both of samples. Decreasing sonication time to 15 minutes or increasing it to 120 minutes did not change the optical properties of the samples indicating that the thickness of the samples can not be changed with increasing sonication time. XPS analyses of these samples show that there is a silica formation on the surface (Figure 2.8B). However, the photoelectrons ejected from the titania layer which is below the silica layer can be still detected (Figure 2.8A). The peaks in Figure 2.8A are assigned to $Ti2p_{1/2}$ and $Ti2p_{3/2}$ of positive titanium with oxidation number of 4 [135]. The photoelectrons are ejected from the titania layer formed during the piranha treatment.

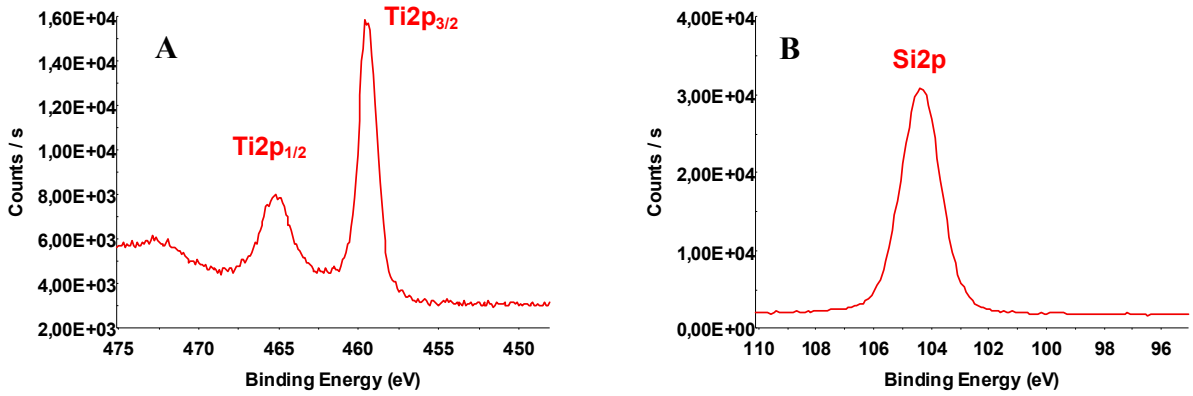

Figure 2. 8 Ti2p and Si2p scans of the sample SG4

The mean free path of the electrons changes 1-5 nm depending on the kinetic energy of the electron. Therefore, by combining the reflectance simulations and XPS results, instead of a thin very thin coating formation (1-5nm) it is concluded that there is not a full coverage of the surface.

Ultrasound increases the reaction and mass transfer rate between two immiscible liquids. Therefore it is used in many heterogeneous liquid-liquid reactions and extraction processes [6]. TEOS and water are immiscible liquids and can be reacted by using a co-solvent at the absence of ultrasound. The unique environment of ultrasound

first increases the hydrolysis rate that occurs at the interface of water and TEOS. With the release of alcohol as a product, rate of hydrolysis and condensation reactions increases since TEOS and water mix at the presence of alcohol [136]. The reported gels produced under ultrasonic irradiation are quite dense compared to conventional gels produced with sol-gel process. In addition to this the gel times are decreased dramatically with the sono-gel approach. The reason behind these observations is the high condensation rate and the high crosslinking density between the produced polymers or colloids [115]. Therefore, during deposition processes the silica particles are deposited at the early time of the reaction and with the start of crosslinking between particles it stops. The formed crosslinked structure may be so large to be deposited with acceleration under ultrasonic field. The displacement amplitude in water for ultrasonic waves with intensity of 50 W cm^{-2} is found 6.5 μm. Therefore, the size of the highly crosslinked structure may be the limiting factor. When the size of the crosslinked structure is comparable with the displacement amplitude, the particles may not be accelerated under ultrasonic field.

Table 2. 3 Some of the physical properties of water, ethanol, acetone

	Surface Tension at 20°C (mN/m)	Viscosity at 25 °C (mPa.s)	Boiling point (C°)
Water	72.8	0.891	100
Ethanol	22.3	1.074	78
Acetone	23.7	0.306	56

In many sonochemical processes water is used as a solvent to synthesize new colloids, polymers, ceramics etc [137]. Also the deposition processes onto soft substrates are shown where water is used as solvent [123, 127]. However, the viscosity and surface tension of the water is relatively high. Also increased viscosity with the formation of

silica particles or polymers could inhibit the cavitation formation. In addition to these the vapor pressure of the water is relatively low which could also increase the cavitation threshold intensity. Therefore, we continued our research by using ethanol and acetone as a solvent in order to fully coat the sample and increase the thickness of the coating. The surface tension, viscosity and boiling point of water, ethanol and acetone is given in Table 2.3.

2.11 Deposition of Silica Particles in Ethanol

When the colloids or powders present in the solution, the shockwaves and turbulent flow lead to high velocity inter-particle collision [4]. Perkas et al. reported the aggregation of silver nanoparticles during ultrasonic deposition [129]. Also, aggregation of silica particles prepared via Stöber method under ultrasonic field is reported. During the silica synthesis, in addition to the ultrasonic effect, the presence of silanol groups at the surface of the silica particles accelerated the aggregation [138]. Running the reactions directly under ultrasonic field causes aggregation very fast especially when acetone is used as the solvent. Aggregates that can be removed easily with tissue paper stick onto the titanium surface and block the further deposition. The particles aggregate before they reach particle sizes that can be deposited. Therefore, in order to prevent the aggregation at the early stage of the reaction, the reaction is allowed to run under magnetic stirring for 1 hour before the deposition process in all experiments. It is worthwhile to mention here that the reaction proceeds also under ultrasonication.

In Table 2.4 series of reactions performed in ethanol is given. All of the parameters are fixed while the reaction time is varied in Eth1, Eth2, Eth3. All of the

reactions are catalyzed with ammonia. The thickness is calculated from reflectance spectrum.

Table 2. 4 Reaction parameters for the deposition process in ethanol

No	Temp. (°C)	Amplitude	Duration (Min)	Solvent	Catalyst Amount(ml)	Extra Water amount	TEOS Amount (ml)	TiO_2 Thickness (nm)	SiO_2 Thickness (nm)
Eth1	25	70%	30	Ethanol	2	-	2	11	67
Eth2	25	70%	60	Ethanol	2	-	2	12	75
Eth3	25	70%	120	Ethanol	2	-	2	11	72
Eth4	25	70%	120	Ethanol	0.5	-	2	8	45
Eth5	25	70%	120	Ethanol	4	-	2	12	85

The reflectance simulations of the samples are given in figure 2.9 and experimental and simulated spectra are matching. Corresponding titania and silica coating thicknesses are also given Table 2.4. The produced films are 15 nm thicker than the films produced via sono-gel approach.

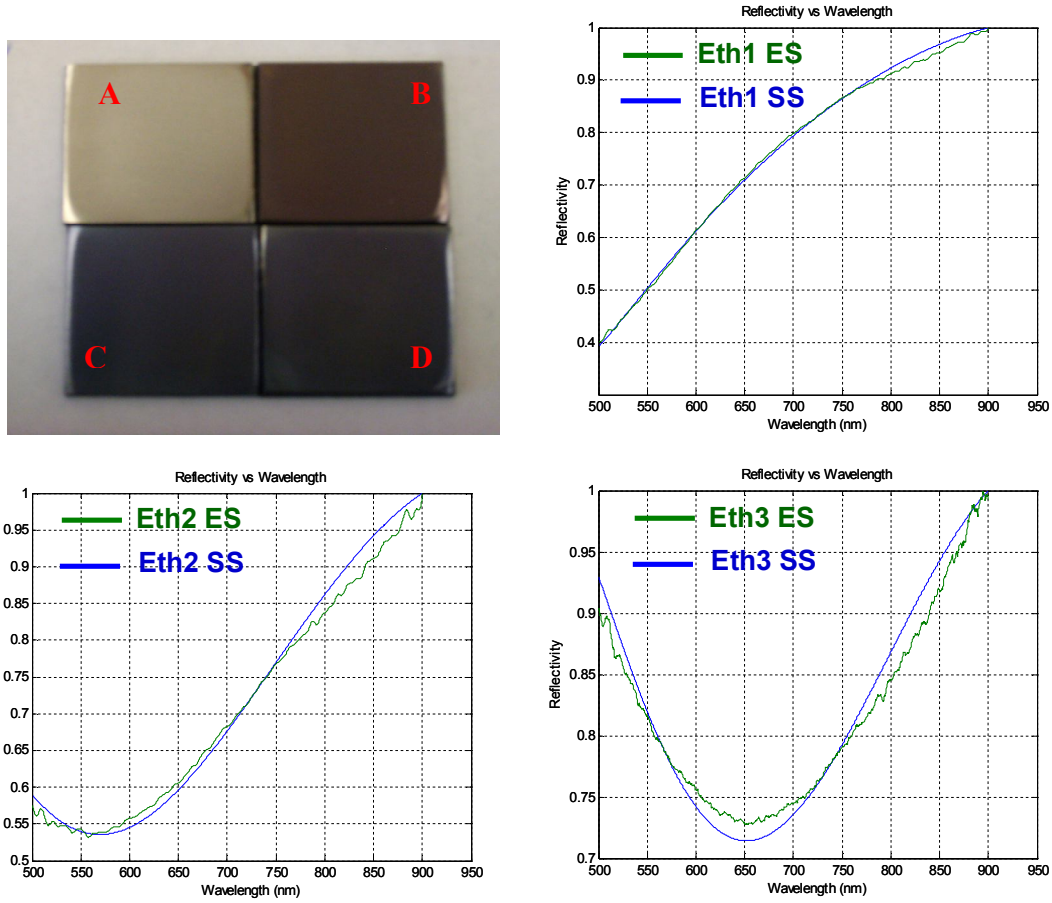

Figure 2. 9 Photo (A: Polished Ti, B: Et1, C: Eth2, D: Eth3) and reflectance simulations of the samples Eth1 Eth 2 and Eth 3. (ES: Experimental spectrum, SS: Simulated spectrum)

Stöber method is a universal and versatile method to produce monodisperse silica particles. The monodispersity of the particles results from the nucleation of the particles at the early stage of the reaction. The growth rate is not affected by the particle size and it continues with the addition of the monomer to the particles which lead to spherical particles. Hydrolysis is the rate determining step even at high water concentrations. Addition of ammonia to the system increases hydrolysis rate since the attack to the silicon is much more rapid at the presence of hydroxyl. Condensation rate is also increased with the addition of ammonia since silanol groups are deprotonated.

Deprotonation of the silanol group also increases the stability of colloids since it creates static charges at the surface of the particles [97].

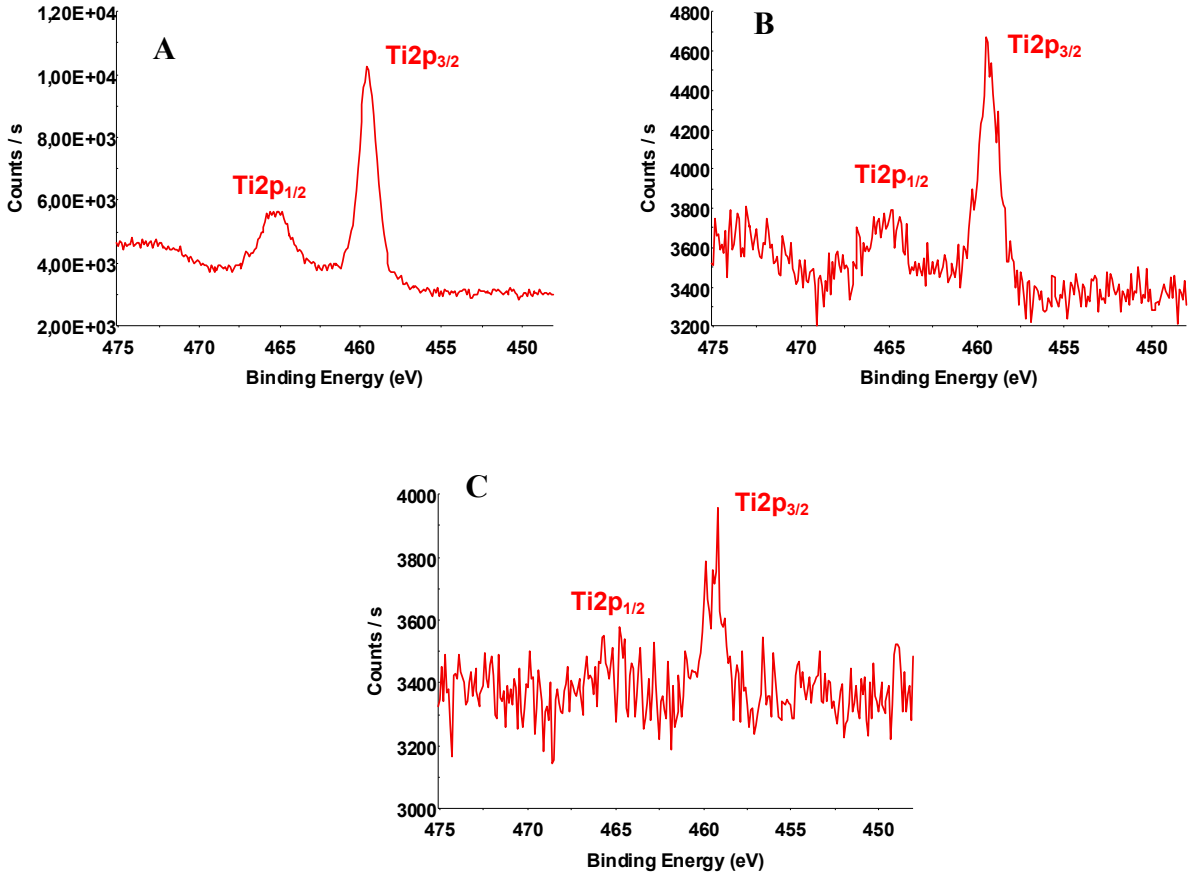

Figure 2. 10 Ti2p Scans of the samples irradiated with ultrasound for A) 30 min B) 60 min C) 120 min (Samples Eth1, Eth2 and Eth3)

In Figure 2.10, XPS spectra of the samples Eth1, Eth2, Eth3 is given. Even after 120 minutes reaction time, photoelectrons coming from Ti^{4+} can still be detected. The signal of titania decreases with the increasing reaction time which can be interpreted as homogenization of the coating. The thickness of the coating does not change significantly after 30 minutes. Instead, the coating is slowly homogenized with a low rate of deposition. FE-SEM image of Eth3 also shows that titanium is coated with 25 nm particles and it is not fully covered (Figure 2.11). The expected particle size is around 50 nm at the end of the reaction [96]. It can be seen from the FE-SEM image

that the size distribution of the deposited particles are quite narrow and larger particles sizes can not be deposited. This is also obvious from thicknesses calculated from reflectance spectra. Viscosity of the solution and the aggregation of the particles may play an important role here. It is known that the viscosity of the sol-gel reactions increases during the reaction and near the gel point it increases dramatically [107]. Even though we are far from the gel point, the viscosity still could increase dramatically due to crosslinking under ultrasound. Created environment only allows certain particle sizes to be deposited onto the surface.

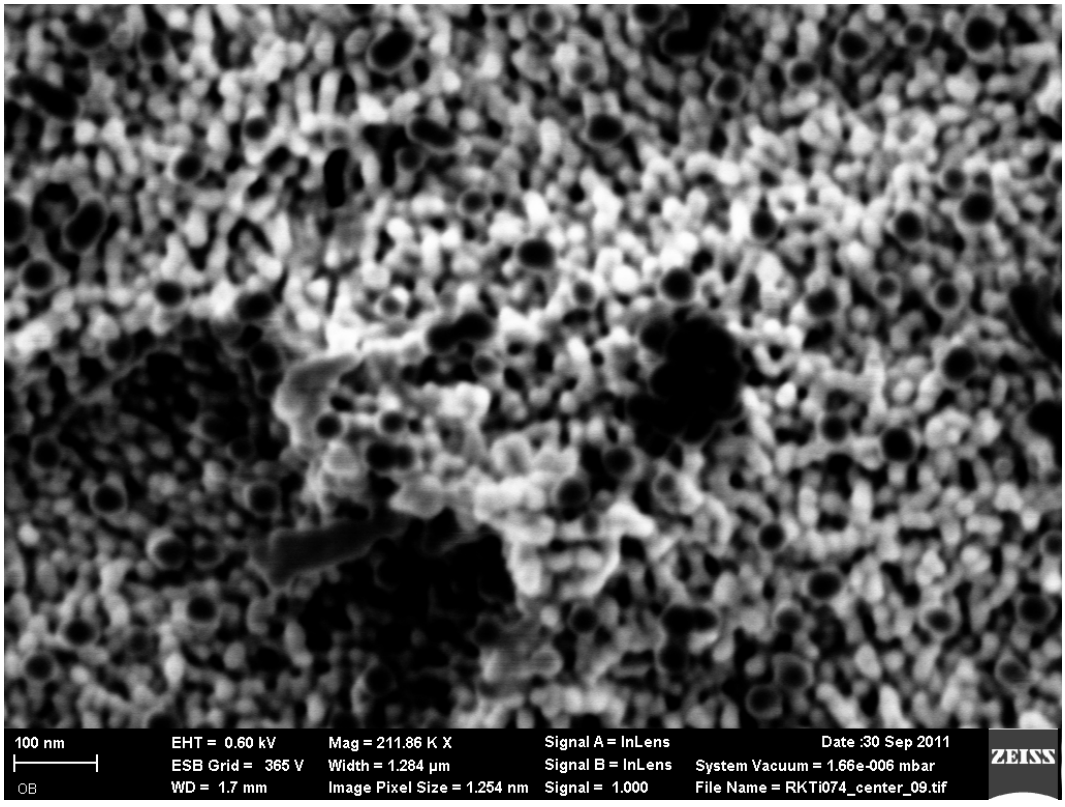

Figure 2. 11 FE-SEM image of the sample irradiated for 120 min (Eth3)

The sizes of the particles hugely depend on the nucleation rate of the particles. High nucleation rate leads to formation of smaller particles whereas low nucleation rate gives larger particles since the growth is favored. Therefore, it is important to know what

factors affect the nucleation and growth. The nucleation is hugely dependent on the hydrolysis rate. We can define nucleation as the reaction between two monomers. Thus increased monomer concentration will result with a high nucleation rate. Therefore, in order to stop nucleation and favor the growth, the hydrolysis rate must be slowed down. The factors that inhibit the hydrolysis will inhibit the nucleation, and favor the growth. Low water concentration favors larger particles since the hydrolysis will be slow. High water concentration favors small particle formation since the hydrolysis rate is fast, or in other words nucleation takes place more rapidly. Increasing ammonia concentration is a little bit challenging. Increase of the ammonia concentration increases the nucleation but also the growth of the particles and lead to formation of larger particles. The faster addition of the monomers to the nucleated particles decreases the nucleation rate since the hydrolysis rate is slow compared to the condensation [139].

Decreasing the ammonia concentration, sample Eth4, decreases the thickness of the coating and does not yield a fully covered surface (Figure 2.12). Since the ammonia and water concentration is very low, the reaction proceeds so slowly. The number of

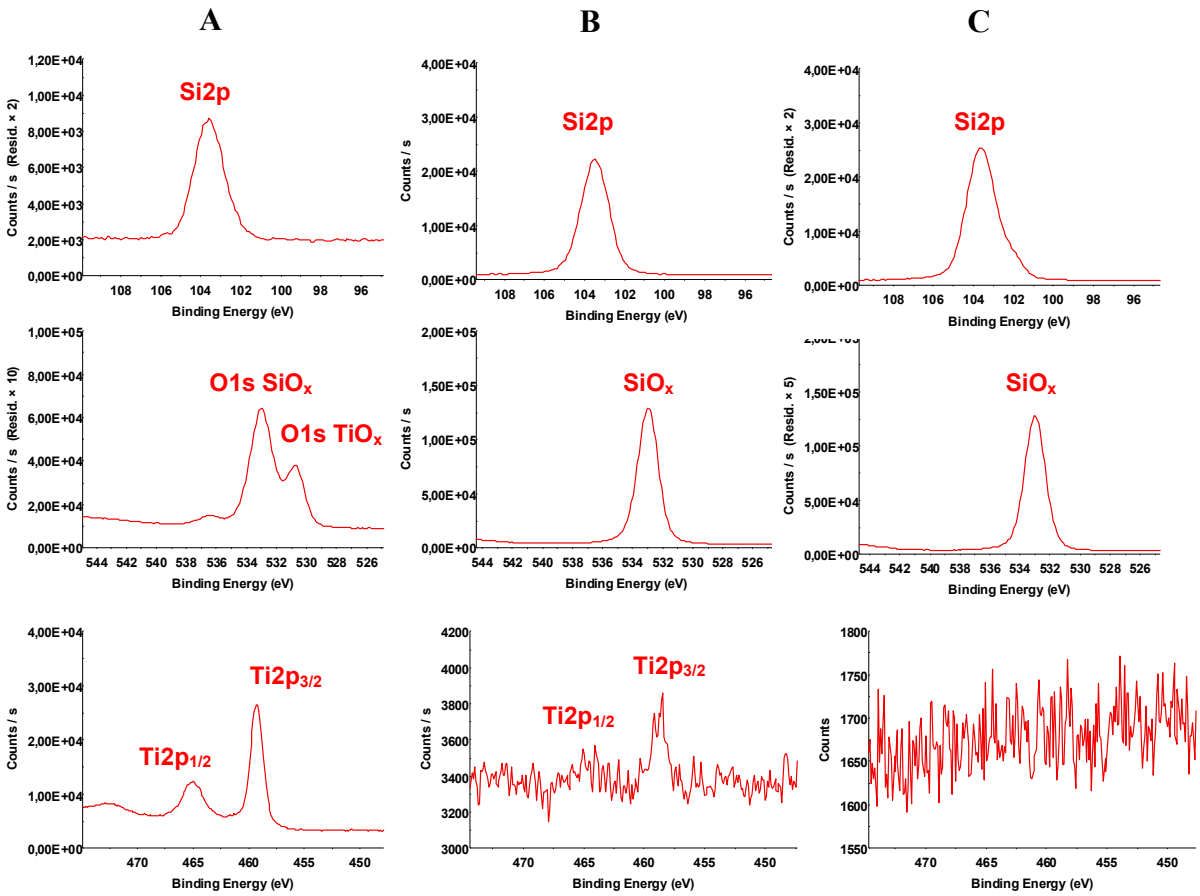

Figure 2. 12 Si2p, O1s and Ti2p scan of the samples as a function ammonia concentration Column A: 0.5 ml (Eth4), Column B: 2 ml (Eth3), Column C: 4 ml (Eth5)

available hydroxide groups to bind chemically to the substrate is small. Increasing ammonia concentration, Eth5, lead to formation of fully covered surface with silica particles. The disappearance of the titanium and oxygen signal (TiO_x) with the increase of ammonia concentration points out homogeneously coated and fully covered surface. Silica particles have an average particle size of 45 nm determined by FE-SEM (Figure 2.13). Since the thickness calculated from the reflectance spectra for Eth 5 is 85 nm, it can be interpreted that the coating is composed of layers of silica particles.

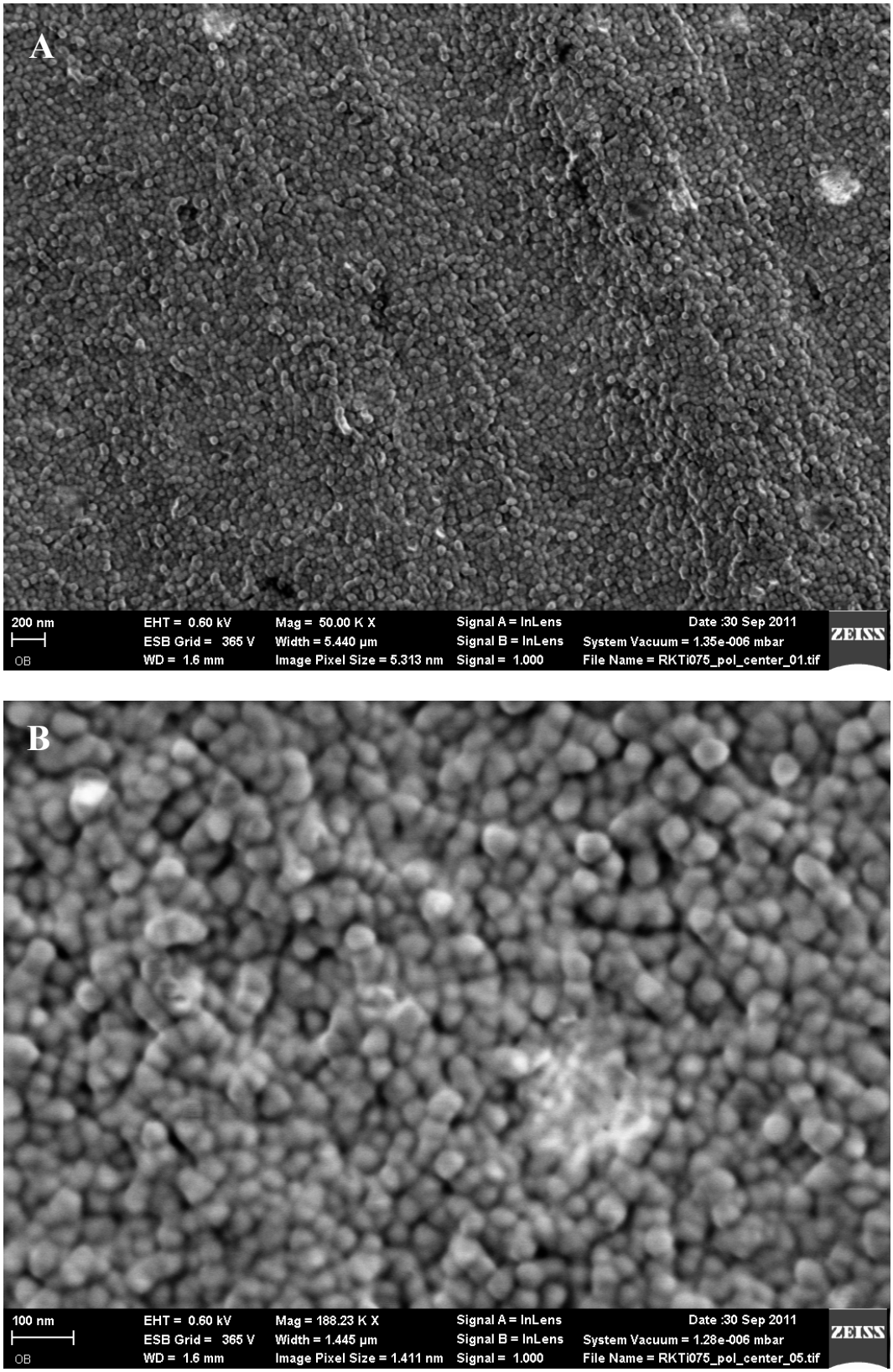

Figure 2. 13 FE-SEM image of the sample Eth5 at low (A) and high (B) magnification

In addition to these, the chemical compositions of the coatings are found to be different at the side and in the middle part of the substrates. An overlaid spectrum of the Si2p scans for the middle and side part of the coatings are given in Figure 2.14. The shoulder of the silicon peaks at the side part of the film has lower binding energy. The electron donating ability of the groups bounded to silicon can be put into descending order as -OCH_2CH_3, -OH, -OSi [97]. Therefore, it can be concluded that the number of Si-O-Si bonds under ultrasonic horn is higher than the other parts of the film. This shows that hydrolysis and condensation rate is higher at the parts close to the ultrasonic horn. Since there is not much difference between the particles in the solution, this shows that the reaction continues within deposited particles under ultrasonic field.

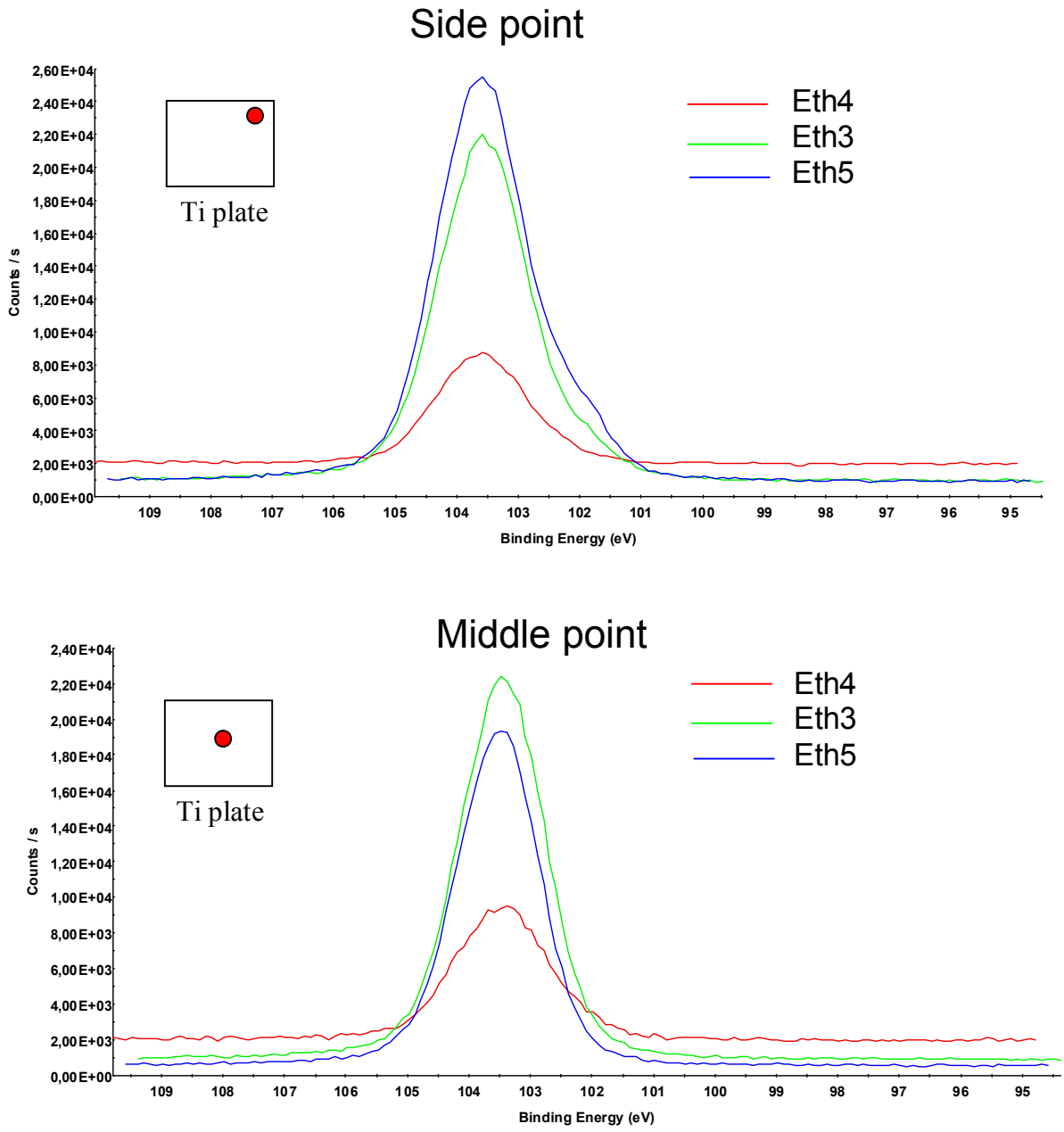

Figure 2. 14 Si2p scans taken from the middle and side part of the substrates

2.12 Deposition of Silica Particles in Acetone

The different reaction conditions are summarized for the deposition processes performed in acetone in Table 2.5. Ammonia is used as the catalyst in all experiments. The reaction conditions are optimized in order to prevent aggregation. Increasing

ammonia or water amount lead to deposition of loosely bound silica particles that block the further growth of the film (Act4, Act5, Act6).

Table 2. 5 Reaction parameters for the deposition process in acetone

No	Temp. (°C)	Amplitude	Duration (Min)	Solvent	Catalyst Amount(ml)	Extra Water amount	TEOS Amount (ml)	TiO_2 Thickness (nm)	SiO_2 Thickness (nm)
Act1	25	70%	30	Acetone	2	0.5	2	12	75
Act2	25	70%	60	Acetone	2	0.5	2	12	163
Act3	25	70%	120	Acetone	2	0.5	2	11	247
Act4	25	70%	Gel	Acetone	2	1	2	-	-
Act5	25	70%	Gel	Acetone	2.5	-	2	-	-
Act6	25	70%	Gel	Acetone	3	-	2	-	-
Act7	25	20%	120	Acetone	2	0.5	2	13	88
Act8	25	40%	120	Acetone	2	0.5	2	14	160

The reflectance spectra of the coated samples for 30 minutes, 60 minutes, and 120 minutes are given in Figure 1.12. The corresponding thicknesses for titania and silica layer are given in Table 1.4. The thickness of the coatings can be changed as a function time. The experimental and simulated spectra match perfectly in each sample. The change in the thickness is also clear from the color of the samples. After 60 minutes, no signal is detected from titania layer below the silica in XPS spectra (not shown in here).

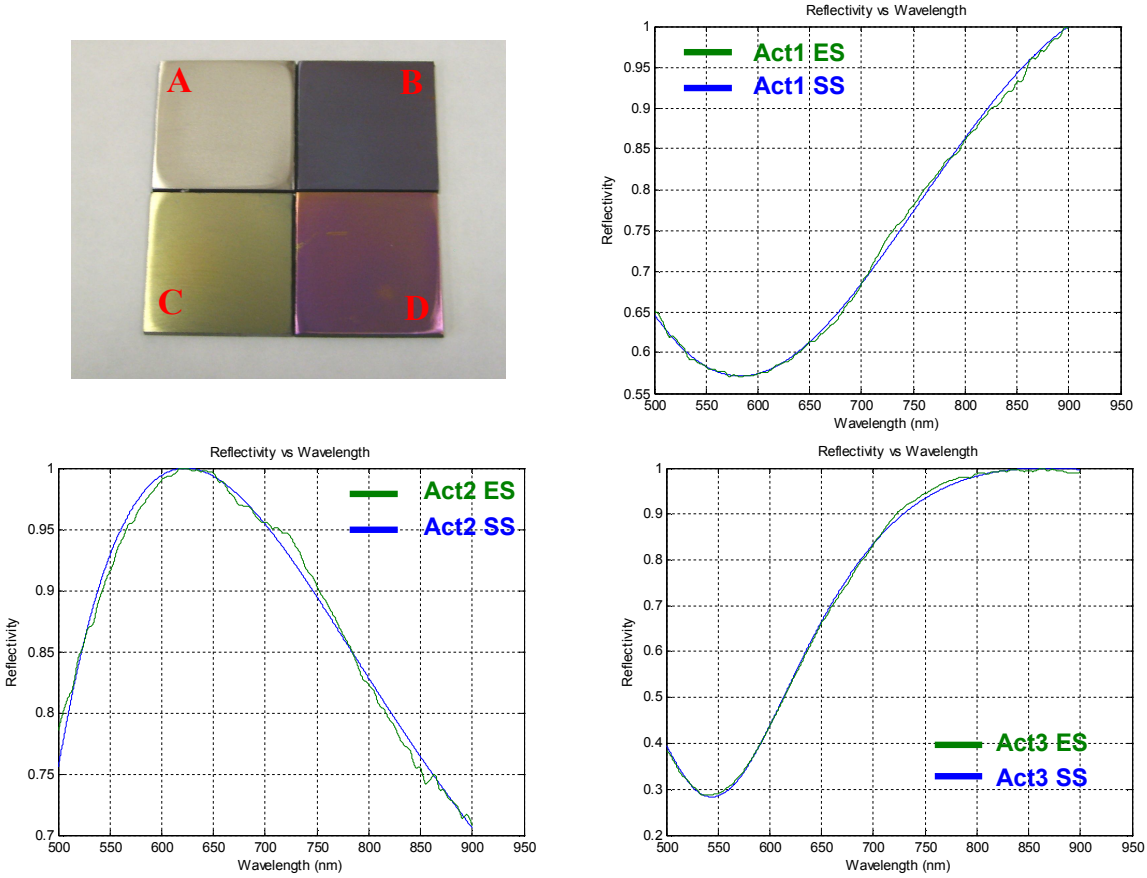

Figure 2. 15 Photo (A: Polished Ti, B: Act1, C: Act2, D: Act3) and reflectance simulations of the samples Ac1 Act 2 and Act 3. (ES: Experimental spectrum, SS: Simulated spectrum)

The FE-SEM images of the samples (Figure 1.13) support the reflectance and XPS results. The sample coated for 30 minutes (Act1) is composed of 25 nm silica particles. The sample is not coated homogenously and detection of titania signal below the silica layer is not surprising. Increasing the deposition time to 60 minutes increases the particle size and homogeneous coatings are obtained. Further increase of the deposition time increases the thickness but does not change the deposited particle size dramatically.

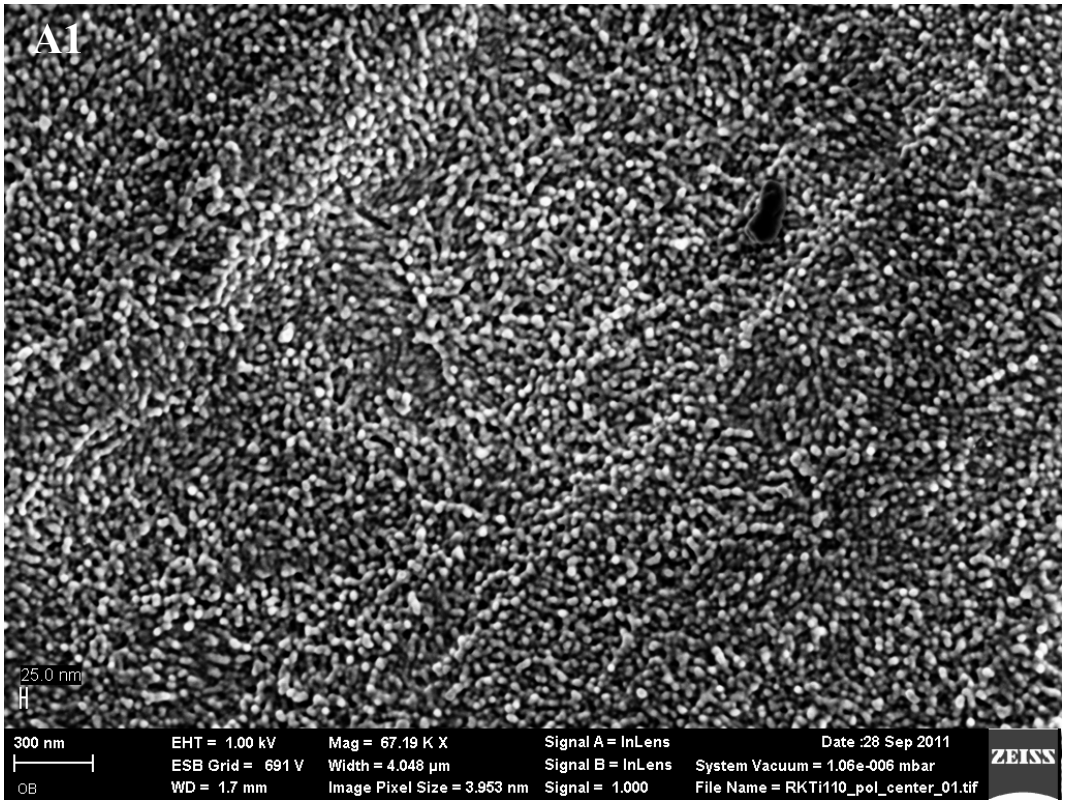
A1
25.0 nm
300 nm
OB
EHT = 1.00 kV
ESB Grid = 691 V
WD = 1.7 mm
Mag = 67.19 K X
Width = 4.048 µm
Image Pixel Size = 3.953 nm
Signal A = InLens
Signal B = InLens
Signal = 1.000
Date :28 Sep 2011
System Vacuum = 1.06e-006 mbar
File Name = RKTi110_pol_center_01.tif
ZEISS

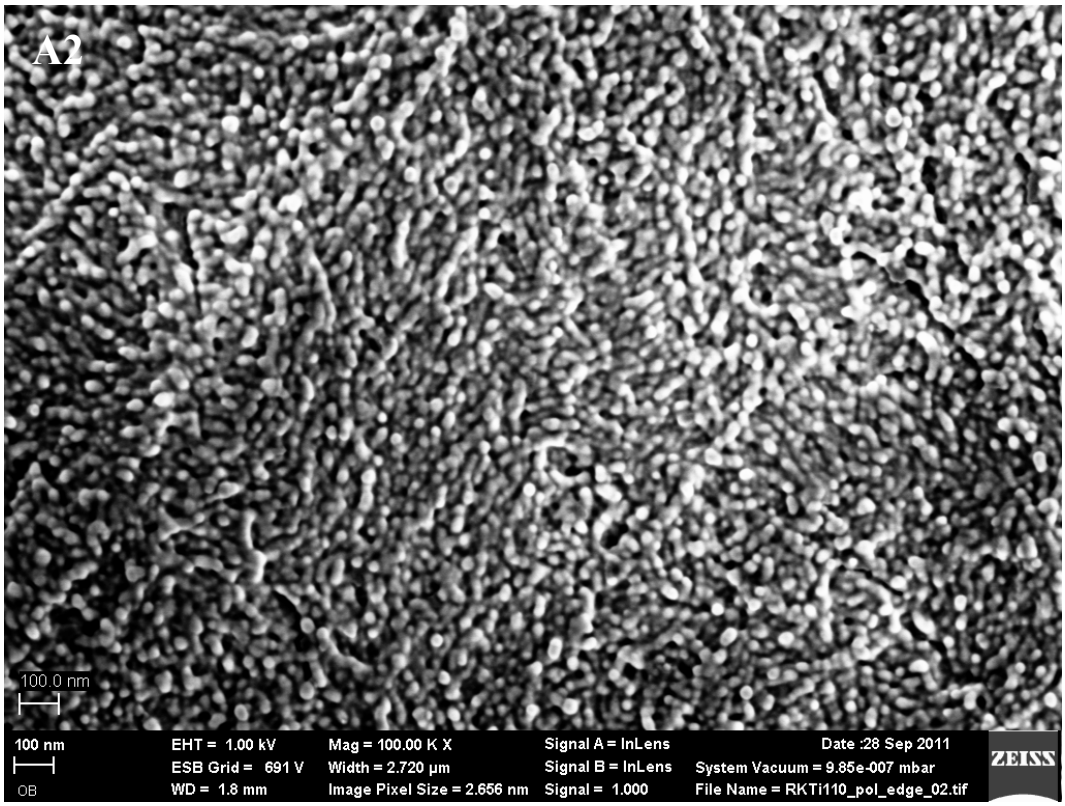
A2
100.0 nm
100 nm
OB
EHT = 1.00 kV
ESB Grid = 691 V
WD = 1.8 mm
Mag = 100.00 K X
Width = 2.720 µm
Image Pixel Size = 2.656 nm
Signal A = InLens
Signal B = InLens
Signal = 1.000
Date :28 Sep 2011
System Vacuum = 9.85e-007 mbar
File Name = RKTi110_pol_edge_02.tif
ZEISS

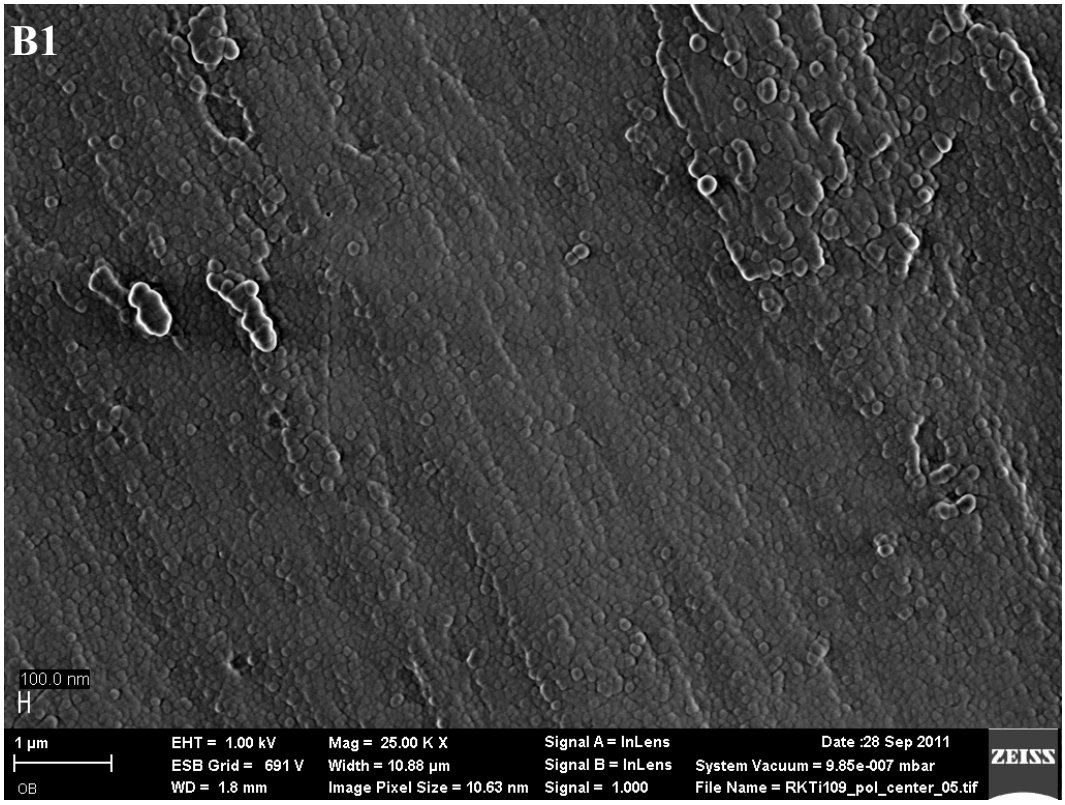
B1
100.0 nm
1 µm
EHT = 1.00 kV
ESB Grid = 691 V
WD = 1.8 mm
Mag = 25.00 K X
Width = 10.88 µm
Image Pixel Size = 10.63 nm
Signal A = InLens
Signal B = InLens
Signal = 1.000
Date :28 Sep 2011
System Vacuum = 9.85e-007 mbar
File Name = RKTi109_pol_center_05.tif
ZEISS

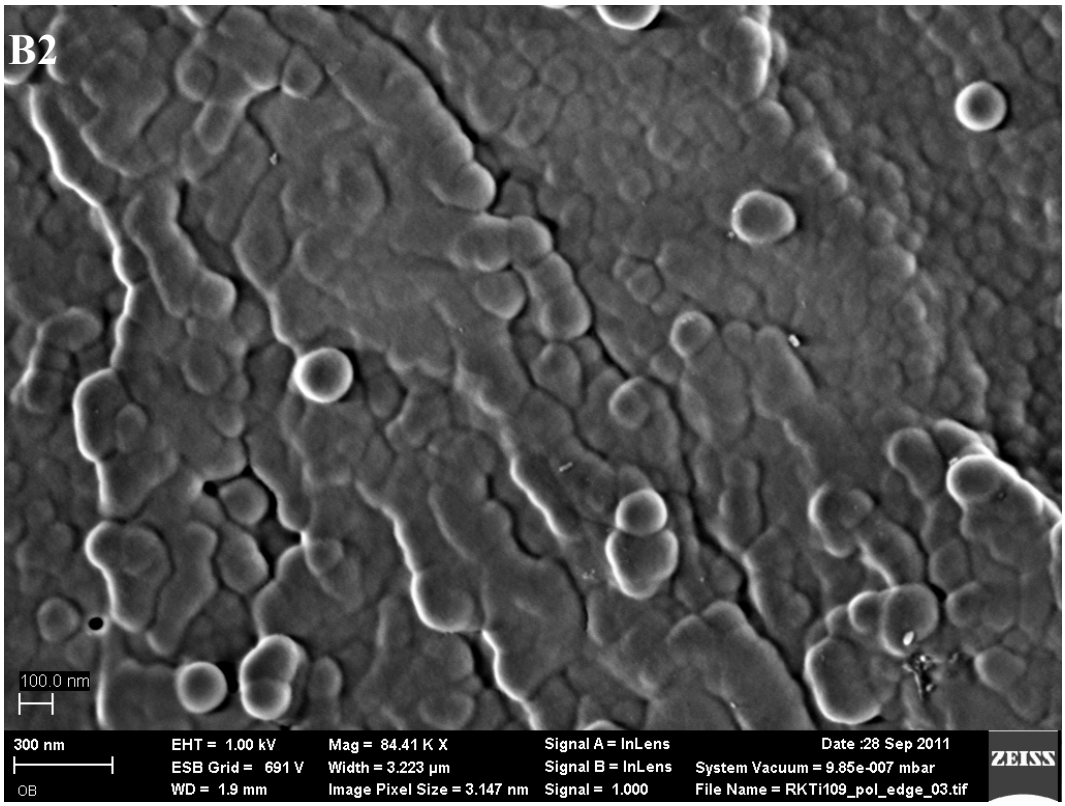
B2
100.0 nm
300 nm
EHT = 1.00 kV
ESB Grid = 691 V
WD = 1.9 mm
Mag = 84.41 K X
Width = 3.223 µm
Image Pixel Size = 3.147 nm
Signal A = InLens
Signal B = InLens
Signal = 1.000
Date :28 Sep 2011
System Vacuum = 9.85e-007 mbar
File Name = RKTi109_pol_edge_03.tif
ZEISS

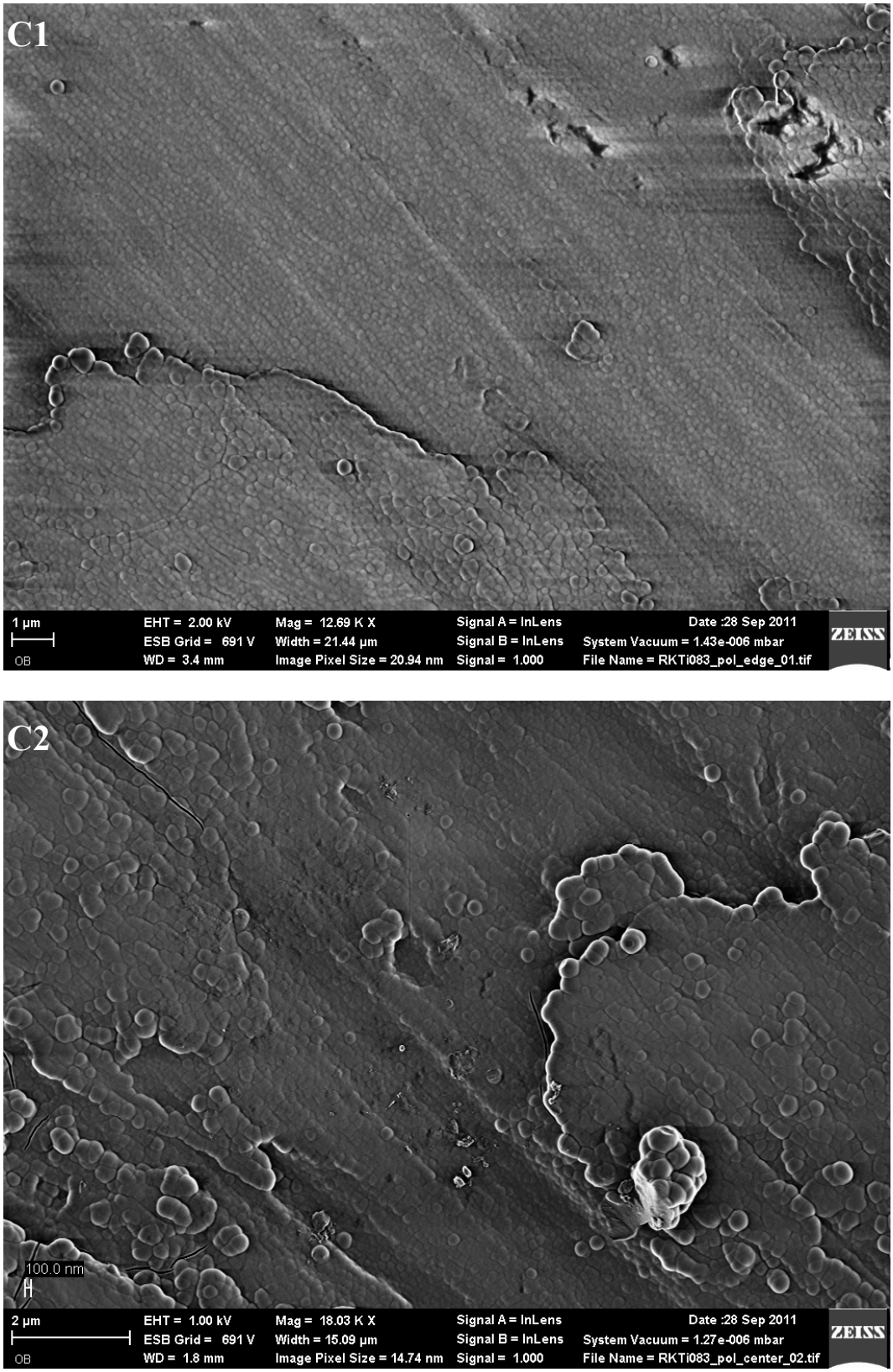

Figure 2. 16 High (A1,B1,C1) and low (A2,B2,C2) magnification FE-SEM images of the samples Act1 (A), Act2 (B) and Act3 (C)

These results indicate that at the starting time of the deposition, small silica particles stick onto the titanium. The silica particles continue to grow in the solution and simultaneously deposit onto the surface. Therefore, the coating is composed of layers of silica particles with different particle sizes. As the number of the layers of the silica particles increase, the particles size increases. In addition to this, the deposited silica would act as a seed for the growth of the film and contribute to the growth. Even though the thicknesses of the films increase in time, the particle size reached at the end of the reaction duration is much larger. Therefore, the particles formed in the solution towards the end can not be deposited homogeneously. In Figure 2.17 FE-SEM image of the sample Act3 is given. Nearly micron size aggregates composed of larger particles randomly deposited on to the substrate can be seen in low magnification FE-SEM images.

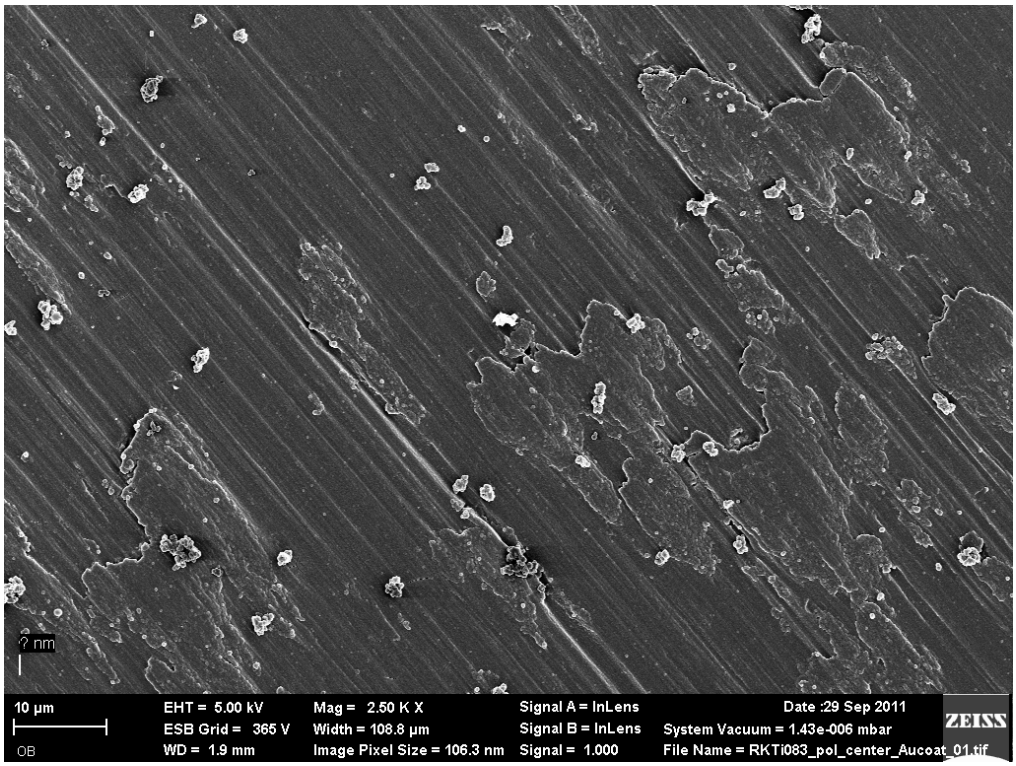

Figure 2. 17 Low magnification FE-SEM images of the sample Act3

The amplitude of the ultrasonic source determines the ultrasonic intensity applied to the system. The increase of the ultrasonic amplitude increases the ultrasonic activity and the cavitation formation. Depending on the conditions, a critical intensity is required to break the intermolecular forces of the liquid and form cavitation. The sound intensity is proportional to the square of the amplitude of the sound wave. The increase of the intensity increases the pressure difference between the expansion and compression cycle. Pressure difference determines the velocity and acceleration of the particles under ultrasonic field. Previous research on the deposition of different nanoparticles onto different substrates is purely based on the ultrasonic activity since there is no chemical interaction between the substrate and the deposited particles [129, 130]. Among the published papers only deposition onto steel is reported as a hard substrate. The adhesion problem of the nanoparticles is reported on hard substrates since the collision velocity of the nanoparticles onto the substrate is not fast enough to adhere to the surface strongly [131]. To overcome this problem, a chemical interaction between the substrate and the deposited particles are created. Since there is a chemical interaction between the substrate and the deposited particles, the amplitude of the sound wave is varied in order to see the effect of the intensity of the ultrasonic field to the deposition process (Samples Act3, Act7, and Act8). The reflectance spectra and corresponding silica and titania thicknesses for these films are given Figure 2.18 and Table 2.5 respectively.

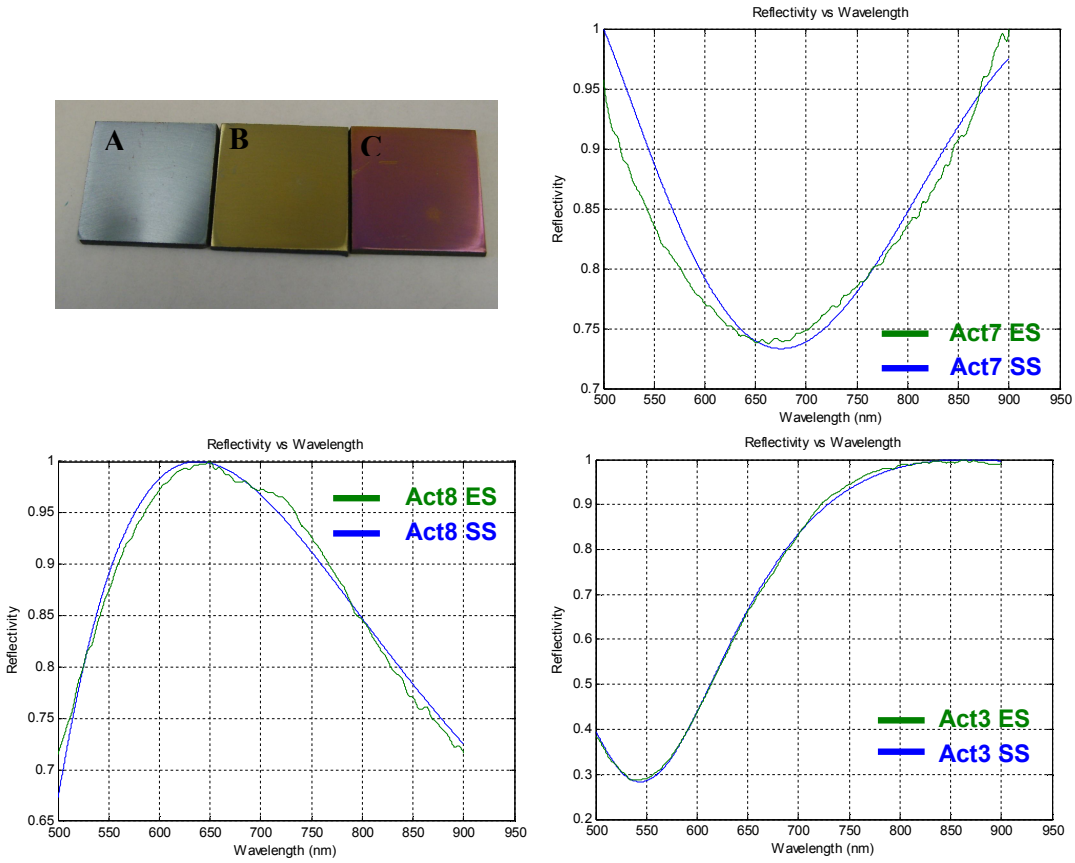

Figure 2. 18 Photo (A: Act7 B: Act8, C: Act3) and reflectance simulations of the samples Ac7 Act 8 and Act 3. (ES: Experimental spectrum, SS: Simulated spectrum)

The thicknesses of the silica film are increasing with the increase of the amplitude of the sound wave. The color of the samples also indicates the thickness difference between the samples. Even though the particles have a chemical interaction with the piranha treated surface, the acceleration under intensity of the ultrasonic field determines the final thickness of the silica films. Therefore, in addition to the chemical interaction between the particles and the substrate the intensity of the ultrasonic field plays an important role during the deposition. The particles are accelerated to the substrates under ultrasonic field and collide with the substrate. The pressure amplitude for 50 W cm^{-2} intensity ultrasonic field in acetone is calculated as 9.25 atm (Equation 2.1). The pressure amplitude for the same energy of ultrasound in water is 12.25 atm. Therefore,

the acceleration due to ultrasonic field is higher in water compared to acetone. However, the cavitation formation is expected to be higher in acetone due to low surface tension, viscosity and boiling point of acetone. Therefore cavitation collapse plays an important role in the deposition process. The deposition process is mostly determined by the collapse of the cavitation at the neighborhood of the solid boundary. This collapse leads to formation of microjets which throws the formed silica particles on to the titanium surface [140]. It is important to specify here that the ACT3 is not a fully reproducible coating since the reaction conditions are extreme (Out of 6 experiments 3 of them has pink color, 2 of them has yellow color). Further increase of water or ammonia amount results in aggregation which blocks the further growth of the film.

2.13 Deposition of organically modified silica particles

Incorporation of organic molecules into the coatings is mostly used to reduce the stress during the annealing process within the matrix by reducing the crosslinking [107]. The utilization of organosilanes in this study has a different purpose. Organosilanes are used in this study to solve our primary problem, aggregation. Aggregation under ultrasonic field is inevitable. Since the aggregation is accelerated by the chemical interaction between the particles, an organic group that has weak interaction with the particles can decrease the rate of aggregation. Reactions performed by using TEOS and DTES as precursors are given in table 2.6. In all of the reactions ammonia and acetone is used as the catalyst and solvent, respectively.

Table 2. 6 Reaction parametrs for the deposition of organically modified silica particles

	Temp. (°C)	Amplitude	Duration (Min)	Mole Percent(TEOS-DTES)	Catalyst Amount(ml)	Extra Water amount	TEOS Amount (ml)	TiO_2 Thickness (nm)	SiO_2 Thickness (nm)
Comp1	25	70%	120	95-5	2	2	2	16	184
Comp2	25	70%	120	95-5	3	2	2	9	228
Comp3	25	70%	120	95-5	3	-	2	15	150
Comp4	25	70%	120	95-5	4	-	2	10	254
Comp5	25	70%	120	95-5	5	-	2	12	204
Comp6	25	70%	120	90-10	3	-	2	12	166
Comp7	25	70%	120	85-15	3	-	2	-	-

Substitution of alkoxy groups in silicate precursors with alkyl chain affects the kinetics of the reaction by inductive effects. The electron donating ability of the alkyl groups increases the electron density on silicon and decreases the hydrolysis rate in basic conditions. Since the hydrolysis rate is rate the determining step in low concentration of water, the reactions proceed slower. However, the ammonia and water concentrations can be increased when an organosilane is introduced in to the reaction solution. Even though the ammonia and water concentrations are increased, none of the reactions in the table end up with aggregates on titanium that blocks the further growth of the film. In reaction conditions of Comp3, silica particles aggregate quickly (sample Act6). Even though the reaction proceeds slower in composite system (under same ammonia and water concentration), further increase of ammonia (samples Comp4, Comp5) concentration do not cause a dramatic increase in aggregation rate. The thickness and the color of the sample are similar with the thickest coating obtained by the acetone. The FE-SEM images of the sample Comp4 (Figure 2.19) show that the deposited particles are larger (around 200 nm) compared to the pure silica sample (Act3). Therefore, by introducing an organosilane to the reaction, it is possible to decrease the aggregation rate and deposit larger particles.

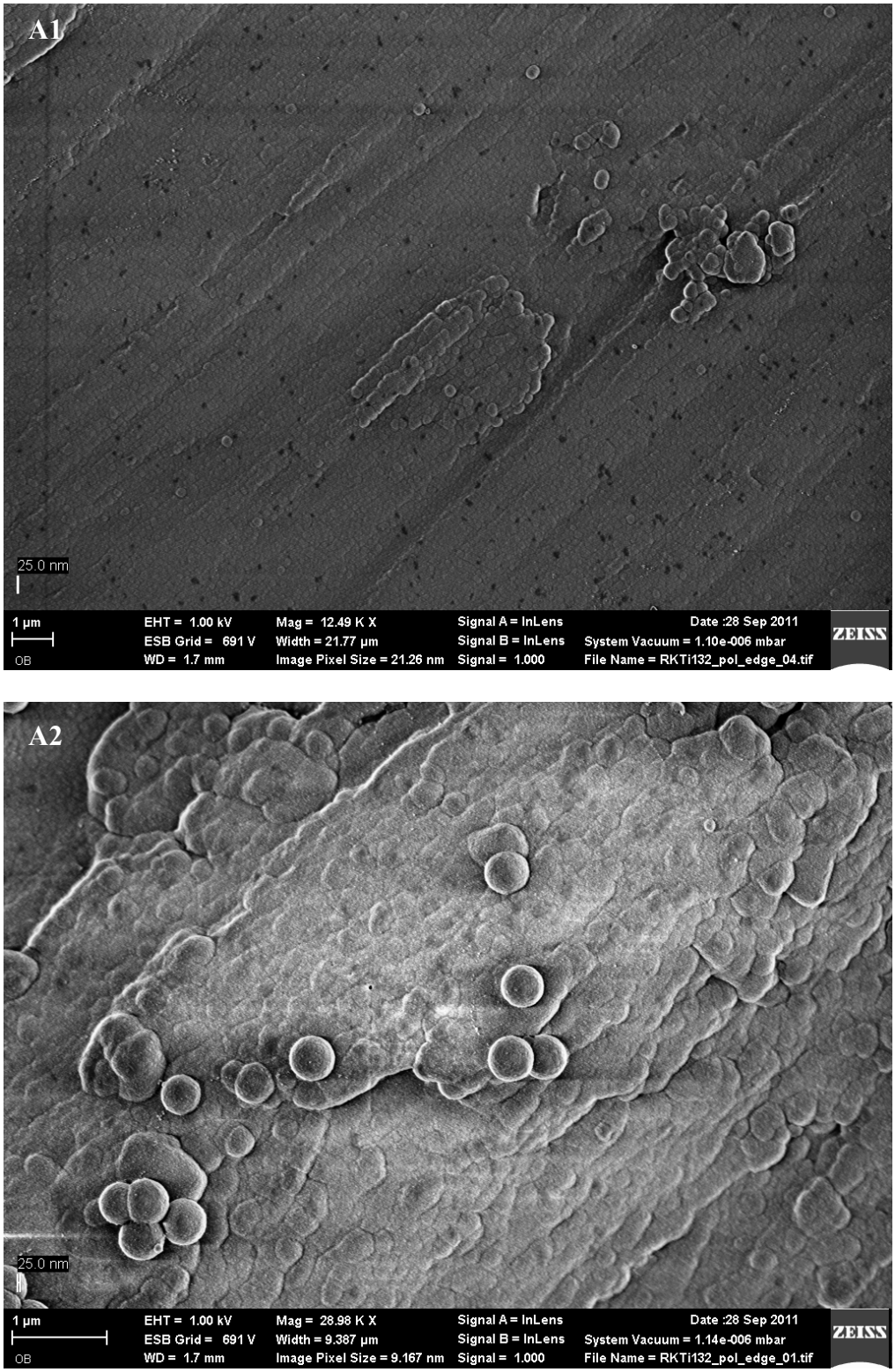

Figure 2. 19 Low (A1) and High (A2) magnification FE-SEM images of the sample Comp4.

Since the thickness of the sample Act3 and sample Comp4 is nearly same, it can be concluded that the composite film is composed of layers of larger particles compare to the silica film. The increase of viscosity limits the deposition process. This is also clear when the ammonia concentration is increased further (Comp5). The thickness of the film decreases although the ammonia amount in the reaction is increased. Increase in particle size increases the viscosity so much that the particles can not be deposited. The FE-SEM images of sample Comp2 (Figure 2.20) also shows rarely deposited aggregated large particles on titanium surface. These results show that viscosity of the solution plays an important role on deposition process and the addition of 5% percent organosilane can not deplete the aggregation totally.

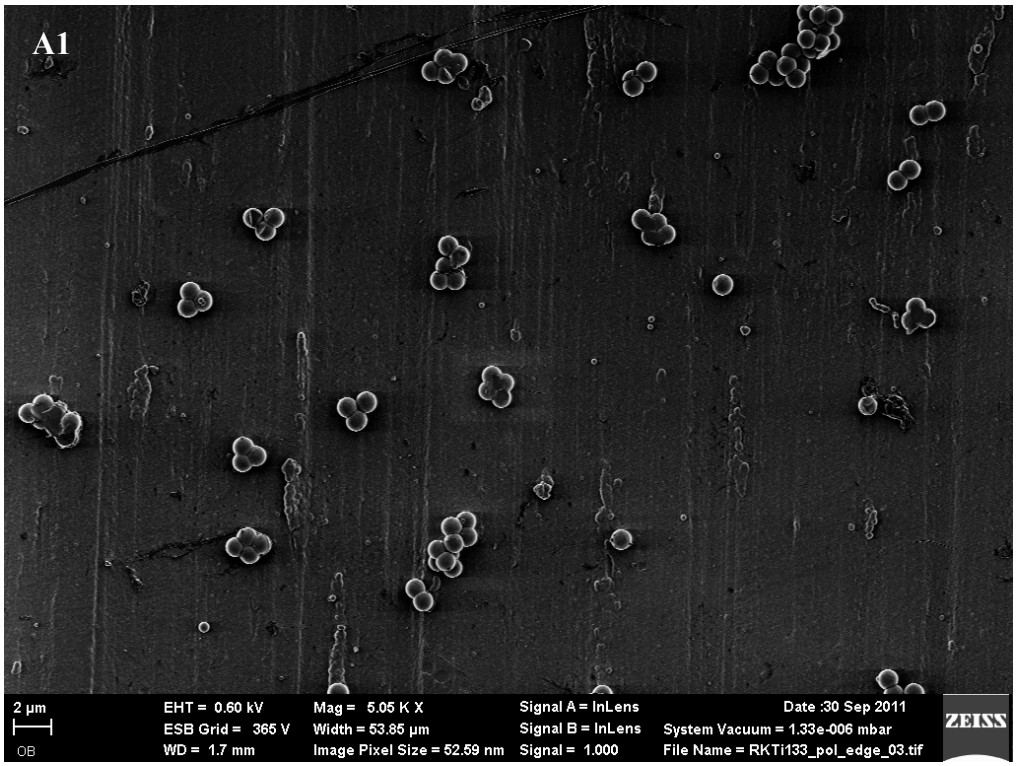

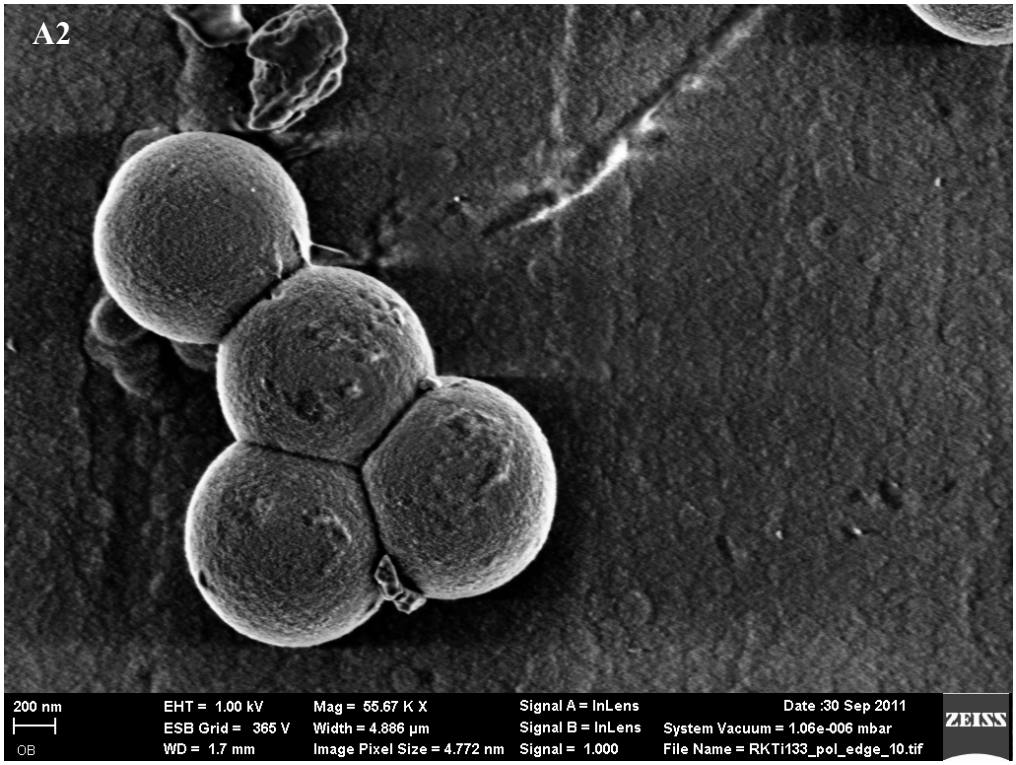

Figure 2. 20 Low (A1) and high (A2) magnification FE-SEM images of the sample Comp2

The morphology of silica particles as well as the size of the particles can also be affected by the addition of the organosilane into the system. Depending on addition time of organosilanes, amount of organosilanes in the system the morphology of the system changes from spherical to lamellar structure [141, 142]. In Figure 2.21, FE-SEM images of the films prepared by different TEOS/DTES ratios are given. With the increasing amount of organosilane ratio in the system, the spherical morphology reduces. The films are no more composed of fused individual spherical particles, instead they form an integrated structure that is not composed of individual defined morphologies. The thicknesses of the samples calculated from the simulation of reflectance spectra are given in Table 2.6. Even though the available sites for the chemical interaction is reduced, the thicknesses of the films seems to be unaffected by the increasing organosilane ratio in the reaction solution. Further increase of organosilane amount may

also influence the thicknesses of the films. Using organosilane increases the reproducibility of the reaction. However, one must be careful during the addition of DTES since it has high viscosity.

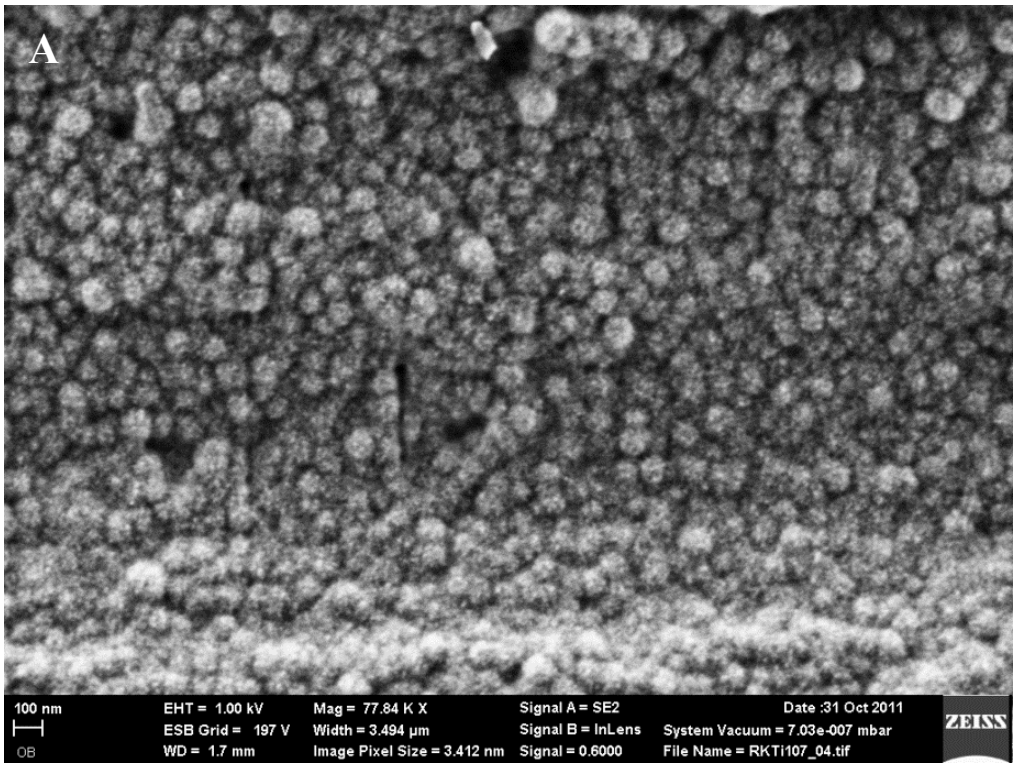

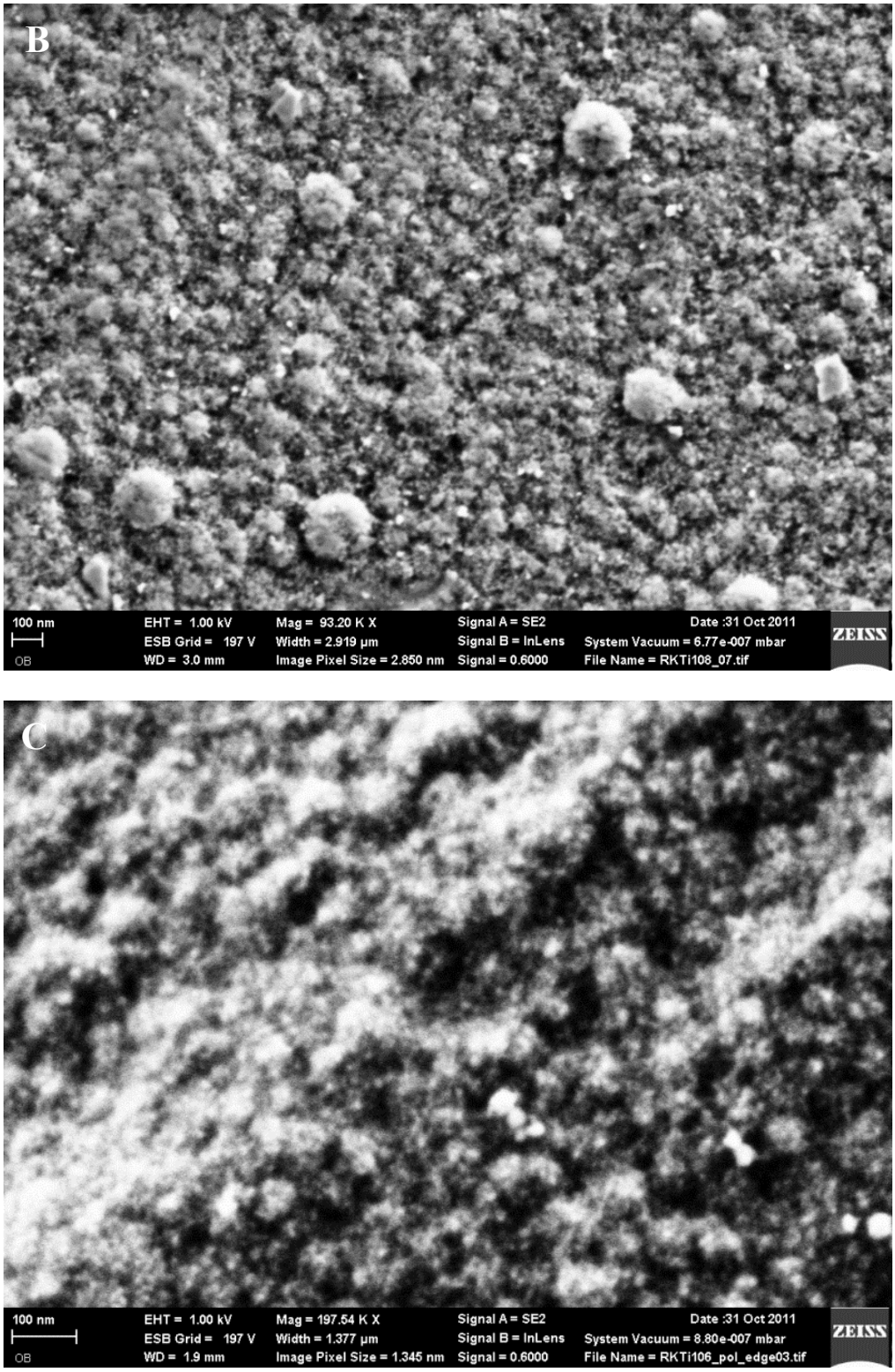

Figure 2. 21 FE-SEM images of the samples prepared with different TEOS/DTES mol ratio (A:Comp5, B:Comp6, C: Comp7)

2.14 Electrochemical characterization

The sol-gel coatings are usually annealed to enhance the stability of the films. The produced films with ultrasound are stable in electrolyte solutions without annealing. In addition to this, there is no report in the literature on sol-gel coatings prepared with ultrasound. Therefore, the electrochemical characterization is also done without applying any heat treatment. In Figure 2.22 and 2.23, OCP and CV measurements of the piranha treated, polished samples in addition to the coated samples Act1, Act2, Act3 are given. OCP measurements of the samples are monitored before the polarization measurements for 30 minutes to reach a quasi-equilibrium state and to detect the changes at the electrode/solution interface. The change in OCP values of the sample could indicate the change at the surface. Substrates with positive OCP values are called noble materials. After the immersion of the sample in to the electrolyte solution the OCP value may drift depending on the changes in the interface. The change in positive direction is related to the formation or thickening of the oxide layer. The change in negative direction is interpreted as release of metal ions into the solution.

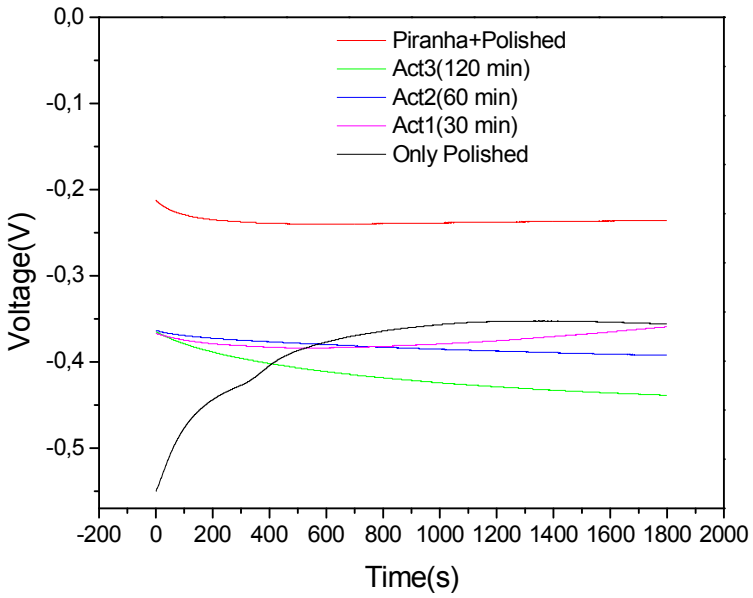

Figure 2. 22 OCP of the samples prepared as a function of time

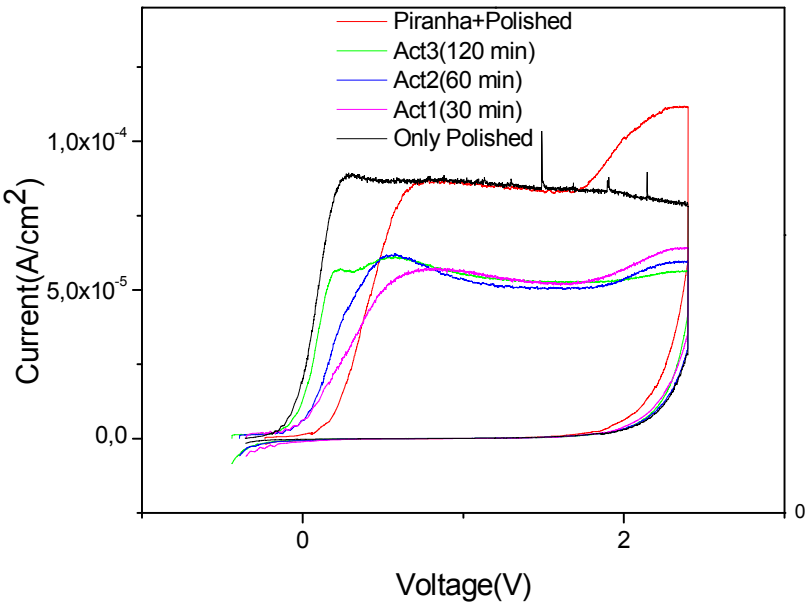

Figure 2. 23 CV of the samples prepared as function of time

The polished bare titanium has the most negative OCP value at the starting point. In time, titania layer is formed in the electrolyte solution and the OCP values move towards noble direction. The piranha treated sample already has a thin titania layer on the surface and has the most noble OCP value among all of the samples. The OCP values of all coated samples start around -0.360 V and they change only ±40 mV during 30 minutes exposure time. OCP of the fully coated samples (Act2, Act3) slightly moves toward the negative direction whereas the OCP of the partially coated sample (Act1) slowly increases in the positive direction. The slight changes of the OCP values indicate the stability of the coatings.

The cyclic voltammetry measurements are started from the final OCP values after 30 min. Polarization in the positive potential results in corrosion in all samples. The corrosion rate can be calculated by Tafel extrapolation when the process is charge transfer controlled. In case of charge transfer controlled process the semi-logarithmic plot of the current-potential graph gives a linear region in both cathodic and anodic direction slightly above the OCP value. However the existence of the oxide layer SiO_2

coated samples case lead to diffusion controlled process and the curve flattens out. At a certain potential, increase of the potential does not increase the current density. This potential is called passivation potential and the low current density at this potential indicates the corrosion resistance of the substrate. A passive film is formed at the surface of substrate that prevents the metal from further corrosion. The metal then passes through a passive region where the current density does not change with the increase of the potential. This current is known as passive current density. The OCP values after 30 minutes, passivation potentials, current densities at passivation potentials are given in Table 2.6.

Table 2. 7 OCP, passivation potential, passivation current density, passive current density of the samples

	Open circuit potential(mV)	Passivation potential (mV)	Passivation current density($\mu A/cm^2$)	Passive current density($\mu A/cm^2$)
Only Pol.	-356	286	88.0	86.0
Piran. Tre.	-236	745	86.0	86.0
Act1	-356	560	56.4	56.2
Act2	-392	561	61.9	52.4
Act3	-439	747	56.8	56.1
Comp2	-431	628	60.4	58.5
Comp4	-457	617	55.1	52.1

The passivation current densities of the coated sample are 2/3 of the bare sample. This indicates that the coated samples by using sonochemical methods improve the resistance against corrosion. The active and passive behaviors of the samples are similar. When the potential is further increased, the different behaviors are observed between bare titanium and other samples. After the passive region, there is an increase in the current density in piranha treated and coated samples. This behavior in the literature is explained with the difference in conductivity and porosity of the oxide layer. The oxide layer conductivity and porosity on piranha treated and coated samples may be higher

than the anodically formed oxide layer in bare titanium during polarization [143]. If the current density increases as a result of local breakdown of the film, the reverse scan current densities would be higher than the forward scan current densities. All the coatings are stable and there is no sign of a local breakdown in the coatings. The OCP of the composite coatings are slightly negative compare to pure silica and cyclic voltammetry behaviors are very similar since the reactant solutions contain only 5% of organosilane (not given here).

CONCLUSIONS

Primary focus of this study is to produce films that would increase the corrosion resistance of titanium by using the power of ultrasound. For this purpose, different reaction conditions and different solvents are used to find the optimum coating conditions. Acetone with lower viscosity and low boiling point is found to be best solvent for the deposition process. In each solvent, the deposition processes continue until critical size is reached and then the deposition rate decreases dramatically. By varying parameters such as reaction time, amplitude of the sound wave, the thicknesses of the coating are controlled. The thicknesses of the coating are determined by using a reflectance simulation program. In addition to control of the film thickness, the deposited particle sizes are changed by changing the solvent or adding an organosilane to the reaction mixture. The corrosion behavior of the bare and coated titanium is analyzed by OCP measurements and CV. Even without annealing, the coatings are proved to be a better barrier to corrosion compared to natural oxide layer on bare titanium.

APPENDIX

Simulation Program

The Matlab program is composed of a script and a function. In the script, the theoretical reflectance is simulated and compared with the experimental spectrum. The program is fed with possible minimum and maximum thicknesses of the silica and titania layers in addition to the incident angle and refractive index of the incident medium. The indices of refraction for silica and titania layers are calculated using Sellmeier equations using literature data. By using the function, the program first calculates the incidence angles for each layer by using Snell's law. Then, in the function, the theoretical reflectance spectrum is simulated by using the equations given in introduction part [144]. For each titania and silica thicknesses, the difference between theoretical spectra and experimental spectra is calculated. The script minimizes the difference between the theoretical and experimental spectra by using this function and reports the corresponding titania and silica thicknesses in the command window.

Script

```
clear all
close all
clc


d1min= input('Enter the min bound thickness of the first layer (nm):
');
d1max= input('Enter the max bound thickness of the first layer (nm):
');
```

```
d2min= input('Enter the min bound thickness of the second layer (nm):
');
d2max= input('Enter the max bound thickness of the second layer (nm):
');


d1i=mean([d1min d1max]);
d2i=mean([d2min d2max]);


%d_layer2 = input('Enter the thickness of the second layer (nm): ');
Incident_Index = input('Enter the index of the incident medium = ');
theta_incident1 = input('Enter the incident angle (in degree) = ');


warning off
fmincon(@(x)
reflectivity_funwithoxidenorm12(x,Incident_Index,theta_incident1),[d1i
d2i],[],[],[],[],[d1min d2min],[d1max d2max])
```

Function

```
Function
err=reflectivity_funwithoxidenorm12(d_layer,Incident_Index,theta_incid
ent1)
exp_data=load(NAME.txt');
maxexp=max(exp_data(:,2));
exp_reflec=exp_data(:,2)/(maxexp);
lambda_all=exp_data(:,1)*1e-9;


d_layer1=d_layer(1);
d_layer2=d_layer(2);
```

```
% Converting input wavelength to nm
d_layer2 = d_layer2*1E-9;
d_layer1 = d_layer1*1E-9;
x = 1;
y = 1;
Reflectivity = [];
Wavelength = [];
for lambda = lambda_all'
Index_1    =    3.84289E+24*lambda^4    -    8.89053E+18*lambda^3    +
7.63319E+12*lambda^2 - 2.92418E+06*lambda + 1.88774E+00;
Index_2=     7.79631E+23*lambda^4     -     2.48333E+18*lambda^3     +
3.00772E+12*lambda^2 - 1.66202E+06*lambda + 2.84520E+00;
Substrate_Index   =   1.34601E+38*lambda^6   -   5.77644E+32*lambda^5   +
9.85540E+26*lambda^4  -  8.55160E+20*lambda^3  +  3.98215E+14*lambda^2  -
9.12645E+07*lambda   +   9.11703E+00   -   i*(   6.92246E+37*lambda^6   -
2.88996E+32*lambda^5  +  4.81931E+26*lambda^4  -  4.07524E+20*lambda^3  +
1.78471E+14*lambda^2 - 3.28383E+07*lambda + 3.09298E+00) ;
% After converting the angle to radians, the incident angle at each
interface can be calculated by
% utilising Snells Law, that is, n1sin(theta1) = n2sin(theta2)
theta_incident = theta_incident1*pi/180;
theta_1 = asin(Incident_Index/Index_1*sin(theta_incident));
theta_2 = asin(Index_1/Index_2*sin(theta_1));
theta_s = asin(Index_2/Substrate_Index*sin(theta_2));
% working out the optical admittances of the layers
Y = 2.6544*1E-3;
admittance_layer1 = Index_1*cos(theta_1)*Y;
admittance_incident = Incident_Index*cos(theta_incident)*Y;
```

```
admittance_layer2 = Index_2*cos(theta_2)*Y;
admittance_substrate = Substrate_Index*cos(theta_s)*Y;
% Caluculating the phase factor "del" for the layers.
del1 = (2*pi*Index_1*d_layer1*cos(theta_1)) / lambda;
del2 = (2*pi*Index_2*d_layer2*cos(theta_2)) / lambda;
% Calculating the characteristic matrix (B C) for layer_1
b1 = [cos(del1), (sin(del1)/admittance_layer1)*i];
c1 = [(admittance_layer1*sin(del1))*i, cos(del1)];
M1 = [b1; c1];
% Calculating the characteristic matrix (B C) for layer_2
b2 = [cos(del2), (sin(del2)/admittance_layer2)*i];
c2 = [(admittance_layer2*sin(del2))*i, cos(del2)];
M2 = [b2; c2];
M = M1*M2;
% Calculating the reflectance
c = M(2,1) + M(2,2)*admittance_substrate;
c_conj = conj(c);
b = M(1,1) + M(1,2)*admittance_substrate;
b_conj = conj(b);
Reflectance_numerator = admittance_incident*b - c;
Reflectance_denominator = admittance_incident*b + c;
r1 = Reflectance_numerator/Reflectance_denominator;
r2= conj(r1);
Reflectance = r1*r2;
Lambda = lambda*1E9;
%fprintf('%f, %f, %f\n', Reflectance, Lambda, Phase)
Reflectivity(x) = Reflectance;
x=x+1;
Wavelength(y) = Lambda;
```

```
y=y+1;
end
maxref=max(Reflectivity);
Reflectivity=Reflectivity/maxref;
cla;
plot(Wavelength, Reflectivity,Wavelength, exp_reflec);
title('Reflectivity vs Wavelength');
xlabel('Wavelength (nm)');
ylabel('Reflectivity');
Output(:,1) = Wavelength;
Output(:,2) = Reflectivity;
dlmwrite('Fit1.txt',Output,'\t')
hold on;
grid on;
drawnow
err=norm(Reflectivity-exp_reflec')
```

BIBLIOGRAPHY

1. Mason, T.J. and J.P. Lorimer, *Sonochemistry: theory, applications and uses of ultrasound in chemistry*1988: Ellis Horwood.
2. Suslick, K.S., D.A. Hammerton, and R.E. Cline, *Sonochemical hot spot.* Journal of the American Chemical Society, 1986. **108**(18): p. 5641-5642.
3. Flint, E.B. and K.S. Suslick, *The temperature of cavitation.* Science, 1991. **253**(5026): p. 1397-9.
4. Suslick, K.S., S.J. Doktycz, and E.B. Flint, *On the origin of sonoluminescence and sonochemistry.* Ultrasonics, 1990. **28**(5): p. 280-290.
5. Makino, K., M.M. Mossoba, and P. Riesz, *Chemical effects of ultrasound on aqueous solutions. Formation of hydroxyl radicals and hydrogen atoms.* The Journal of Physical Chemistry, 1983. **87**(8): p. 1369-1377.
6. Castro, M.D.L. and F.P. Capote, *Analytical applications of ultrasound*2007: Elsevier.
7. Thompson, L.H. and L.K. Doraiswamy, *Sonochemistry: Science and Engineering.* Industrial & Engineering Chemistry Research, 1999. **38**(4): p. 1215-1249.
8. K.S.Suslick, *Sonochemistry.* Review article, 1990.
9. Jin, R., et al., *Photoinduced Conversion of Silver Nanospheres to Nanoprisms.* Science, 2001. **294**(5548): p. 1901-1903.
10. Liu, J., et al., *Self-Assembled CuO Monocrystalline Nanoarchitectures with Controlled Dimensionality and Morphology.* Crystal Growth & Design, 2006. **6**(7): p. 1690-1696.

11. Peng, X., et al., *Shape control of CdSe nanocrystals.* Nature, 2000. **404**(6773): p. 59-61.

12. Jana, N.R., L. Gearheart, and C.J. Murphy, *Wet Chemical Synthesis of High Aspect Ratio Cylindrical Gold Nanorods.* The Journal of Physical Chemistry B, 2001. **105**(19): p. 4065-4067.

13. Singh, D.P., A.K. Ojha, and O.N. Srivastava, *Synthesis of Different Cu(OH)2 and CuO (Nanowires, Rectangles, Seed-, Belt-, and Sheetlike) Nanostructures by Simple Wet Chemical Route.* The Journal of Physical Chemistry C, 2009. **113**(9): p. 3409-3418.

14. Martin, C.R., *Nanomaterials: A Membrane-Based Synthetic Approach.* Science, 1994. **266**(5193): p. 1961-1966.

15. Zhang, G.Q., et al., *Ultrasonic-assisted preparation of monodisperse iron oxide nanoparticles.* Materials Letters, 2007. **61**(11-12): p. 2204-2207.

16. Kumar, R.V., Y. Diamant, and A. Gedanken, *Sonochemical Synthesis and Characterization of Nanometer-Size Transition Metal Oxides from Metal Acetates.* Chemistry of Materials, 2000. **12**(8): p. 2301-2305.

17. Mukaibo, H., et al., *Particle size and performance of SnS2 anodes for rechargeable lithium batteries.* Journal of Power Sources, 2003. **119-121**(0): p. 60-63.

18. Yin, J., et al., *Preparation of ZnS/PS microspheres and ZnS hollow shells.* Materials Letters, 2003. **57**(24-25): p. 3859-3863.

19. Zhang, J., et al., *Sonochemical Formation of Single-Crystalline Gold Nanobelts.* Angewandte Chemie, 2006. **118**(7): p. 1134-1137.

20. Wahab, R., et al., *Room temperature synthesis of needle-shaped ZnO nanorods via sonochemical method.* Applied Surface Science, 2007. **253**(18): p. 7622-7626.

21. Jung, S.-H., et al., *Sonochemical Preparation of Shape-Selective ZnO Nanostructures.* Crystal Growth & Design, 2007. **8**(1): p. 265-269.

22. Woods, T.L. and R.M. Garrels, *Use of oxidized copper minerals as environmental indicators.* Applied Geochemistry. **1**(2): p. 181-187.

23. Prasad, S.V.S. and V. Sitakara Rao, *Thermal analysis, X-ray diffraction and infrared spectroscopic study of synthetic brochantite.* Journal of Thermal Analysis and Calorimetry, 1985. **30**(3): p. 603-609.

24. Koga, N., J. Criado, and H. Tanaka, *Reaction pathway and kinetics of the thermal decomposition of synthetic brochantite.* Journal of Thermal Analysis and Calorimetry, 1997. **49**(3): p. 1467-1475.

25. Vilminot, S., et al., *Nuclear and magnetic structures and magnetic properties of synthetic brochantite, Cu4(OH)6SO4.* Dalton Transactions, 2006(11): p. 1455-1462.

26. Vilminot, S., et al., *Synthesis, structure and magnetic properties of copper hydroxysulfates.* Crystal Engineering. **5**(3-4): p. 177-186.

27. Koga, N., et al., *Thermal decomposition of synthetic antlerite prepared by microwave-assisted hydrothermal method.* Thermochimica Acta, 2008. **467**(1-2): p. 11-19.

28. Matijević, S.K.a.E., *Preparation of copper compounds of different compositions and particle morphologies.* Journal of Materials Research, (1991). **6**: p. 766-777.

29. Bakhtiari, F. and E. Darezereshki, *One-step synthesis of tenorite (CuO) nano-particles from Cu4 (SO4) (OH) 6 by direct thermal-decomposition method.* Materials Letters, 2011. **65**(2): p. 171-174.

30. Borkow, G. and J. Gabbay, *Copper as a Biocidal Tool.* Current Medicinal Chemistry, 2005. **12**(18): p. 2163-2175.

31. Dollwet, H.H.A.S., J R J, *Historic Uses of Copper Compounds in Medicine.* Trace Elements in Medicine, 1985. **2**(2): p. 80-87.

32. Borkow, G. and J. Gabbay, *Copper, An Ancient Remedy Returning to Fight Microbial, Fungal and Viral Infections.* Current Chemical Biology, 2009. **3**(3): p. 272-278.

33. Courtade, M.R., Georges, *Bordeaux mixture, process for its manufacture and cupric fungicidal compositions containing it* U.S. Patent 5958,438, 1996.

34. Frederic Ferrier, G.J., Marc Pillot, *Method of producing copper hydoroxosulphates and copper fungicidal compositions containing same* US Patent US2007/0003635 A1, 2007.

35. Pal, S., Y.K. Tak, and J.M. Song, *Does the Antibacterial Activity of Silver Nanoparticles Depend on the Shape of the Nanoparticle? A Study of the Gram-Negative Bacterium Escherichia coli.* Applied and Environmental Microbiology, 2007. **73**(6): p. 1712-1720.

36. Pang, H., F. Gao, and Q. Lu, *Morphology effect on antibacterial activity of cuprous oxide.* Chemical Communications, 2009(9): p. 1076-1078.

37. Nowack, B. and T.D. Bucheli, *Occurrence, behavior and effects of nanoparticles in the environment.* Environmental Pollution, 2007. **150**(1): p. 5-22.

38. Matthews, R.W., *The Radiation Chemistry of the Terephthalate Dosimeter.* Radiation Research, 1980. **83**(1): p. 27-41.

39. Fang, X., G. Mark, and C. von Sonntag, *OH radical formation by ultrasound in aqueous solutions Part I: the chemistry underlying the terephthalate dosimeter.* Ultrasonics Sonochemistry, 1996. **3**(1): p. 57-63.

40. Mason, T.J., et al., *Dosimetry in sonochemistry: the use of aqueous terephthalate ion as a fluorescence monitor.* Ultrasonics Sonochemistry, 1994. **1**(2): p. S91-S95.

41. Saran, M. and K.H. Summer, *Assaying for hydroxyl radicals: Hydroxylated terephthalate is a superior fluorescence marker than hydroxylated benzoate.* Free Radical Research, 1999. **31**(5): p. 429-436.

42. Penn, R.L. and J.F. Banfield, *Imperfect Oriented Attachment: Dislocation Generation in Defect-Free Nanocrystals.* Science, 1998. **281**(5379): p. 969-971.

43. Lu, C., et al., *Simple Template-Free Solution Route for the Controlled Synthesis of Cu(OH)2 and CuO Nanostructures.* The Journal of Physical Chemistry B, 2004. **108**(46): p. 17825-17831.

44. Rasmussen, J.K., et al., *Kinetics and mechanism of the interaction of potassium peroxydisulfate and 18-crown-6 in aqueous media.* Journal of the American Chemical Society, 1983. **105**(23): p. 6845-6849.

45. Price, G.J. and A.A. Clifton, *Sonochemical acceleration of persulfate decomposition.* Polymer, 1996. **37**(17): p. 3971-3973.

46. Liang, C. and H.-W. Su, *Identification of Sulfate and Hydroxyl Radicals in Thermally Activated Persulfate.* Industrial & Engineering Chemistry Research, 2009. **48**(11): p. 5558-5562.

47. Hayon, E., A. Treinin, and J. Wilf, *Electronic spectra, photochemistry, and autoxidation mechanism of the sulfite-bisulfite-pyrosulfite systems. SO2-, SO3-, SO4-, and SO5- radicals.* Journal of the American Chemical Society, 1972. **94**(1): p. 47-57.

48. Pennington, D.E. and A. Haim, *Stoichiometry and mechanism of the chromium(II)-peroxydisulfate reaction.* Journal of the American Chemical Society, 1968. **90**(14): p. 3700-3704.

49. Fischer, C.H., E.J. Hart, and A. Henglein, *Ultrasonic irradiation of water in the presence of oxygen 18,18O2: isotope exchange and isotopic distribution of hydrogen peroxide.* The Journal of Physical Chemistry, 1986. **90**(9): p. 1954-1956.

50. Parke, A.V.M. and D. Taylor, *855. The chemical action of ultrasonic waves.* Journal of the Chemical Society (Resumed), 1956: p. 4442-4450.

51. Petrier, C., et al., *Sonochemical Degradation of Phenol in Dilute Aqueous Solutions: Comparison of the Reaction Rates at 20 and 487 kHz.* The Journal of Physical Chemistry, 1994. **98**(41): p. 10514-10520.

52. Mark, G., et al., *OH-radical formation by ultrasound in aqueous solution – Part II: Terephthalate and Fricke dosimetry and the influence of various conditions on the sonolytic yield.* Ultrasonics Sonochemistry, 1998. **5**(2): p. 41-52.

53. Weissler, A., *Formation of Hydrogen Peroxide by Ultrasonic Waves: Free Radicals.* Journal of the American Chemical Society, 1959. **81**(5): p. 1077-1081.

54. Hua, I. and M.R. Hoffmann, *Optimization of Ultrasonic Irradiation as an Advanced Oxidation Technology.* Environmental Science & Technology, 1997. **31**(8): p. 2237-2243.

55. Rack, H.J. and J.I. Qazi, *Titanium alloys for biomedical applications.* Materials Science and Engineering: C, 2006. **26**(8): p. 1269-1277.

56. R.R, B., *An overview on the use of titanium in the aerospace industry.* Materials Science and Engineering: A, 1996. **213**(1-2): p. 103-114.

57. Faller, K. and F. Froes, *The use of titanium in family automobiles: Current trends.* JOM Journal of the Minerals, Metals and Materials Society, 2001. **53**(4): p. 27-28.

58. González, J.E.G. and J.C. Mirza-Rosca, *Study of the corrosion behavior of titanium and some of its alloys for biomedical and dental implant applications.* Journal of Electroanalytical Chemistry, 1999. **471**(2): p. 109-115.

59. Geetha, M., et al., *Ti based biomaterials, the ultimate choice for orthopaedic implants – A review.* Progress in Materials Science, 2009. **54**(3): p. 397-425.

60. Mccafferty, E., *Introduction to Corrosion Science*2010: Springer.

61. Bockris, J.O.M., R.E. White, and B.E. Conway, *Modern aspects of electrochemistry*1996: Academic Press.

62. T, H., *Metal ion release from metal implants.* Materials Science and Engineering: C, 2004. **24**(6-8): p. 745-752.

63. Mu, Y., et al., *Metal ion release from titanium with active oxygen species generated by rat macrophages in vitro.* Journal of Biomedical Materials Research, 2000. **49**(2): p. 238-243.

64. Martini, D., et al., *Detachment of titanium and fluorohydroxyapatite particles in unloaded endosseous implants.* Biomaterials, 2003. **24**(7): p. 1309-1316.

65. Pimenova, N.V. and T.L. Starr, *Electrochemical and corrosion behavior of Ti–xAl–yFe alloys prepared by direct metal deposition method.* Electrochimica Acta, 2006. **51**(10): p. 2042-2049.

66. Raman, V., S. Tamilselvi, and N. Rajendran, *Electrochemical impedance spectroscopic characterization of titanium during alkali treatment and apatite growth in simulated body fluid.* Electrochimica Acta, 2007. **52**(26): p. 7418-7424.

67. Tamilselvi, S., V. Raman, and N. Rajendran, *Surface modification of titanium by chemical and thermal methods ‐ electrochemical impedance spectroscopic studies.* Corrosion Engineering, Science and Technology, 2011. **46**(4): p. 585-591.

68. Robert, A., *The role of stress-assisted localized corrosion in the development of short fatigue cracks*1997, Philadelphia, PA, ETATS-UNIS: American Society for Testing and Materials. 15.

69. Stansbury, E.E. and R.A. Buchanan, *Fundamentals of electrochemical corrosion*2000: ASM International.

70. Pérez, N., *Electrochemistry and corrosion science*2004: Kluwer Academic.

71. Tsuchiya, H., et al., *Hydroxyapatite growth on anodic TiO2 nanotubes.* Journal of Biomedical Materials Research Part A, 2006. **77A**(3): p. 534-541.

72. Kodama, A., et al., *Bioactivation of titanium surfaces using coatings of TiO2 nanotubes rapidly pre-loaded with synthetic hydroxyapatite.* Acta Biomaterialia, 2009. **5**(6): p. 2322-2330.

73. Demetrescu, I., C. Pirvu, and V. Mitran, *Effect of nano-topographical features of Ti/TiO2 electrode surface on cell response and electrochemical stability in artificial saliva.* Bioelectrochemistry, 2010. **79**(1): p. 122-129.

74. Wen, H.B., et al., *Preparation of bioactive microporous titanium surface by a new two-step chemical treatment.* Journal of Materials Science: Materials in Medicine, 1998. **9**(3): p. 121-128.

75. Gallardo, J., P. Galliano, and A. Durán, *Bioactive and Protective Sol-Gel Coatings on Metals for Orthopaedic Prostheses.* Journal of Sol-Gel Science and Technology, 2001. **21**(1): p. 65-74.

76. Leyens, C. and M. Peters, *Titanium and titanium alloys: fundamentals and applications*2003: Wiley-VCH.

77. Biggs, M.J.P., et al., *The use of nanoscale topography to modulate the dynamics of adhesion formation in primary osteoblasts and ERK/MAPK signalling in STRO-1+ enriched skeletal stem cells.* Biomaterials, 2009. **30**(28): p. 5094-5103.

78. Stevens, M.M. and J.H. George, *Exploring and Engineering the Cell Surface Interface.* Science, 2005. **310**(5751): p. 1135-1138.

79. Cochran, D.L., et al., *Bone response to unloaded and loaded titanium implants with a sandblasted and acid-etched surface: A histometric study in the canine mandible.* Journal of Biomedical Materials Research, 1998. **40**(1): p. 1-11.

80. Wong, M., et al., *Effect of surface topology on the osseointegration of implant materials in trabecular bone.* Journal of Biomedical Materials Research, 1995. **29**(12): p. 1567-1575.

81. Brunette, D.M., *Titanium in medicine: material science, surface science, engineering, biological responses, and medical applications*2001: Springer.

82. Darvell, B.W., et al., *Contamination of titanium castings by aluminium oxide blasting.* Journal of Dentistry, 1995. **23**(5): p. 319-322.

83. Ratner, B.D., A.S. Hoffman, and F.J. Schoen, *Biomaterials science: an introduction to materials in medicine*1996: Academic Press.

84. Takeuchi, M., et al., *Acid pretreatment of titanium implants.* Biomaterials, 2003. **24**(10): p. 1821-1827.

85. Li, P., et al., *Bonelike Hydroxyapatite Induction by a Gel-Derived Titania on a Titanium Substrate.* Journal of the American Ceramic Society, 1994. **77**(5): p. 1307-1312.

86. Wang, X.-X., et al., *Bioactive titania gel layers formed by chemical treatment of Ti substrate with a H2O2/HCl solution.* Biomaterials, 2002. **23**(5): p. 1353-1357.

87. Variola, F., et al., *Influence of Treatment Conditions on the Chemical Oxidative Activity of H2SO4/H2O2 Mixtures for Modulating the Topography of Titanium.* Advanced Engineering Materials, 2009. **11**(12): p. B227-B234.

88. Yi, J.-H., et al., *Characterization of a bioactive nanotextured surface created by controlled chemical oxidation of titanium.* Surface Science, 2006. **600**(19): p. 4613-4621.

89. Martin, H.J., et al., *Enhanced bonding of chitosan to implant quality titanium via four treatment combinations.* Thin Solid Films, 2008. **516**(18): p. 6277-6286.

90. Martin, H.J., et al., *XPS Study on the Use of 3-Aminopropyltriethoxysilane to Bond Chitosan to a Titanium Surface.* Langmuir, 2007. **23**(12): p. 6645-6651.

91. Parkhill, R.L., E.T. Knobbe, and M.S. Donley, *Application and evaluation of environmentally compliant spray-coated ormosil films as corrosion resistant treatments for aluminum 2024-T3.* Progress in Organic Coatings, 2001. **41**(4): p. 261-265.

92. Karmakar, B., et al., *Silica microspheres from the system tetraethyl orthosilicate-acetic acid-water.* Journal of Non-Crystalline Solids, 1991. **135**(1): p. 29-36.

93. Huang, Y. and W. Liu, *Sol–gel composite coatings from methyltriethoxysilane and polymethylhydrosiloxane.* Journal of Sol-Gel Science and Technology, 2010. **55**(3): p. 261-268.

94. Zandi-zand, R., A. Ershad-langroudi, and A. Rahimi, *Silica based organic–inorganic hybrid nanocomposite coatings for corrosion protection.* Progress in Organic Coatings, 2005. **53**(4): p. 286-291.

95. Wang, D. and G.P. Bierwagen, *Sol–gel coatings on metals for corrosion protection.* Progress in Organic Coatings, 2009. **64**(4): p. 327-338.

96. Stöber, W., A. Fink, and E. Bohn, *Controlled growth of monodisperse silica spheres in the micron size range.* Journal of Colloid and Interface Science, 1968. **26**(1): p. 62-69.

97. Brinker, C.J. and G.W. Scherer, *Sol-gel science: the physics and chemistry of sol-gel processing*1990: Academic Press.

98. Kickelbick, G., *Introduction to Hybrid Materials*, in *Hybrid Materials*2007, Wiley-VCH Verlag GmbH & Co. KGaA. p. 1-48.

99. Atik, M., et al., *Sol-gel thin films for corrosion protection.* Ceramics International, 1995. **21**(6): p. 403-406.

100. Fedrizzi, L., et al., *The use of electrochemical techniques to study the corrosion behaviour of organic coatings on steel pretreated with sol–gel zirconia films.* Electrochimica Acta, 2001. **46**(24-25): p. 3715-3724.

101. Peltola, T., et al., *Calcium phosphate induction by sol-gel-derived titania coatings on titanium substrates in vitro.* Journal of Biomedical Materials Research, 1998. **41**(3): p. 504-510.

102. Yuan, S.J., et al., *Biocorrosion Behavior of Titanium Oxide/Butoxide-Coated Stainless Steel.* Journal of The Electrochemical Society, 2008. **155**(5): p. C196-C210.

103. Karlsson, K.H., K. Fröberg, and T. Ringbom, *A structural approach to bone adhering of bioactive glasses.* Journal of Non-Crystalline Solids, 1989. **112**(1-3): p. 69-72.

104. Vasconcelos, D.C.L., et al., *Corrosion resistance of stainless steel coated with sol–gel silica.* Journal of Non-Crystalline Solids, 2000. **273**(1-3): p. 135-139.

105. Guglielmi, M., *Sol-Gel Coatings on Metals.* Journal of Sol-Gel Science and Technology, 1997. **8**(1): p. 443-449.

106. Zheludkevich, M.L., et al., *Corrosion protective properties of nanostructured sol–gel hybrid coatings to AA2024-T3.* Surface and Coatings Technology, 2006. **200**(9): p. 3084-3094.

107. Sakka, S., *Handbook of sol-gel science and technology: processing, characterization and applications*2005: Kluwer Academic Publishers.

108. Nazeri, A., P.P. Trzaskoma-Paulette, and D. Bauer, *Synthesis and Properties of Cerium and Titanium Oxide Thin Coatings for Corrosion Protection of 304*

Stainless Steel. Journal of Sol-Gel Science and Technology, 1997. **10**(3): p. 317-331.

109. Metroke, T.L., O. Kachurina, and E.T. Knobbe, *Spectroscopic and corrosion resistance characterization of GLYMO–TEOS Ormosil coatings for aluminum alloy corrosion inhibition.* Progress in Organic Coatings, 2002. **44**(4): p. 295-305.

110. Fallet, M., et al., *Electrochemical behaviour of ceramic sol–gel coatings on mild steel.* Journal of Non-Crystalline Solids, 2001. **293-295**(0): p. 527-533.

111. Chen, Y., L. Jin, and Y. Xie, *Sol-Gel Processing of Organic-Inorganic Nanocomposite Protective Coatings.* Journal of Sol-Gel Science and Technology, 1998. **13**(1): p. 735-738.

112. Veeraraghavan, B., et al., *Development of a Novel Electrochemical Method to Deposit High Corrosion Resistant Silicate Layers on Metal Substrates.* Electrochemical and Solid-State Letters, 2003. **6**(2): p. B4-B8.

113. Tarasevich, M., *Ultrasonic hydrolysis of a metal alkoxide without alcohol.* Ceramic Bulletin, 1984. **63**: p. 500.

114. Suslick, K.S., et al., *Sonochemical synthesis of amorphous iron.* Nature, 1991. **353**(6343): p. 414-416.

115. Blanco, E., et al., *Sonogels and derived materials.* Applied Organometallic Chemistry, 1999. **13**(5): p. 399-418.

116. Ramírez-del-Solar, M., et al., *Ultrastructural evolution during gelation of TiO2-SiO2 sols.* Journal of Non-Crystalline Solids, 1992. **147-148**(0): p. 206-212.

117. Rosa-Fox, N., L. Esquivias, and J. Zarzycki, *Silica sonogels with drying control chemical additives.* Journal of Materials Science Letters, 1991. **10**(21): p. 1237-1242.

118. Calvino, J.J., et al., *Ultrasound as a tool for the preparation of gels: effect on the textural properties of TiO2-SiO2 aerogels.* Journal of Materials Science, 1993. **28**(8): p. 2191-2195.

119. Fernández-Lorenzo, C., et al., *Sol-gel synthesis of SiO2□P2O5 glasses.* Journal of Non-Crystalline Solids, 1994. **176**(2-3): p. 189-199.

120. Leighton, T.G., *The acoustic bubble*1994: Academic Press.

121. Mason, T.J. and J.P. Lorimer, *Applied sonochemistry: the uses of power ultrasound in chemistry and processing*2002: Wiley-VCH.

122. Pol, V.G., et al., *Sonochemical Deposition of Silver Nanoparticles on Silica Spheres.* Langmuir, 2002. **18**(8): p. 3352-3357.

123. Chen, Q., et al., *Silica Coating of Nanoparticles by the Sonogel Process.* Langmuir, 2008. **24**(3): p. 650-653.

124. Chen, Q., et al., *Sol–gel nanocoating on commercial TiO₂ nanopowder using ultrasound.* Journal of Sol-Gel Science and Technology, 2010. **53**(1): p. 115-120.

125. Dang, F., et al., *Sonochemical coating of magnetite nanoparticles with silica.* Ultrasonics Sonochemistry, 2010. **17**(1): p. 193-199.

126. Pol, V.G., A. Gedanken, and J. Calderon-Moreno, *Deposition of Gold Nanoparticles on Silica Spheres: A Sonochemical Approach.* Chemistry of Materials, 2003. **15**(5): p. 1111-1118.

127. Kotlyar, A., et al., *Coating silver nanoparticles on poly(methyl methacrylate) chips and spheres via ultrasound irradiation.* Journal of Applied Polymer Science, 2007. **104**(5): p. 2868-2876.

128. Perelshtein, et al., *Sonochemical coating of silver nanoparticles on textile fabrics (nylon, polyester and cotton) and their antibacterial activity*. Vol. 19. 2008, Bristol, Royaume University: Institute of Physics.

129. Perkas, et al., *Depositing silver nanoparticles on/in a glass slide by the sonochemical method*. Vol. 19. 2008.

130. Gottesman, R., et al., *Sonochemical Coating of Paper by Microbiocidal Silver Nanoparticles.* Langmuir, 2010. **27**(2): p. 720-726.

131. Soloviev, M. and A. Gedanken, *Coating a stainless steel plate with silver nanoparticles by the sonochemical method.* Ultrasonics Sonochemistry, 2011. **18**(1): p. 356-362.

132. V.A. Kheraj, C.J.P., M.S, Desai, V. Porbhare, *Simulation of refectivity spectrum for non-absorbing multilayer optical thin films.* Journal of Physics, 2009. **72**(6): p. 1011-1022.

133. Hecht, E., *Optics*2002: Addison-Wesley.

134. Palik, E.D. and G. Ghosh, *Handbook of optical constants of solids*1998: Academic Press.

135. Wagner, C.D. and G.E. Muilenberg, *Handbook of x-ray photoelectron spectroscopy: a reference book of standard data for use in x-ray photoelectron spectroscopy*1979: Perkin-Elmer Corp., Physical Electronics Division.

136. Vollet, D.R., et al., *Structural characteristics of gels prepared from sonohydrolysis and conventional hydrolysis of TEOS: an emphasis on the mass*

fractal as determined from the pore size distribution. physica status solidi (a), 2005. **202**(14): p. 2700-2708.

137. Suslick, K.S., *Sonochemistry.* Science, 1990. **247**(4949): p. 1439-1445.

138. Enomoto N., M.S.N.Z.E., *Agglomeration of Silica Spheres under Ultrasonication*. Vol. 12. 1997: Cambridge University Press. 6.

139. Matsoukas, T. and E. Gulari, *Dynamics of growth of silica particles from ammonia-catalyzed hydrolysis of tetra-ethyl-orthosilicate.* Journal of Colloid and Interface Science, 1988. **124**(1): p. 252-261.

140. Friedman, A., et al., *Depositing nanoparticles inside millimeter-size hollow tubing.* Applied Surface Science, (0).

141. Brambilla, R., et al., *Spherical and lamellar octadecylsilane hybrid silicas.* Journal of Non-Crystalline Solids, 2008. **354**(45-46): p. 5033-5040.

142. Brambilla, R., et al., *Octadecylsilane hybrid silicas prepared by the sol–gel method: Morphological and textural aspects.* Journal of Colloid and Interface Science, 2007. **312**(2): p. 326-332.

143. Oliveira, E.M., et al., *Reactivation of passive titanium: the enhancement of O2 evolution after potentiodynamic cyclings.* Electrochemistry Communications, 2000. **2**(4): p. 254-258.

144. Conway, L., *Modeling of DBR Mirrors for Vertical Cavity Surface Emitting Lasers, with an Emphasis on Optical Materials.* M.Sc. Thesis, 1999.